

國立臺灣大學電機資訊學院電信工程學研究所

碩士論文

Graduate Institute of Communication Engineering
College of Electrical Engineering and Computer Science
National Taiwan University
Master Thesis



使用空氣填充式基板集成波導結構之毫米波波束成形

天線陣列

mm-Wave Beamforming Antenna Array Using AFSIW
Structure

劉庭孜

Ting-Zi Liu

指導教授：吳宗霖 博士

Advisor: Tzong-Lin Wu, Ph.D.

中華民國 108 年 10 月

October, 2019

國立臺灣大學 (碩) 博士學位論文
口試委員會審定書



使用空氣填充式基板集成波導結構之毫米波波束成形
天線陣列

mm-Wave Beamforming Antenna Array Using AFSIW
Structure

本論文係劉庭孜君 (R06942021) 在國立臺灣大學電信工程學研究所完成之碩士學位論文，於民國 108 年 10 月 01 日承下列考試委員審查通過及口試及格，特此證明

口試委員：

吳宗霖

(簽名)

(指導教授)

林丁丙

黃建宗

鄭文鋒

周錦偉

所長

蘇KJ

(簽名)

誌謝



兩年多的碩士生活很快的過去了，在這兩年多感謝許多人的幫助，將當初一個創新的想法實做出來，並在遇到瓶頸時，給予許多建議與想法，讓我順利完成研究，並了解到研究的方法與態度。

首先，要感謝我的指導教授吳宗霖教授，讓我完成研究，取得碩士學位。過去兩年多，當遇到困難時，老師總是提供他的想法與建議給我參考，從老師身上不僅可以學到專業知識，還可以學到研究的方法與態度，以及待人處事的方式。感謝先豐通訊李建成副總、廖中興課長花時間多次溝通與製作，並提供許多可以嘗試的做法，一同努力讓成品成功。另外，也感謝口試委員鄭文鋒董事長、林丁丙教授、黃建彰教授、以及周錫增教授在口試時給予的許多意見，使本論文更加完整。

感謝 EMC 實驗室的大家給予的各方面幫助與意見。感謝帶領我的仲原學長，給予我許多研究上的專業知識以及意見，讓我能夠收穫滿滿，並提供我許多文法的知識，將我的英文論文更加完美。感謝陳襄學長，花時間與我討論製程與研究的問題，提供許多寶貴的建議。感謝齊軒學長、揚智學長幫忙量測與教我如何使用下針量測。感謝高圻、誠吾幫忙檢查 layout 圖是否有誤，並花時間互相討論製程和研究的問題，讓我從中獲得許多想法與收穫。感謝幫助過我和關心過我的各位，並祝福各位日後也能事事順利。

最後，感謝我的家人，謝謝你們的支持與鼓勵，讓我能夠無憂無慮地完成研究並取得碩士學位，我將這份榮譽與歡樂跟你們共享。

劉庭孜
2019.10

中文摘要



隨著時代的進步及行動通訊需求大量增加，第五代行動通訊技術利用毫米波段中的部分頻譜來增加通信容量、降低功耗、提高資料傳輸速率和減少延遲。其中透過波束成形技術可以鎖定特定區域，來改善基地站無法涵蓋之區域的傳輸速率，而波束成形是藉由調整多個天線的輸入訊號大小與相位權重，以控制主波束的方向。巴特勒矩陣是其中一種可以達到此種目的的電路，且巴特勒矩陣使用元件數較少、損耗較小、以及較便宜。另外，為了降低功耗，需減少傳輸路徑上的損耗，因此本文採用空氣填充式基板集成波導結構來設計巴特勒矩陣饋入陣列天線，以達到波束成形功能，以及降低損耗之特性。

傳統波導管之體積較笨重、耗費較高又無法與平面集成。為了有利於封裝整合，因此衍生出基板集成波導結構的設計。該結構利用基板上下兩層的全金屬，配合兩側穿層的金屬柱作為金屬牆，形成一個可以與平面集成體積較小又低成本的平面波導結構。由於基板集成波導在傳輸過程中會接觸到有損介質，且在高頻時，有損介質材料的損耗大，因此造成能量在傳輸過程大量損耗。為了降低損耗，因而衍生出本文採用之空氣填充式基板集成波導結構。該結構將傳統基板集成波導之有損介質基板改為空氣基板，由於有損介質材料的損耗大於空氣，因此空氣填充式基板集成波導結構可以降低傳輸過程產生的損耗。

巴特勒矩陣是由耦合器、交叉耦合器以及相移器所組成的，其中本論文所使用的相移器為短截線相移器。本論文針對此相移器進行分析，並建立其等效電路模組，以此模組設計出可應用於空氣填充式基板集成波導結構的巴特勒矩陣之相移器。

為了驗證空氣填充式基板集成波導結構損耗較低，因此利用空氣填充式基板集成波導結構設計四乘四巴特勒矩陣饋入陣列天線，經模擬得知，在 60 GHz 時，此設計電路之損耗低於 1 dB，與參考文獻中，使用傳統基板集成波導設計之巴特勒矩陣相比明顯小 1 dB，因此證實使用空氣填充式基板集成波導結構設計出來之

四乘四巴特勒矩陣之損耗較低，而將此電路饋入陣列天線，不但具有波束成形功能，又低損耗，且應用於毫米波頻段。

關鍵字：巴特勒矩陣、空氣填充式基板集成波導、毫米波、相移器、陣列天線。



ABSTRACT



With the advancement of the times and the increasing demand for mobile communications, the fifth-generation mobile networks will utilize part of the spectrum in the millimeter-wave (mm-Wave) band to increase communication capacity, reduce power consumption, increase data transmission rate, and reduce delay. The beamforming technology can specify a specific area to improve the transmission rate of an area that cannot be covered by the base station. And beamforming controls the direction of the main beam by adjusting the input signal magnitude and phase weight of multiple antennas. The Butler Matrix is one of the circuits that can achieve beamforming. The Butler Matrix uses fewer components, less loss, and is less expensive. In addition, in order to reduce power consumption, it is necessary to reduce the loss on the transmission path. Therefore, this thesis uses an air-filled substrate integrated waveguide (AFSIW) structure to design an extremely low loss Butler matrix feeding beamforming antenna array.

Traditional waveguides are bulky, expensive, and can't be integrated with the plane. In order to make package integration easy, the design of the substrate integrated waveguide (SIW) structure is evolved. The structure utilizes the full metal of the upper and lower layers of the substrate, and the through-hole via on the two sides is used as the metal wall to form a planar waveguide structure which can be integrated with the plane and has a small size and low cost. However, due to the contact with the lossy substrate or air during the transmission, there is still a non-negligible power loss when applied in high frequencies. In order to further reduce losses, the AFSIW structure is evolved on this thesis. The AFSIW structure changes the lossy dielectric substrate of the conventional SIW into the air. Therefore, the AFSIW structure can avoid the loss from substrate and achieve better performance than traditional SIW.

Butler matrix is composed of the coupler, the crossover and the phase shifter. The stub phase shifter is used in this thesis. In this thesis, the stub phase shifter is analyzed and the equivalent circuit module of the stub phase shifter is established. The module is designed to apply in the phase shifter of the Butler matrix on AFSIW structure.

In order to verify that the structure of the AFSIW has low loss, a 4×4 Butler matrix feeding array antenna is designed by using an AFSIW structure. The simulation shows that the loss of this design circuit is less than 1 dB at 60 GHz, which is significantly smaller than the traditional SIW Butler matrix 1 dB. Therefore, it is confirmed that the loss of the 4×4 Butler matrix designed using the AFSIW is low. And the extremely low loss Butler matrix feeding beamforming antenna array is applied in the millimeter-wave band.

Index terms – Butler matrix, air-filled substrate integrated waveguide (AFSIW), millimeter-wave (mm-Wave), phase shifter, array antenna

CONTENTS

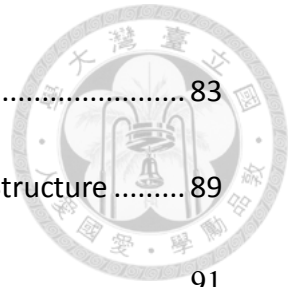


國立台灣大學碩士學位論文口試委員會審定書	#
誌謝	i
中文摘要	ii
ABSTRACT	iv
CONTENTS	vi
LIST OF FIGURES	ix
LIST OF TABLES	xiv
Chapter 1 Introduction	1
1.1 Research Motivation	1
1.2 Literature Survey	2
1.3 Contributions	4
1.4 Organization of This Thesis	4
Chapter 2 Introduction of SIW and Butler Matrix	7
2.1 Introduction of Waveguide	7
2.2 Introduction of SIW	13
2.3 Introduction of antenna array	15



2.4	Introduction of Butler Matrix	17
Chapter 3	Novel Structure of AFSIW	23
3.1	AFSIW Fabrication.....	23
3.2	AFSIW Feeding.....	30
Chapter 4	AFSIW Stub Phase Shifter	33
4.1	Introduction of Stub Phase Shifter.....	34
4.2	Analysis of Stub Phase Shifter in AFSIW	40
4.2.1	Design Procedure.....	44
4.3	AFSIW Stub Phase Shifter Design.....	48
4.4	Measurement and Discussion	55
4.5	Sensitivity About Fabrication	57
Chapter 5	AFSIW 4x4 Butler Matrix Antenna Array.....	61
5.1	Coupler Design.....	62
5.2	Crossover Design.....	70
5.3	Slot Antenna Array Design.....	74
5.3.1	Slot Antenna Design	74
5.3.2	Slot Antenna Array.....	78
5.4	AFSIW 4x4 Butler Matrix Antenna Array	83

5.4.1	Butler Matrix.....	83
5.4.2	Proposed Beamforming Antenna Array Using AFSIW Structure	89
5.5	Measured result and discussion	91
5.5.1	Coupler and Crossover.....	91
5.5.2	Butler Matrix and Butler Matrix Antenna Array.....	100
5.5.3	Comparison and Discussion.....	102
Chapter 6	Conclusions	105
REFERENCE	108



LIST OF FIGURES



Fig. 2.1 Rectangular waveguide	8
Fig. 2.2 TE ₁₀ mode	10
Fig. 2.3 TM ₁₁ mode	12
Fig. 2.4 SIW structure (Top view)	14
Fig. 2.5 Antenna array with N elements	16
Fig. 2.6 Block of a 4x4 butler matrix	17
Fig. 2.7 The radiation pattern of the butler matrix when $\phi = 0$ (x-z) cut on the spherical coordinate system.	22
Fig. 3.1 The description of each layer of AFSIW	23
Fig. 3.2 The fabrication process of the AFSIW (a) step1 (b) step2 (c) step3 (d) step4 (e) step5	25
Fig. 3.3 The front view and geometrical dimensions of the AFSIW	26
Fig. 3.4 The front view and geometrical dimensions of the modified AFSIW	28
Fig. 3.5 The simulation and measurement of the AFSIW on HFSS (a) Simulation (b) Measurement	29
Fig. 3.6 The structure of the AFSIW feeding. (a) 3D view (b) Top view (c) Side view	31
Fig. 3.7 The simulation results of AFSIW feeding on HFSS.	32

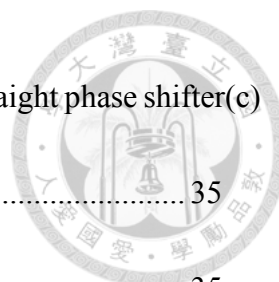


Fig. 4.1 Top view of SIW phase shifter (a) Curved phase shifter (b) Straight phase shifter(c)
Stub phase shifter 35

Fig. 4.2 The equivalent circuit of the stub phase shifter..... 35

Fig. 4.3 Use the ADS and HFSS to simulate the stub phase shifter (a) ADS circuit (b)
Magnitude (c) Phase 39

Fig. 4.4 (a) E-plane T-junction (b) H-plane T-junction 40

Fig. 4.5 The equivalent circuit of H-plane T-junction 41

Fig. 4.6 The equivalent circuit of H-plane T-junction with short stub 42

Fig. 4.7 The equivalent circuit of the overall short-ended stub phase shifter..... 44

Fig. 4.8 The 45-degree stub phase shifter compared by HFSS and MATLAB
(a)Magnitude (b) Phase 47

Fig. 4.9 The configuration of top view of the theoretical phase shifter 49

Fig. 4.10 The theoretical phase shifter (a) 0-deg phase shifter magnitude (b) 45-deg phase
shifter magnitude (c) the phase difference between the crossover and the 0/45-deg
phase shifter..... 51

Fig. 4.11 The configuration of top view of the proposed tuning phase shifter..... 52

Fig. 4.12 The proposed tuning phase shifter (a) 0-deg phase shifter magnitude (b) 45-deg
phase shifter magnitude (c) the phase difference between the crossover and the 0/45-
deg phase shifter 54

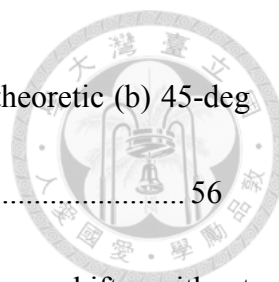


Fig. 4.13 The photograph of the proposed phase shifters. (a) 0-deg theoretic (b) 45-deg theoretic (c) 0-deg tuning (d) 45-deg tuning 56

Fig. 4.14 The measured and simulated results of the 0-deg tuning phase shifter without calibration. 56

Fig. 4.15 The X-ray photo of phase shifter. 57

Fig. 4.16 Sweep the parameters $\pm 0.05\text{mm}$ in phase shifter. 59

Fig. 5.1 The configuration of the coupler (Top view) 62

Fig. 5.2 The even mode junction discontinuity of the coupler (Top view) 64

Fig. 5.3 The geometrical dimensions of the proposed coupler. (Top view) 68

Fig. 5.4 The photograph of the coupler. 68

Fig. 5.5 The simulation results and measurement results of the proposed coupler. (a) S_{11} and S_{31} (b) S_{21} and S_{31} (c) Phase difference 70

Fig. 5.6 The geometrical dimensions of the proposed crossover. (Top view) 72

Fig. 5.7 The photograph of the crossover. 73

Fig. 5.8 The simulation results and measurement results of the proposed crossover. (a) magnitude (b) phase..... 74

Fig. 5.9 The transverse wave currents on the short-circuited waveguide..... 75

Fig. 5.10 TE_{10} mode waveguide transverse wave currents..... 76

Fig. 5.11 Structure of the slot antenna 76

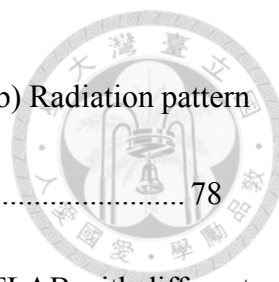


Fig. 5.12 The simulation results of the slot antenna. (a) S-parameter (b) Radiation pattern
 ($\phi = 0$)..... 78

Fig. 5.13 The radiation pattern of the antenna array calculated by MATLAB with different
 inter-element distances. 80

Fig. 5.14 The structure of the antenna array with isolation (a) 3D view (b) front view 81

Fig. 5.15 The maximum mutual coupling in the antenna array of the case 2- 4. 82

Fig. 5.16 Slot antenna array radiation pattern of case 1- 3..... 83

Fig. 5.17 S-parameter of the butler matrix on HFSS while exciting at port 1 and port 2. (a)
 $S_{11}, S_{21}, S_{31}, S_{41}$, (b) $S_{51}, S_{61}, S_{71}, S_{81}$, (c) $S_{12}, S_{22}, S_{32}, S_{42}$, and (d) $S_{52}, S_{62}, S_{72}, S_{82}$.
 86

Fig. 5.18 The total power insertion loss of the Butler matrix..... 87

Fig. 5.19 Phase difference of the butler matrix on HFSS. (a) Port 1 (b) Port 2 88

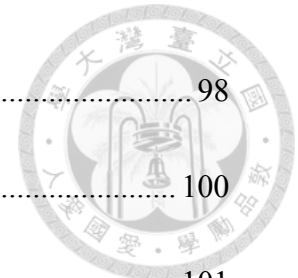
Fig. 5.20 Butler matrix antenna array radiation pattern on HFSS..... 90

Fig. 5.21 The cut-section of the thru and line. (a) The position of the cut-section. (Top
 view) (b) Thru (c) Line 93

Fig. 5.22 The post-simulated results and the error box of the TRL. (a) Thru (b) Line (c)
 Error box..... 95

Fig. 5.23 The post-simulated results of asymmetry coupler. (a) Top view of asymmetry
 coupler (b) S_{21} and S_{31} of post-simulated results 96

Fig. 5.24 Sweep the parameters $\pm 0.05\text{mm}$ in coupler.	98
Fig. 5.25 Sweep the parameters $\pm 0.05\text{mm}$ in crossover.	100
Fig. 5.26 The photograph of (a) Butler matrix (b) Butler matrix antenna array.	101



LIST OF TABLES



Table 2.1 Phase of output ports of the Butler matrix.....	20
Table 3.1 The geometrical dimension of the AFSIW	27
Table 3.2 The geometrical dimensions of the modified AFSIW	28
Table 4.1 Geometrical dimensions of the theoretical phase shifter.	49
Table 4.2 Geometrical dimensions of the proposed tuning phase shifter.	52
Table 5.1 Width and length of the slot region of the coupler.....	66
Table 5.2 Width and length of the slot region of the crossover.	71
Table 5.3 Geometry of the slot antenna.....	77
Table 5.4 The gain of the Butler matrix antenna array.	90
Table 5.5 The direction angle of the Butler matrix antenna array.	91
Table 5.6 Performance summary and comparison of Butler matrix to related literature.	103



Chapter 1

Introduction

1.1 Research Motivation

Due to the large increase in mobile data demand, a fifth-generation(5G) mobile networks will utilize part of the spectrum in the millimeter-wave (mm-Wave) band to increase communication capacity [1]. And because of operating at high frequency, mm-Wave communications suffer from high propagation loss and limited scattering. To solve these problems, some advanced antenna techniques are applied in 5G mm-Wave communication systems, such as the beamforming technique and the massive multiple-input multiple-output (MIMO) technique [2]. There are several kinds of beamforming technique, such as Butler matrix [3], Blass matrix [4] and Nolen matrix [5]. Among them, the Butler matrix has a lower loss and is cheaper than others.

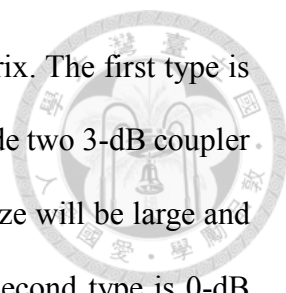
There are several challenges for mm-Wave communications, such as a planar integrated circuits design [1]. Using waveguide to design the Butler matrix is a typical method, but hard for packaging and system integration. To solve this problem, substrate integrated waveguide (SIW) can integrate planar circuits and offer smaller size than the traditional waveguide. However, due to the contact with the lossy substrate or air during the transmission, there is a non-negligible power loss in general SIW when it is applied in high frequency. In order to further reduce losses, the AFSIW structure is evolved on

this thesis. The AFSIW structure changes the lossy dielectric substrate of the conventional SIW into the air. Therefore, the AFSIW structure can avoid the loss from the substrate and achieve better performance than traditional SIW. So that, using this structure to design the Butler matrix can achieve low loss. That is why we use AFSIW to design the Butler matrix in this thesis.

1.2 Literature Survey

There are many different types of Butler matrices. The first type is the fundamental type. Four-input four-output (4×4) Butler matrix [3],[6],[7] is composed of four couplers, two crossovers, two 0-deg phase shifters, and two 45-deg phase shifters. The second type is the 4×8 Butler matrix [8],[9], which adds the power divider to reduce the sidelobe level. The third type is the two-dimensional Butler matrix [10],[11], which is composed of the N E-plane sub-beamforming network and the N H-plane sub-beamforming network. If this Butler matrix cascades the antenna array, it will obtain the $N \times N$ beam direction angle. Namely, if the circuit network is propagated on the z-axis, the beam-steering will obtain the N beam direction angle on the x-axis and N beam direction angle on the y-axis. The fourth type is the Butler matrix composed of multilayers [12],[13]. Except for the first type, other types are modified from the first type. Therefore, if the fundamental 4×4 Butler matrix is designed first, it will be easier to improve it into other types of Butler matrices.

The method to design the coupler is short-slot coupler, which is composed of two parallel waveguides with a common narrow wall between the waveguide is removed [14],[15]. The other method is the multilayer substrate, which is drilled a slot on the substrate to couple to another layer [16]. The disadvantage is that the multilayer is not cheap.



There are many different types of crossovers on the Butler matrix. The first type is cascaded 3-dB coupler [17],[18], which is a popular method to cascade two 3-dB coupler to form a 0-dB coupler. The disadvantages of this type are that the size will be large and return loss will be worse if the designed coupler is not good. The second type is 0-dB coupler, which is the same design method of the coupler [19]. The third type is without the crossover, which needs to rearrange the circuit network [20]. The advantage is that the loss of the crossover and the space of the crossover are reduced. The disadvantage is that the input ports should on the outside of the circuit and the output ports are inside the circuit, so the antenna array will be designed inside the circuit.

Phase shifters on the Butler matrix, there are many different types. One is the curved type, which propagates the desired phase through the curved line [21],[22]. The second type is changing the width of the waveguide to control the phase constant [23]. The third type is shunting a short stub to change the phase [24],[25].

From the above, we choose two papers to discuss detail. In [19], the Butler matrix is composed of a 3-dB coupler, a 0-dB coupler to be the crossover and the curved phase shifter. The total power insertion losses of the Butler matrix are below 2.5 dB and the phase error within 17° at 60 GHz on measurement. The array factors computed from the measured results are consistent with the ideal ones. In [20], the Butler matrix is composed of the 3-dB coupler, without the crossover and the curved phase shifter. The total power insertion losses of the Butler matrix are below 2 dB and the phase error within 4° at 77 GHz on simulation. Since the output ports of this Butler matrix are surrounded by the Butler matrix circuit, it's difficult to measure the Butler matrix. The measured direction angles of the Butler matrix antenna array are consistent with the ideal ones.



1.3 Contributions

The Butler matrix on AFSIW has a lower loss than the Butler matrix on SIW. And compared with a conventional waveguide, the Butler matrix on AFSIW can be a planar integrated circuit.

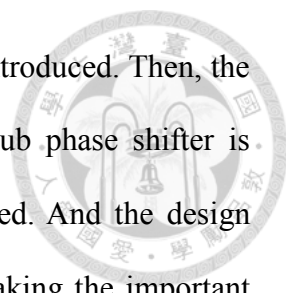
The shorted-end stub phase shifter is designed on AFSIW structure. The stub phase shifter on AFSIW is designed based on the waveguide theory. The equivalent circuit module of the stub phase shifter on AFSIW is established considering the non-negligible T-junction in the AFSIW stub phase shifter. And the design flow for AFSIW phase shifter is introduced.

Based on the theory of the slot-coupler, the 3-dB coupler and 0-dB crossover are designed. The error of the phase difference between the crossover and the phase shifter is small to avoid the phase error on the Butler matrix. The Butler matrix is composed of the proposed stub phase shifter, the proposed coupler, and proposed crossover.

The slot antenna array is designed based on the theory of the slot antenna. And the drilling slots between the antenna array are designed to prevent the mutual coupling affecting the radiation pattern. The antenna array is cascaded then with the Butler matrix. An extremely low-loss beamforming antenna array in AFSIW is proposed.

1.4 Organization of This Thesis

This thesis is organized as follows. In Chapter 2, the theory of the Butler matrix and SIW are introduced. First, the basic concept of the waveguide is introduced. Second, the concept of SIW is introduced. Then, the theory of the antenna array and the array factor would be derived. The theory of the Butler matrix and the phase of the output port would be derived in the end.



In Chapter 3, the fabrication process of the AFSIW would be introduced. Then, the feeding of the AFSIW would be introduced. In Chapter 4, the stub phase shifter is introduced. First, many kinds of phase shifters would be introduced. And the design formula of the stub phase shifter would be derived. Analyzed by taking the important effect of waveguide junction into consideration. In the end, the AFSIW stub phase shifter is proposed.

Chapter 5 starts with the design of the Butler matrix network. First, the crossover and the coupler would be proposed. Second, the slot antenna array would be designed. Then, each component would be combined to form the Butler matrix antenna array. And the phase difference of each output port and the simulated performance would be given. The measurement of the Butler matrix would be given and discussed in the end. Finally, the conclusions of this thesis are given in Chapter 6.





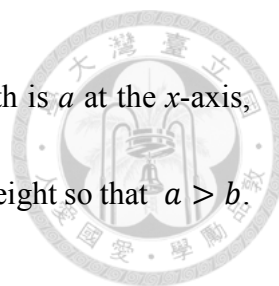
Chapter 2

Introduction of SIW and Butler Matrix

The rectangular waveguide is widely used in the microwave and mm-wave communication system, and many applications. Since the disadvantage of the waveguide, such as the size is bulk and non-planar, the new structure is evolved. This new structure is substrate integrated waveguide (SIW). SIW can be used to design the butler matrix network and be a planar integrated circuit. This chapter will first introduce the waveguide and SIW. The array factor of the antenna array will be derived. Then, the Butler matrix will be introduced and analyzed to know the phase difference of each output port. Thus, the combination of the Butler matrix and the antenna array can predict that when the input port input, the main beam will be directed to where.

2.1 Introduction of Waveguide

Rectangular waveguides are often used to transport microwave signals and used for many applications. But the size of the rectangular waveguide is often huger than using microstrip line or strip line. There are two modes to be propagated in a rectangular waveguide. One is TE mode, another is TM mode.



A typical rectangular waveguide is shown in Fig. 2.1. The width is a at the x -axis, and the height is b at the y -axis. Sometimes, the width is larger than height so that $a > b$. And the waveguide is propagated at the z -axis.

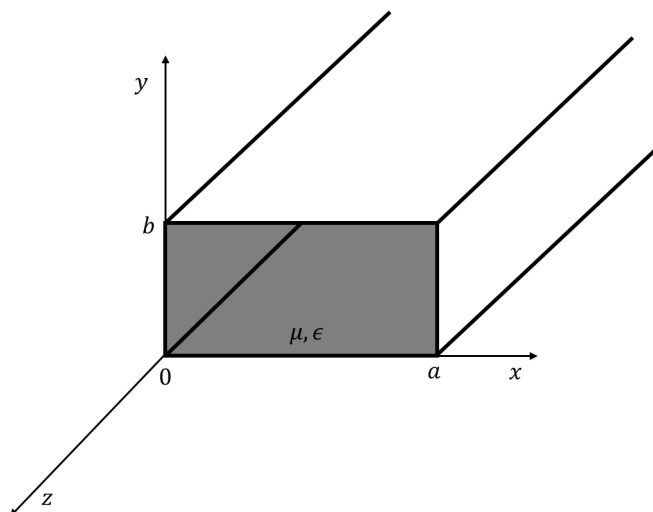


Fig. 2.1 Rectangular waveguide

■ TE modes

TE modes are characterized by $E_z = 0$ and $H_z \neq 0$. Then $H_z(x, y, z) = h_z(x, y)e^{-j\beta z}$, where propagation constant $\beta = \sqrt{k^2 - k_c^2}$, $k_x^2 + k_y^2 = k_c^2$ and $h_z(x, y) = (A \cos k_x x + B \sin k_x x)(C \cos k_y y + D \sin k_y y)$.

Since Maxwell's equations,

$$\nabla \times \vec{E} = -j\omega\mu\vec{H} \quad (2.1)$$

$$\nabla \times \vec{H} = j\omega\epsilon\vec{E} \quad (2.2),$$

can be reduced to

$$H_x = \frac{j}{k_c^2} \left(\omega\epsilon \frac{\partial E_z}{\partial y} - \beta \frac{\partial H_z}{\partial x} \right) \quad (2.3)$$



$$H_y = \frac{-j}{k_c^2} \left(\omega \epsilon \frac{\partial E_z}{\partial x} + \beta \frac{\partial H_z}{\partial y} \right) \quad (2.4)$$

$$E_x = \frac{-j}{k_c^2} \left(\beta \frac{\partial E_z}{\partial x} + \omega \mu \frac{\partial H_z}{\partial y} \right) \quad (2.5)$$

$$E_y = \frac{j}{k_c^2} \left(-\beta \frac{\partial E_z}{\partial y} + \omega \mu \frac{\partial H_z}{\partial x} \right) \quad (2.6)$$

and apply the boundary conditions on the electric field that tangential to the waveguide

walls: $e_x(x, y) = 0$, at $y = 0$ and b , $e_y(x, y) = 0$, at $x = 0$ and a [26].

From the above equations and conditions can get that $B = 0, D = 0, k_x = \frac{m\pi}{a}, k_y = \frac{n\pi}{b}$, for $m, n = 0, 1, 2, \dots$. Then the final

$$E_z = 0 \quad (2.7)$$

$$H_z = A_{mn} \cos \frac{m\pi x}{a} \cos \frac{n\pi y}{b} e^{-j\beta z} \quad (2.8)$$

$$E_x = \frac{j\omega\mu n\pi}{k_c^2 b} A_{mn} \cos \frac{m\pi x}{a} \sin \frac{n\pi y}{b} e^{-j\beta z} \quad (2.9)$$

$$E_y = \frac{-j\omega\mu m\pi}{k_c^2 a} A_{mn} \sin \frac{m\pi x}{a} \cos \frac{n\pi y}{b} e^{-j\beta z} \quad (2.10)$$

$$H_x = \frac{j\beta m\pi}{k_c^2 a} A_{mn} \sin \frac{m\pi x}{a} \cos \frac{n\pi y}{b} e^{-j\beta z} \quad (2.11)$$

$$H_y = \frac{j\beta n\pi}{k_c^2 b} A_{mn} \cos \frac{m\pi x}{a} \sin \frac{n\pi y}{b} e^{-j\beta z} \quad (2.12),$$

where A_{mn} is the amplitude of the multiplication of A and C, the propagation constant

is

$$\beta = \sqrt{k^2 - k_c^2} = \sqrt{k^2 - \left(\frac{m\pi}{a}\right)^2 - \left(\frac{n\pi}{b}\right)^2} \quad (2.13)$$

and the guided wavelength is

$$\lambda_g = \frac{2\pi}{\beta} \quad (2.14).$$



The cutoff frequency of each mode is

$$f_{c_{mn}} = \frac{k_c}{2\pi\sqrt{\mu\epsilon}} = \frac{1}{2\pi\sqrt{\mu\epsilon}} \sqrt{\left(\frac{m\pi}{a}\right)^2 + \left(\frac{n\pi}{b}\right)^2} \quad (2.15)$$

Because a is larger than b . So that TE_{10} mode is the dominant mode, where $m = 1, n = 0$. The field of TE_{10} mode is shown in Fig. 2.2. The solid line is the electric field line. The dashed line is the magnetic field line.

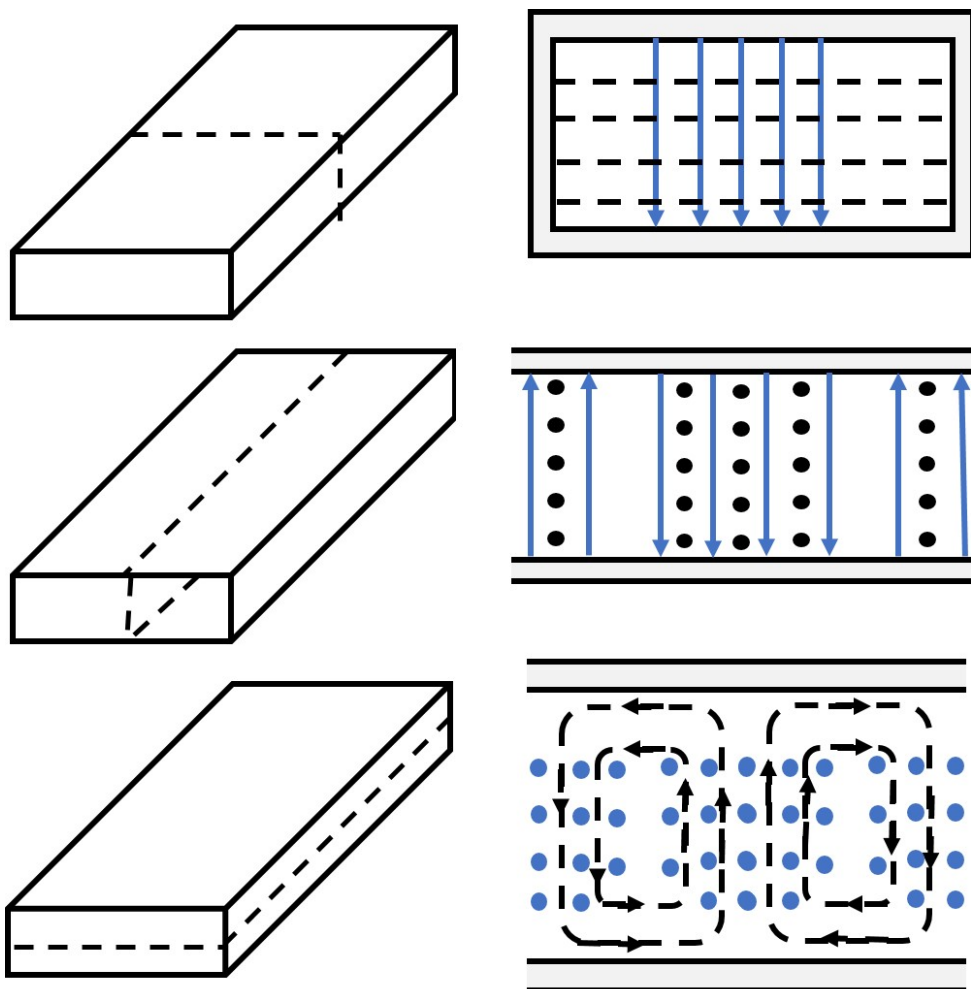
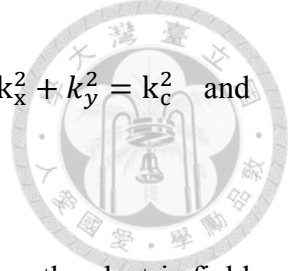


Fig. 2.2 TE_{10} mode

■ TM modes

TM modes are characterized by $H_z = 0$ and $E_z \neq 0$. Then $E_z(x, y, z) =$



$e_z(x,y)e^{-j\beta z}$, where propagation constant $\beta = \sqrt{k^2 - k_c^2}$, $k_x^2 + k_y^2 = k_c^2$ and

$$e_z(x,y) = (A \cos k_x x + B \sin k_x x)(C \cos k_y y + D \sin k_y y).$$

From equation (2.3)-(2.6) and apply the boundary conditions on the electric field that tangential to the waveguide walls: $e_z(x,y) = 0$, at $x = 0$ and a , $e_z(x,y) = 0$, at $y = 0$ and b .

From the above equations and conditions can get that $A = 0, C = 0, k_x = \frac{m\pi}{a}, k_y = \frac{n\pi}{b}$, for $m, n = 0, 1, 2, \dots$. Then the final

$$H_z = 0 \tag{2.16}$$

$$E_z = B_{mn} \sin \frac{m\pi x}{a} \sin \frac{n\pi y}{b} e^{-j\beta z} \tag{2.17}$$

$$E_x = \frac{-j\beta m\pi}{k_c^2 a} B_{mn} \cos \frac{m\pi x}{a} \sin \frac{n\pi y}{b} e^{-j\beta z} \tag{2.18}$$

$$E_y = \frac{-j\beta n\pi}{k_c^2 b} B_{mn} \sin \frac{m\pi x}{a} \cos \frac{n\pi y}{b} e^{-j\beta z} \tag{2.19}$$

$$H_x = \frac{j\omega\epsilon n\pi}{k_c^2 b} B_{mn} \sin \frac{m\pi x}{a} \cos \frac{n\pi y}{b} e^{-j\beta z} \tag{2.20}$$

$$H_y = \frac{-j\omega\epsilon m\pi}{k_c^2 a} B_{mn} \cos \frac{m\pi x}{a} \sin \frac{n\pi y}{b} e^{-j\beta z} \tag{2.21}$$

where B_{mn} is the amplitude of the multiplication of B and D, the propagation constant is

$$\beta = \sqrt{k^2 - k_c^2} = \sqrt{k^2 - \left(\frac{m\pi}{a}\right)^2 - \left(\frac{n\pi}{b}\right)^2} \tag{2.22}$$

and the guide wavelength is

$$\lambda_g = \frac{2\pi}{\beta} \tag{2.23}$$



The cutoff frequency of each mode is

$$f_{c_{mn}} = \frac{k_c}{2\pi\sqrt{\mu\epsilon}} = \frac{1}{2\pi\sqrt{\mu\epsilon}} \sqrt{\left(\frac{m\pi}{a}\right)^2 + \left(\frac{n\pi}{b}\right)^2} \quad (2.24)$$

Because E_z includes m and n . If m or n is equal to zero, the E_z will be equal to zero. So that TM_{11} mode is the lowest order mode, where $m = 1, n = 1$. The field of TM_{11} mode is shown in Fig. 2.3. The solid line is the electric field line. The dashed line is the magnetic field line.

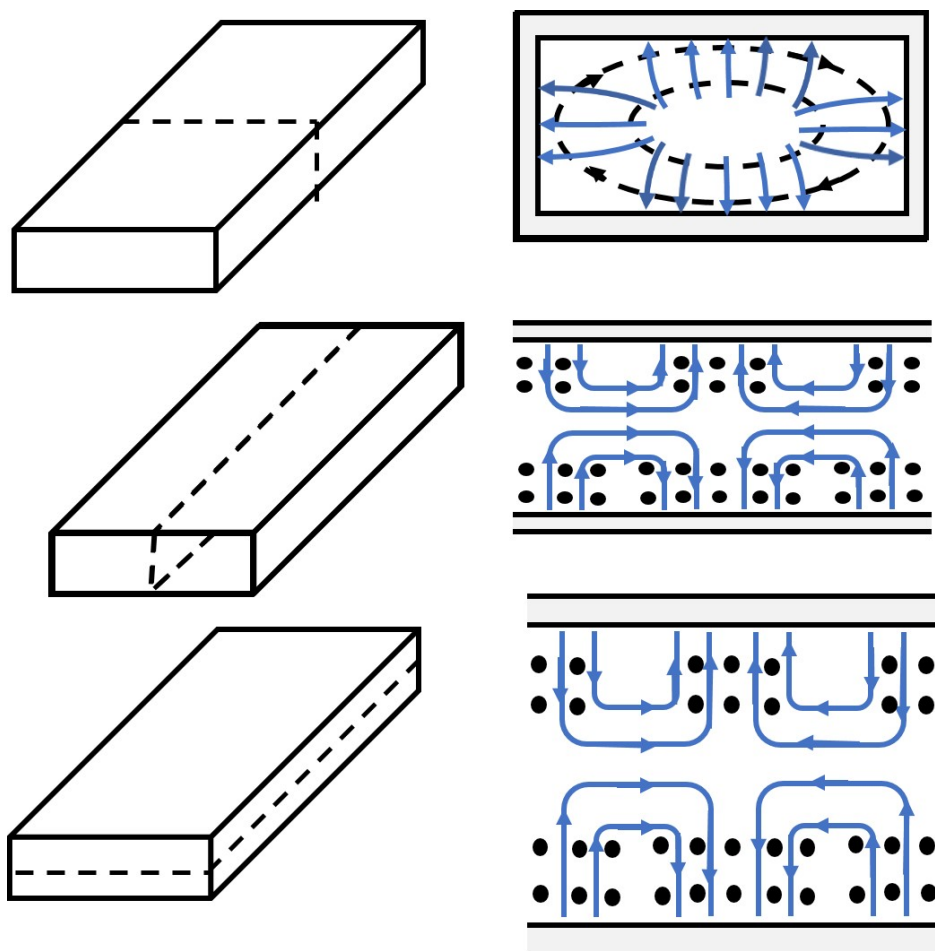


Fig. 2.3 TM_{11} mode



2.2 Introduction of SIW

Because the traditional rectangular waveguide is bulky, non-planar, and more restrictive in manufacturing, it is difficult to be the mm-wave planar integrated circuits [27]. The substrate integrated waveguide (SIW) is a structure using a printed circuit board (PCB) and metallic via holes on both sides, it's shown in Fig. 2.4. SIW structure is like a rectangular waveguide so that SIW can preserve the advantage of traditional rectangular waveguides, such as the high Q factor and high-power capacity [28]. And also, the advantage of the SIW is a small size and the planar circuit, which can improve the disadvantages of the traditional rectangular waveguide.

Since SIW is made up of metallic via holes, there are many gaps. From these gaps, it can be judged that SIW may produce the leakage problem or wave attenuation. In addition, the substrate of the SIW is lossy dielectric, so some losses were produced by the substrate.

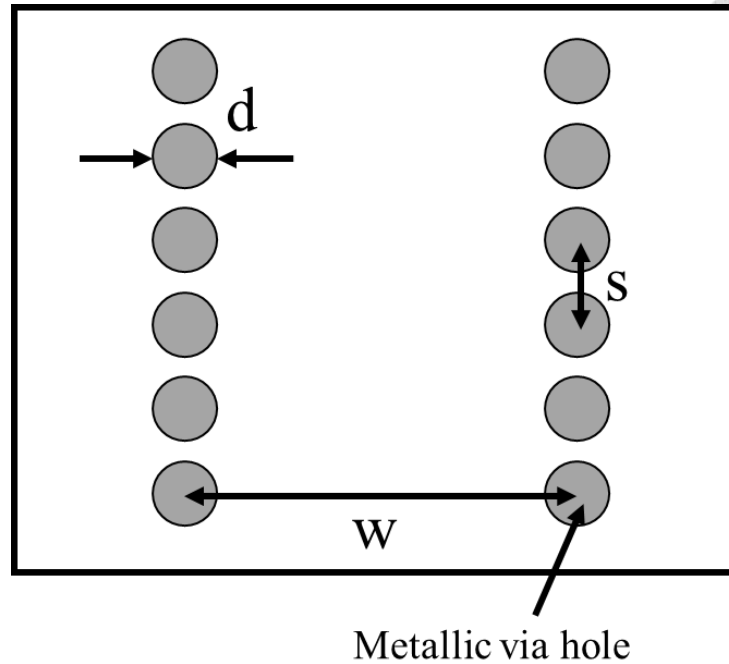


Fig. 2.4 SIW structure (Top view)

The equivalent width of the SIW (w_{eff}) is [28]

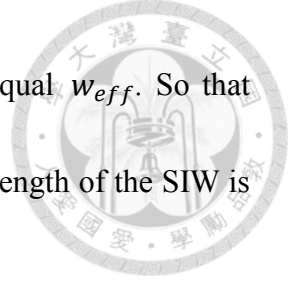
$$w_{eff} = w - 1.08 \cdot \frac{d^2}{s} + 0.1 \cdot \frac{d^2}{w} \quad (2.25),$$

where w is the width of the SIW, s is the pitch of the metallic via holes and d is the diameter of the metallic via holes, it's shown in Fig. 2.4.

As soon as, the gap of metallic via holes s is too large, the large radiation loss will be produced. The return loss of the SIW transition will be affected by the diameter of the metallic via holes (d). There are two useful criteria to establish upper bounds for s and d [29].

$$d \leq \frac{\lambda_g}{5} \quad (2.26)$$

$$s \leq 2d \quad (2.27),$$



where λ_g is the guided wavelength and the width of waveguide equal w_{eff} . So that when the fundamental mode of SIW is TE_{10} mode, the guided wavelength of the SIW is equal to

$$\lambda_{g_{10}} = \frac{2\pi}{\sqrt{\left(\frac{\epsilon_r \omega^2}{c^2}\right)^2 - \left(\frac{\pi}{w_{eff}}\right)^2}} \quad (2.28).$$

If the first higher mode of SIW is TE_{m0} mode, the limit of the via diameter equation (2.26) can be simplified from equation (2.15) and equation (2.28), which is given by

$$d \leq \frac{2w_{eff}}{5\sqrt{m^2 - 1}} \quad (2.29).$$

2.3 Introduction of antenna array

An antenna array is composed of N single antennas, which are separated at the same distance. The antenna array can achieve higher directivity and narrower beam than the single element. The antenna array also can control the direction of the beam by the phase difference. The antenna array is regarded as many isotropic point sources be separated the same distance. Then the radiation pattern can be calculated by the principle of pattern multiplication [30],

Radiation pattern of antenna array

$$= \text{Array factor} \times \text{Radiation pattern of individual antenna} \quad (2.30).$$

Fig. 2.5 shows the antenna array with n elements. Assume all individual antennas are isotropic point sources with the same distance. Then the electric field of the antenna array can be calculated as

$$E = E_0 + E_0 e^{j\psi} + E_0 e^{j2\psi} + \dots + E_0 e^{j(n-2)\psi} + E_0 e^{j(n-1)\psi} \quad (2.31),$$

where $\psi = \frac{2\pi d}{\lambda} \cos(90^\circ - \theta) + b$, d is the distance between the point sources, and b is the phase difference. Then equation (2.31) can be simplified as

$$E = E_0 \frac{1 - e^{jn\psi}}{1 - e^{j\psi}} = E_0 \frac{e^{\frac{jn\psi}{2}} \left(e^{\frac{jn\psi}{2}} - e^{-\frac{jn\psi}{2}} \right)}{e^{\frac{j\psi}{2}} \left(e^{\frac{j\psi}{2}} - e^{-\frac{j\psi}{2}} \right)} = E_0 e^{j\frac{n-1}{2}\psi} \frac{\sin \frac{n\psi}{2}}{\sin \frac{\psi}{2}} \quad (2.32).$$

The maximum of the electric field occurs on $\psi = 0$. The array factor is the normalized total electric field. Thus, the equation of the array factor (AF) of the antenna array can be obtained by

$$AF = \frac{|E|}{|E_{\max}|} = \frac{1 \sin \left(\frac{n\psi}{2} \right)}{n \sin \left(\frac{\psi}{2} \right)} \quad (2.33)$$

This analysis is assumed that the amplitude and the phase difference of all point sources are the same.

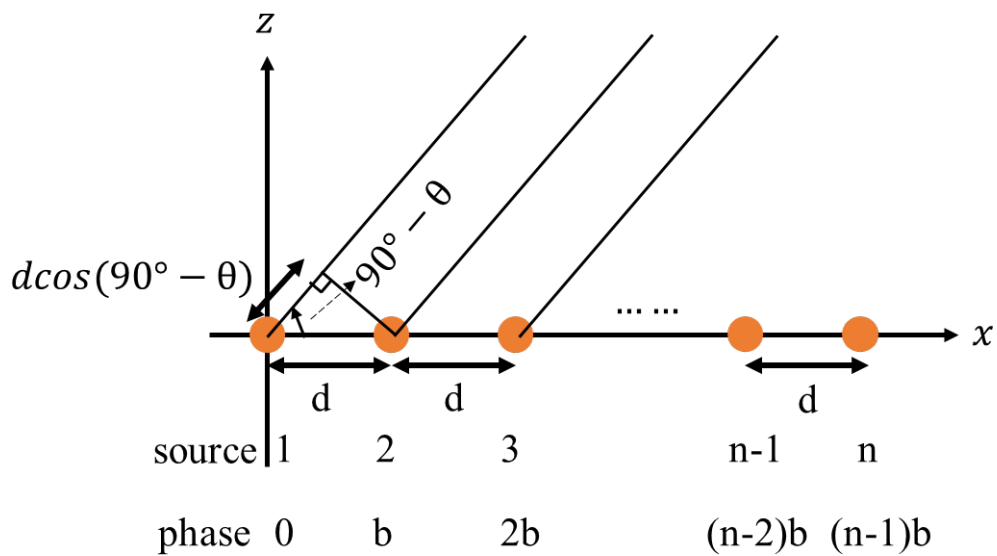


Fig. 2.5 Antenna array with N elements



2.4 Introduction of Butler Matrix

Butler matrix is a beamforming network for the multibeam antenna array. Butler matrix is a low loss network. The block diagram of the Butler matrix is shown in Fig. 2.6.

Butler matrix is composed of four 3-dB couplers, two crossovers, two 45° phase shifters, and two 0° phase shifters.

The output port of the butler matrix will be satisfied with two conditions. One is that the amplitude of each output port will be the same. Another is that when the same input port is input, the phase difference between adjacent output ports are the same.

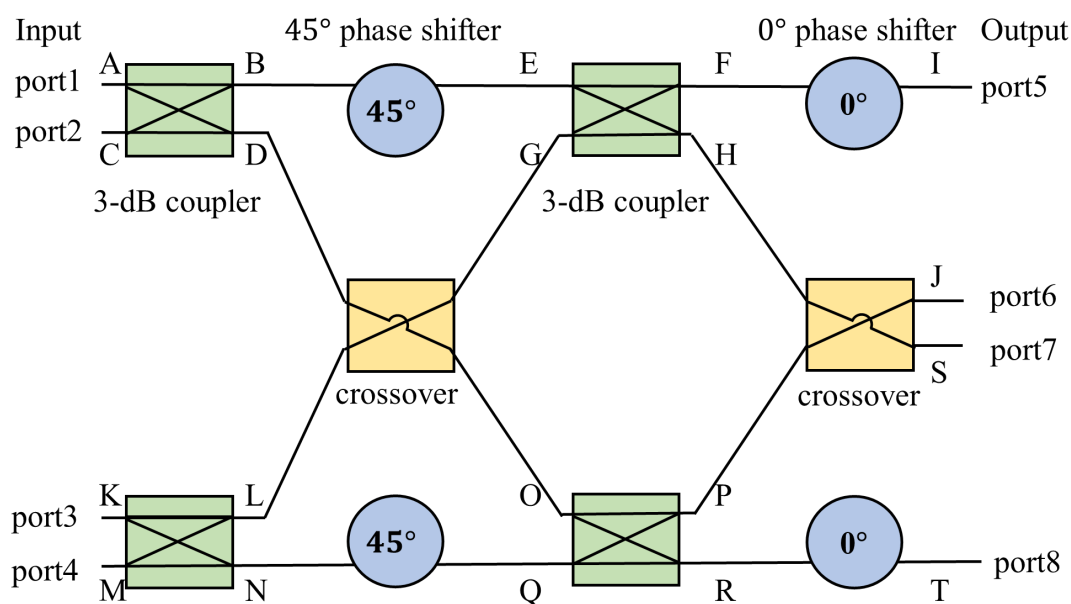


Fig. 2.6 Block of a 4x4 butler matrix

In the ideal case, the insertion loss of the coupler is 3 dB. The insertion loss of the crossover and the phase shifter are 0 dB. Thus, the total loss of each output port of the butler matrix is 6 dB. On the coupler, the phase difference between the coupled port and



the through port is 90 degrees. And the phase difference between the crossover and the 0° or 45° phase shifter is 0 degrees and 45 degrees, respectively. Assumed that couplers and crossovers are symmetric structure. The clearer descriptions are transformed into formulas as following:

$$|S_{BA}| = |S_{DA}| = |S_{BC}| = |S_{DC}| = 3dB \quad (2.34)$$

$$|S_{EB}| = |S_{OD}| = |S_{GL}| = |S_{IF}| = 0dB \quad (2.35)$$

$$\angle S_{DA} - \angle S_{BA} = \angle S_{BC} - \angle S_{DC} = -90^\circ \quad (2.36)$$

$$\angle S_{EB} = \angle S_{OD} - 45^\circ \quad (2.37)$$

$$\angle S_{IF} = \angle S_{SH} - 0^\circ \quad (2.38)$$

The phase of each output port of the Butler matrix and phase difference of the Butler matrix are computed at the following. And at the following, the PD is represented the phase difference of the Butler matrix.

■ Input port at port 1

$$\angle S_{51} = \angle S_{BA} + \angle S_{EB} + \angle S_{FE} + \angle S_{IF} \quad (2.39)$$

$$\angle S_{61} = \angle S_{DA} + \angle S_{OD} + \angle S_{PO} + \angle S_{JP} \quad (2.40)$$

$$\angle S_{71} = \angle S_{BA} + \angle S_{EB} + \angle S_{HE} + \angle S_{SH} \quad (2.41)$$

$$\angle S_{81} = \angle S_{DA} + \angle S_{OD} + \angle S_{RO} + \angle S_{TR} \quad (2.42)$$



$$\begin{aligned}
 PD1 &= \angle S_{61} - \angle S_{51} \\
 &= (\angle S_{DA} - \angle S_{BA}) + (\angle S_{OD} - \angle S_{EB}) + (\angle S_{JP} - \angle S_{IF}) \\
 &= -90^\circ + 45^\circ + 0^\circ = -45^\circ
 \end{aligned} \tag{2.43}$$

$$\begin{aligned}
 PD2 &= \angle S_{71} - \angle S_{61} \\
 &= (\angle S_{BA} - \angle S_{DA}) + (\angle S_{EB} - \angle S_{OD}) + (\angle S_{HE} - \angle S_{PO}) \\
 &= 90^\circ - 45^\circ - 90^\circ = -45^\circ
 \end{aligned} \tag{2.44}$$

$$\begin{aligned}
 PD3 &= \angle S_{81} - \angle S_{71} \\
 &= (\angle S_{DA} - \angle S_{BA}) + (\angle S_{OD} - \angle S_{EB}) + (\angle S_{TR} - \angle S_{SH}) \\
 &= -90^\circ + 45^\circ + 0^\circ = -45^\circ
 \end{aligned} \tag{2.45}$$

■ **Input port at port 2**

$$\angle S_{52} = \angle S_{BC} + \angle S_{EB} + \angle S_{FE} + \angle S_{IF} \tag{2.46}$$

$$\angle S_{62} = \angle S_{DC} + \angle S_{OD} + \angle S_{PO} + \angle S_{JP} \tag{2.47}$$

$$\angle S_{72} = \angle S_{BC} + \angle S_{EB} + \angle S_{HE} + \angle S_{SH} \tag{2.48}$$

$$\angle S_{82} = \angle S_{DC} + \angle S_{OD} + \angle S_{RO} + \angle S_{TR} \tag{2.49}$$

$$\begin{aligned}
 PD4 &= \angle S_{62} - \angle S_{52} \\
 &= (\angle S_{DC} - \angle S_{BC}) + (\angle S_{OD} - \angle S_{EB}) + (\angle S_{JP} - \angle S_{IF}) \\
 &= 90^\circ + 45^\circ + 0^\circ = 135^\circ
 \end{aligned} \tag{2.50}$$



$$\begin{aligned}
 PD5 &= \angle S_{72} - \angle S_{62} \\
 &= (\angle S_{BC} - \angle S_{DC}) + (\angle S_{EB} - \angle S_{OD}) + (\angle S_{HE} - \angle S_{PO}) \\
 &= -90^\circ - 45^\circ - 90^\circ = -225^\circ = 135^\circ
 \end{aligned}
 \tag{2.51}$$

$$\begin{aligned}
 PD6 &= \angle S_{82} - \angle S_{72} \\
 &= (\angle S_{DC} - \angle S_{BC}) + (\angle S_{OD} - \angle S_{EB}) + (\angle S_{TR} - \angle S_{SH}) \\
 &= 90^\circ + 45^\circ + 0^\circ = 135^\circ
 \end{aligned}
 \tag{2.52}$$

When the input ports are port 3 and port 4, the calculation method is the same as the input ports are port 2 and port 1. So that when the input ports are port 1, port 2, port 3, and port 4, the phase difference is -45° , 135° , -135° , and 45° , respectively. The phase of the output port and the phase difference can be summarized in Table 2.1.

<i>Output</i> <i>Input</i>	Port 5	Port 6	Port 7	Port 8	Phase difference
Port 1	-45°	-90°	-135°	-180°	-45°
Port 2	-135°	0°	-225°	-90°	135°
Port 3	-90°	-225°	0°	-135°	-135°
Port 4	-180°	-135°	-90°	-45°	45°

Table 2.1 Phase of output ports of the Butler matrix

Then, the antenna array is fed by the Butler matrix. From the equation (2.33), the array factor of the antenna array with 4 elements can be expressed as

$$AF = \frac{1}{4} \cdot \frac{\sin(2\psi)}{\sin\left(\frac{\psi}{2}\right)} \quad (2.53),$$

where

$$\psi = \frac{2\pi d}{\lambda} \cos(90^\circ - \theta) + b \quad (2.54).$$

When the array factor of equation (2.53) is the maximum, the ψ is equal to zero. And the equation (2.54) can be derived by

$$\theta = 90^\circ - \cos^{-1}\left(-\frac{\lambda b}{2\pi d}\right) \quad (2.55)$$

where θ is the angle of the main beam, b is the phase difference. Thus, the different phase difference can obtain the different direction of the main beam.

Assumed the distance (d) equal half wavelength ($\lambda/2$) to substitute into the equation (2.53) - (2.55). And the phase difference (b) is substituted by the phase difference of each output port of the Butler matrix. The radiation pattern of the butler matrix is shown in Fig. 2.7. The radiation pattern is the cut section on the spherical coordinate system when $\phi = 0$. However, the angle of Fig. 2.7 is the polar angle (θ) on the spherical coordinate system. From Fig. 2.7, it's shown that when input port is port 1, port 2, port3, and port 4, the direction of the main beam is 14.5° , -48.6° , 48.6° , and -14.5° on the spherical coordinate, respectively. So that when phase difference is $\pm 45^\circ$, the direction of the main beam is $\mp 14.5^\circ$. The direction of the main beam is mirrored at 0° .

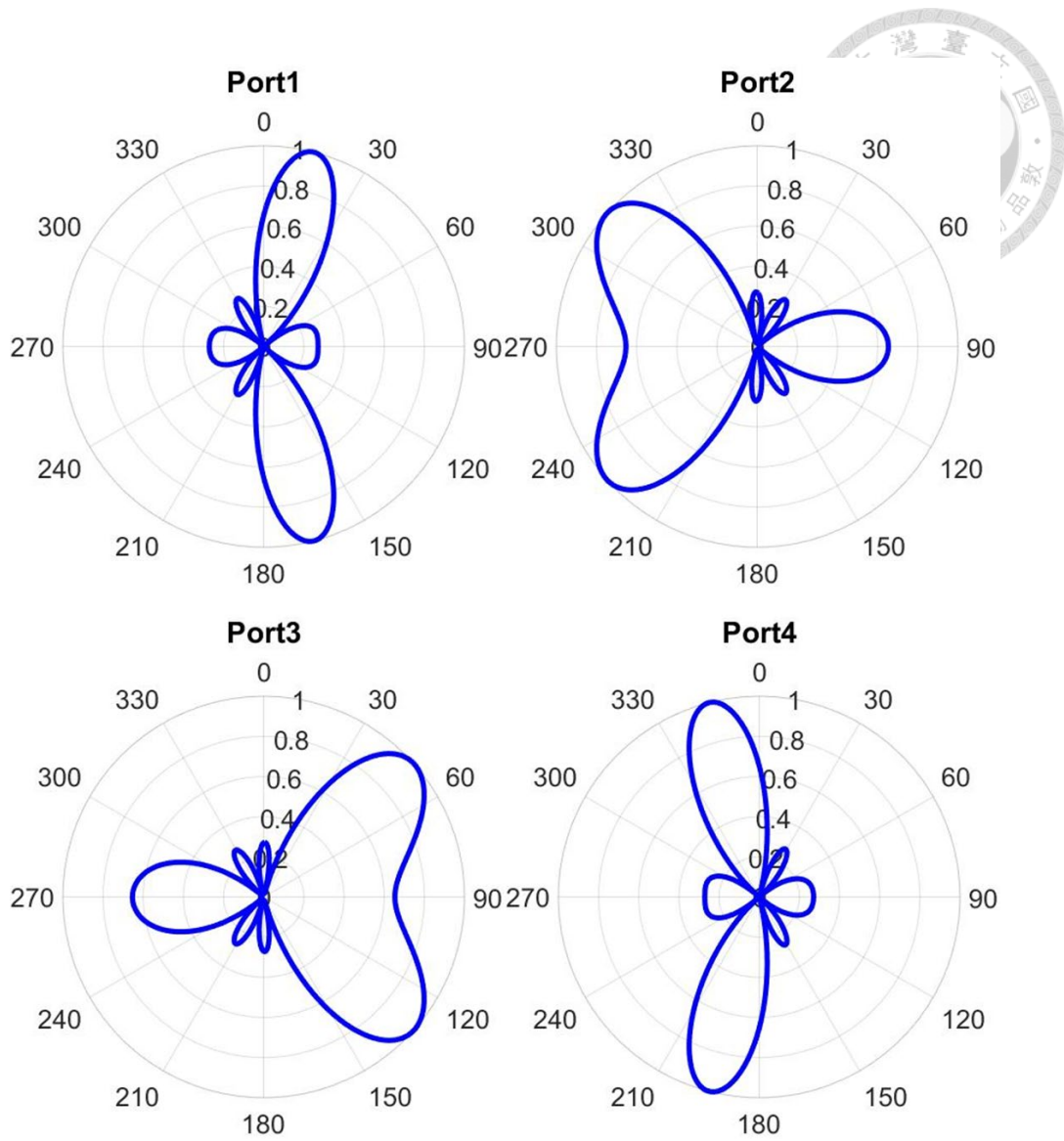


Fig. 2.7 The radiation pattern of the butler matrix when $\phi = 0$ (x-z) cut on the spherical coordinate system.



Chapter 3

Novel Structure of AFSIW

AFSIW on PCB is a novel structure. So, the fabrication process and stacking of AFSIW on PCB will be introduced in this chapter. And the feeding method of AFSIW also will be introduced in this chapter.

3.1 AFSIW Fabrication

In this thesis, we use the AFSIW structure, which is composed of three cores stuck by the prepreg (PP) and copper paste. The description of each layer of AFSIW is shown in Fig. 3.1. The CORE1 is a low loss material, whose $D_k = 3$ and $D_f = 0.0019$ at 10 GHz. The properties of the material of the CORE2 and CORE3 is $D_k = 4.1$ and $D_f = 0.016$ at 10 GHz.

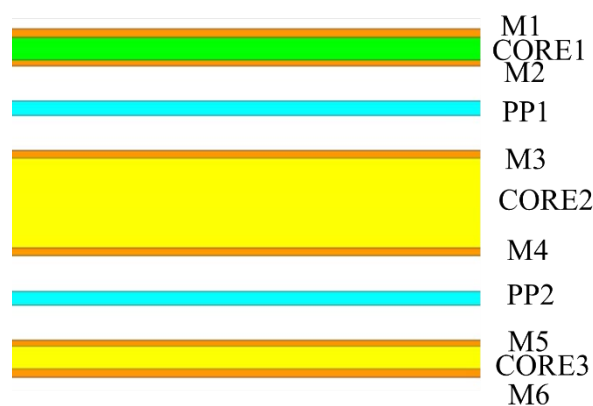
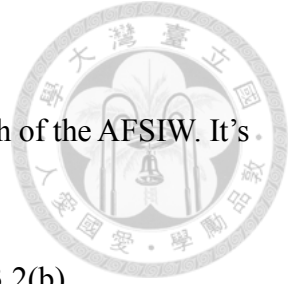


Fig. 3.1 The description of each layer of AFSIW



The fabrication process of the AFSIW as following:

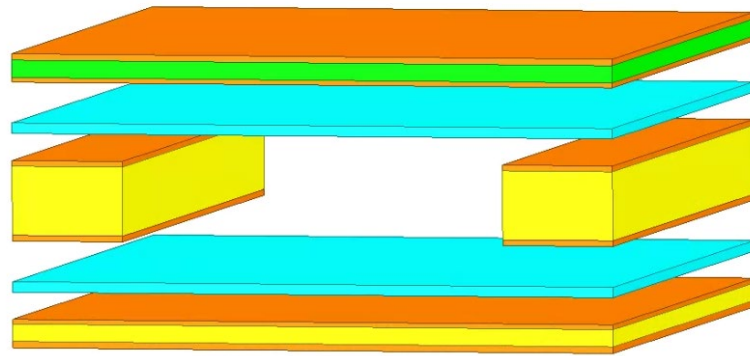
Step1: CORE2, M3, and M4 are dug with the desired width and length of the AFSIW. It's shown in Fig. 3.2(a).

Step2: CORE2 and CORE3 are stuck by the PP2. It's shown in Fig. 3.2(b).

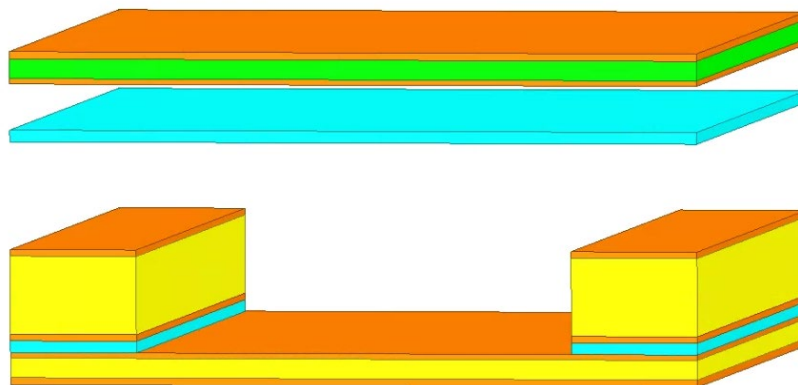
Step3: The copper is plated around the dug M3 to PP2. The bottom of the AFSIW is formed. It's shown in Fig. 3.2(c).

Step4: CORE1 and CORE2 are stuck by the PP1. It's shown in Fig. 3.2(d)

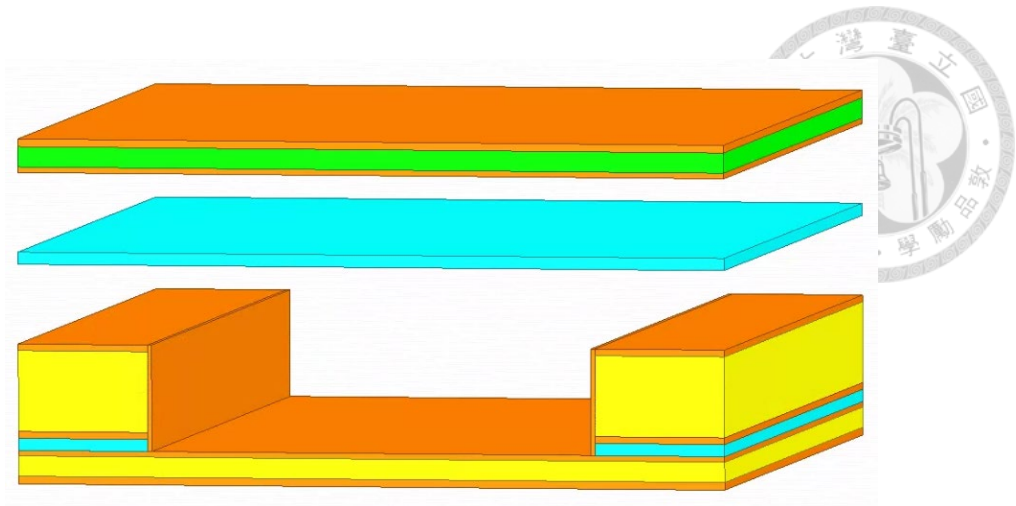
Step5: A row of the through-hole via on the two sides of the air channel to form the metal wall on the PP1 layer. The complete AFSIW is formed. It's shown in Fig. 3.2(e).



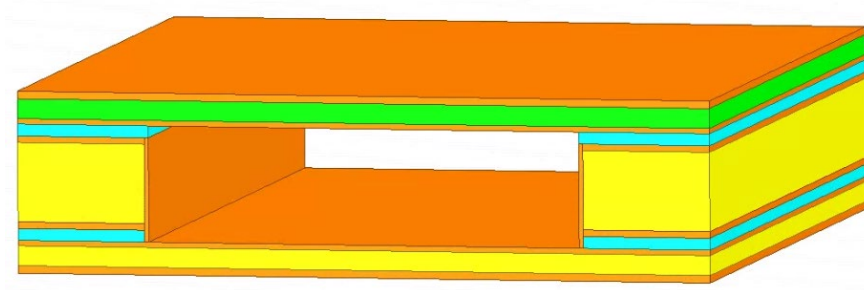
(a)



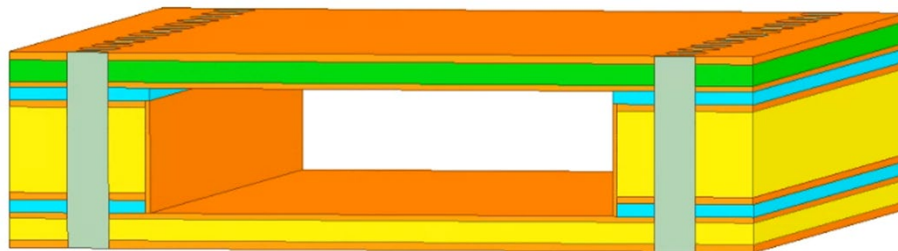
(b)



(c)



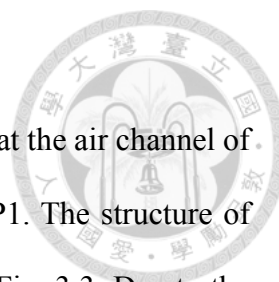
(d)



(e)

Fig. 3.2 The fabrication process of the AFSIW (a) step1 (b) step2 (c) step3 (d) step4 (e)

step5



The front view of the AFSIW is shown in Fig. 3.3. It's shown that the air channel of the AFSIW is formed by M2 to M5, the dug CORE2, and some PP1. The structure of AFSIW is like a T-shaped waveguide, which is the slash section in Fig. 3.3. Due to the fabrication process, there is a prepreg layer embedded in the top of the T-shaped structure (only on two sides, shown by the dot part in Fig. 3.3 slash section). We can still regard it as a traditional rectangular waveguide, as long as the prepreg sizes on two sides are not too large.

But compared with the waveguide equation derived in Chapter 2.1, there will be some slight errors on the properties of the AFSIW, such as the cutoff frequency, guided wavelength or propagation constant. And also, there will be a slight error on transmission loss. Those errors are caused by the T-shaped structure and the embedding prepreg. Since the width of the AFSIW is larger than the height of the AFSIW. The fundamental mode propagating in the AFSIW is TE_{10} mode.

The geometrical dimensions of the AFSIW is shown in Fig. 3.3 and Table 3.1. In Table 3.1, s is the pitch of the through-hole via.

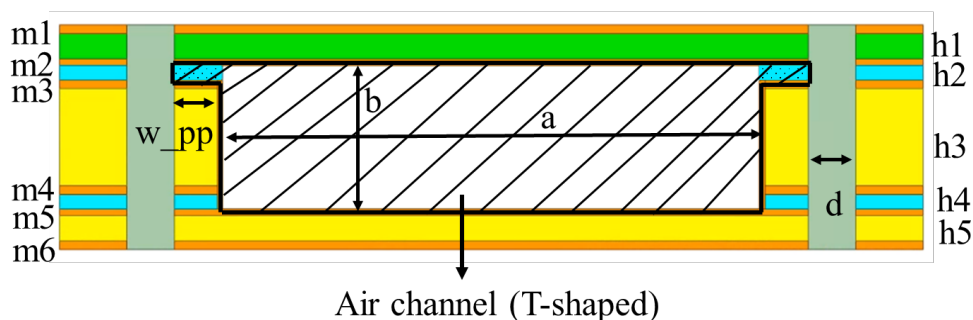
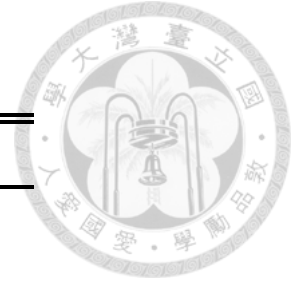


Fig. 3.3 The front view and geometrical dimensions of the AFSIW



Geometrical dimensions	
$h1, h5 = 5 \text{ mil}$	$m1, m6 = 48 \text{ um}$
$h2, h4 = 3 \text{ mil}$	$m2, m5 = 35 \text{ um}$
$h3 = 20 \text{ mil}$	$m3, m4 = 42 \text{ um}$
$a = 2.8 \text{ mm @}60\text{GHz}$	$d = 0.25 \text{ mm}$
$b = 0.744 \text{ mm}$	$s = 0.4 \text{ mm}$
	$w_{pp} = 0.3 \text{ mm}$

Table 3.1 The geometrical dimension of the AFSIW

However, when the Butler matrix is fabricated, some places are surrounded by air channels from three sides or all around. At this time, the above fabrication process might encounter some fabrication process problems which makes the AFSIW collapse. So, the other method must be used.

The modified method is that the PP1 is changed to the copper paste on step 4 and step 5 is removed because the copper paste forms the metal wall on the PP1 layer. The front view of the modified AFSIW is shown in the Fig. 3.4. The modified AFSIW is almost equal to the waveguide. So, the properties of the AFSIW, such as the cutoff frequency, guided wavelength or propagation constant, can use the waveguide equation derived on Chapter 2.1. Since the width of the AFSIW is larger than the height of the AFSIW. The fundamental mode propagating in the AFSIW is TE₁₀ mode. The geometrical dimensions of the AFSIW is shown in Fig. 3.4 and Table 3.2.

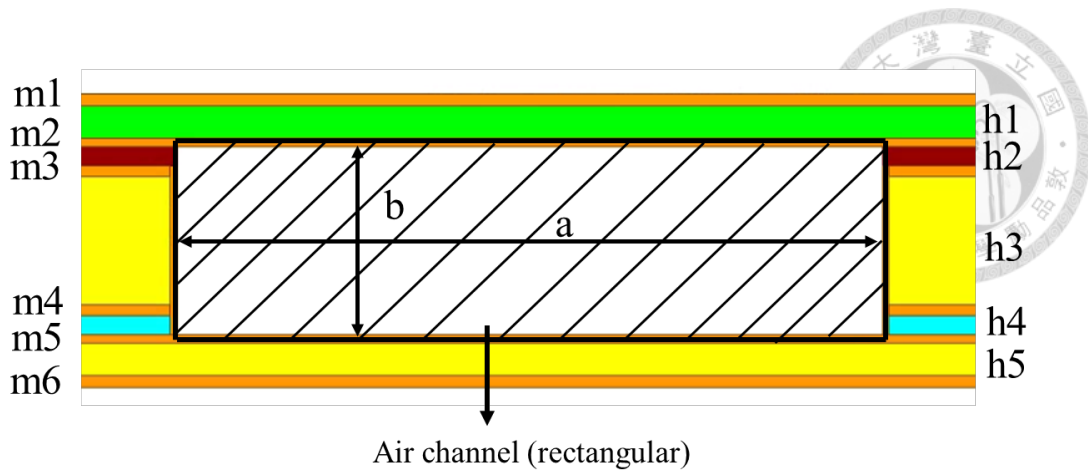


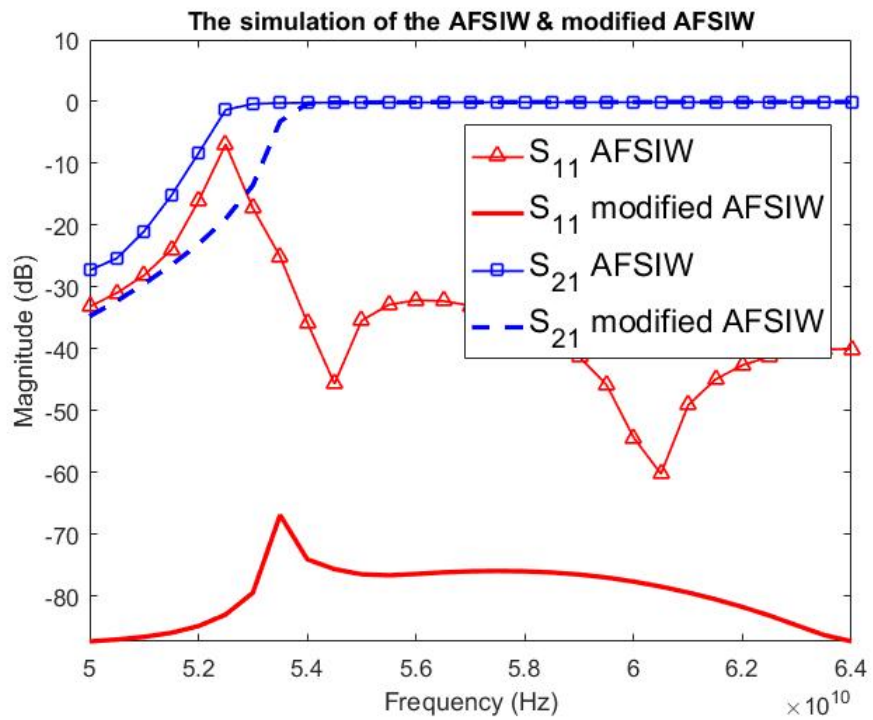
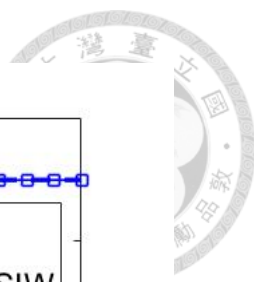
Fig. 3.4 The front view and geometrical dimensions of the modified AFSIW

Geometrical dimensions	
$h1, h5 = 5 \text{ mil}$	$m1, m6 = 48 \text{ um}$
$h2, h4 = 3 \text{ mil}$	$m2, m5 = 35 \text{ um}$
$h3 = 20 \text{ mil}$	$m3, m4 = 42 \text{ um}$
$a = 2.8 \text{ mm @}60\text{GHz}$	$b = 0.744 \text{ mm}$

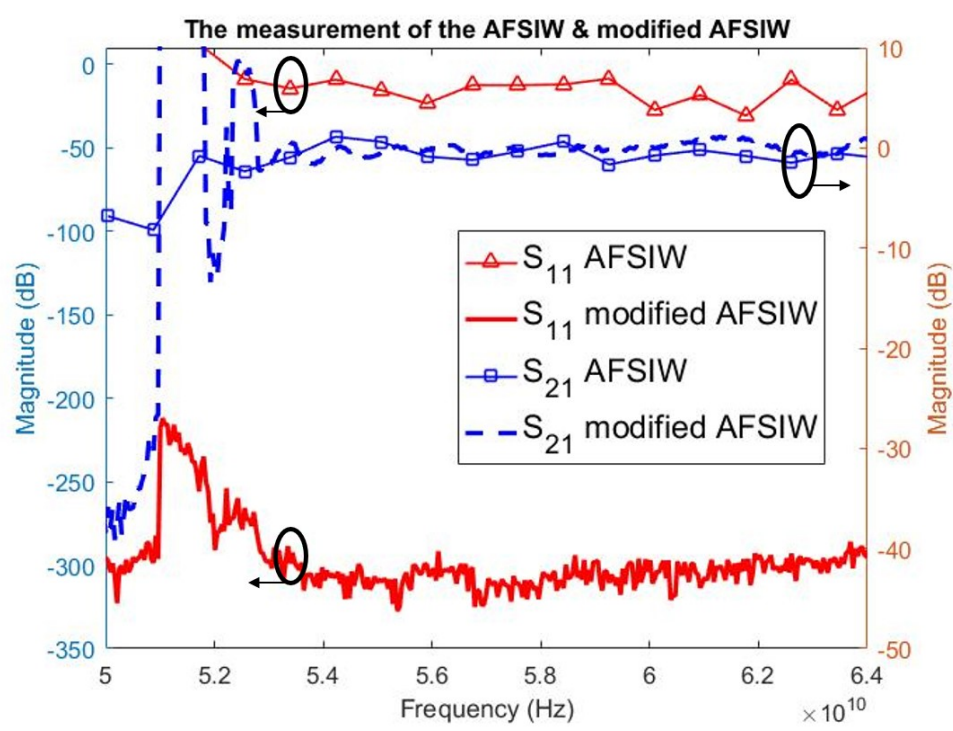
Table 3.2 The geometrical dimensions of the modified AFSIW

The simulation results and measurements of the AFSIW and modified AFSIW on HFSS software are shown in Fig. 3.5. In Fig. 3.5(a), it's shown that when the width of the AFSIW is 2.8mm, the cutoff frequency is equal to 52.3 GHz, which is not equal to the equation (2.15). But, when the width of the modified AFSIW is 2.8mm, the cutoff frequency is equal to 53.5 GHz, which matches the equation (2.15). The loss of the AFSIW and the modified AFSIW are 0.1 dB/cm and 0.064 dB/cm, respectively. These results verify that modified AFSIW doesn't include the prepreg and is similar to the waveguide, so loss is very low and the cutoff frequency the same as the waveguide.

In Fig. 3.5(b), the cutoff frequency of AFSIW and modified AFSIW are about 51.9 GHz and 52.9 GHz, respectively. The loss of the AFSIW and the modified AFSIW roughly are 0.16 dB/cm and 0.1dB/cm, respectively.



(a)



(b)

Fig. 3.5 The simulation and measurement of the AFSIW on HFSS (a) Simulation (b)

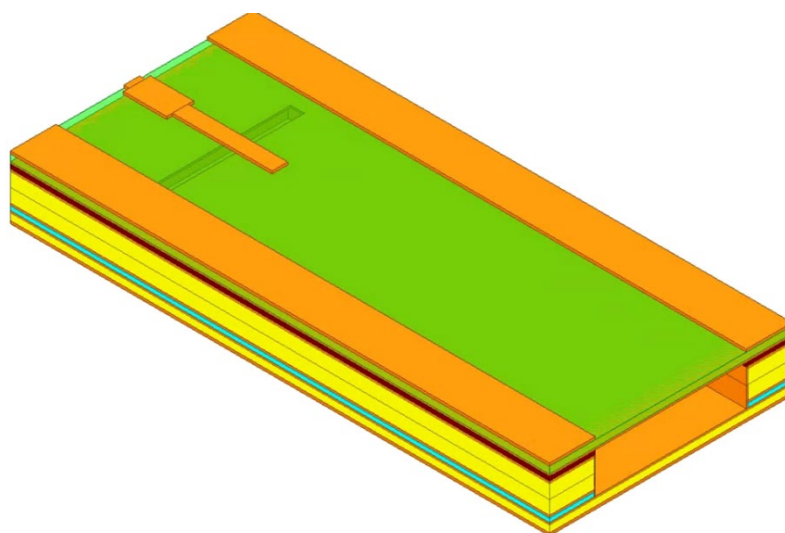
Measurement



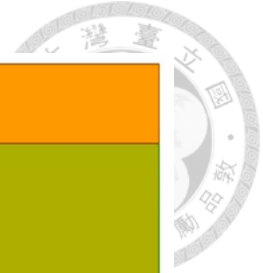
3.2 AFSIW Feeding

There are several methods for feeding the SIW, such as the transition between microstrip line to SIW with tapered microstrip feeding, by probe feeding or by slot coupling [31]. The slot coupling for feeding AFSIW is used in this thesis, which refers to [31] and [32] to design AFSIW feeding.

The design method of AFSIW feeding is introduced as follows. The signal of the microstrip line is at M1 and the ground of the microstrip line is at M2. The signal is propagated from M1 to the slot at M2 to couple into the air channel. There is a one-quarter wavelength open stub, which is used to short the microstrip line. The slot whose length is half-wavelength is used to make the power couple into the air channel to complete feeding. The structure of AFSIW feeding is shown in Fig. 3.6. In Fig. 3.6(c), the air channel is stepped because it makes the power easily couples into the air channel.



(a)



(b)



(c)

Fig. 3.6 The structure of the AFSIW feeding. (a) 3D view (b) Top view (c) Side view

The simulation results and measurement of AFSIW feeding on HFSS software are shown in Fig. 3.7. It's shown that the bandwidth (defined by S_{11} lower than -15 dB) is 58.3 to 62.3 GHz on simulation. The minimum loss of the feeding is about -0.37 dB on simulation. The bandwidth of the measured is 58.4 to 61.6 GHz. The measured minimum loss is about 0.4 dB.

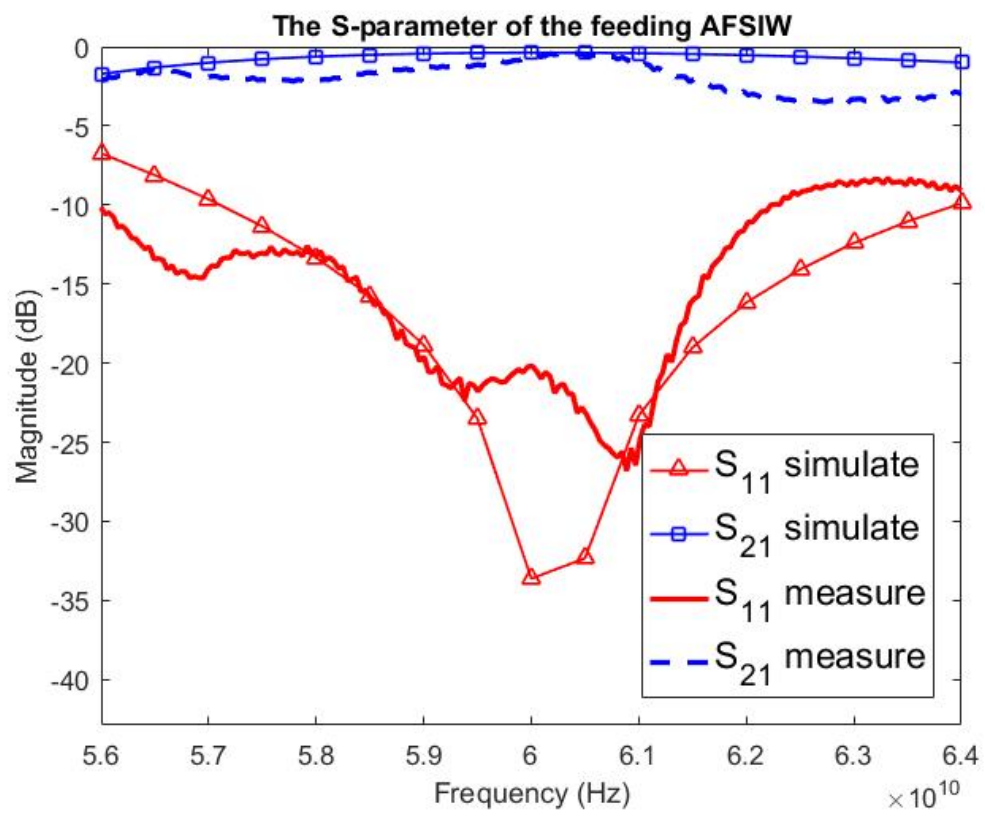


Fig. 3.7 The simulation results of AFSIW feeding on HFSS.



Chapter 4

AFSIW Stub Phase Shifter

Corresponding to the Butler matrix architecture in Fig. 2.6, the main goal of this chapter is to design a phase shifter which provides a 0/45-degree phase difference compared with the crossover. And in order to reduce the complexity of the path on Butler matrix circuit design and reduce the circuit size, the phase shifter should be designed with the same physical length of the crossover.

There are many methods to design the phase shifter on the SIW structure. However, in the AFSIW fabrication process, some methods will encounter some fabrication problems. Thus, this chapter will introduce the methods to design the phase shifter on the SIW structure and discuss the problems about these methods on the AFSIW structure. And the reason that the stub phase shifter is chosen in this thesis is explained. The stub phase shifter designed in AFSIW structure is analyzed. Next, the design rule of the proposed phase shifter is introduced.



4.1 Introduction of Stub Phase Shifter

Several typical methods for SIW phase shifter design are shown in Fig. 4.1. In Fig. 4.1, it is shown the top view of the SIW phase shifter.

The first method is a curved phase shifter as shown in Fig. 4.1(a). The curved phase shifter can achieve the requirements of the desired electrical length and the same physical length of the crossover. The disadvantage of this method is that the return loss is relatively poor. The second method can improve this disadvantage. The second method is the straight phase shifter which changes the width of the SIW to achieve the requirement of the desired electrical length, as shown in Fig. 4.1(b). Because the propagation constant is affected by the variation of the width of the SIW, the guided wavelength is also affected. So, the phase shifter with the desired electrical length and the same physical length of the crossover is proposed. The overall size of the second method is smaller than the first method.

But these methods will encounter some problems in the AFSIW fabrication process. For the first method, the curved line should be fabricated accurately. As soon as the curvature is wrong, the significant phase error will be provided. For the second method, if the minimum unit of the width of the SIW is too small, the fabrication process cannot be accurate. Thus, in order to avoid the above problems, we choose stub phase shifter for our design, as shown in Fig. 4.1(c).

Stub phase shifter doesn't require the accurate curvature and too precise unit width in the AFSIW fabrication process. And also, the stub phase shifter can be easily designed with desired electrical length and the same physical length of crossover. So, the stub type is chosen for the AFSIW Butler matrix design at this thesis.

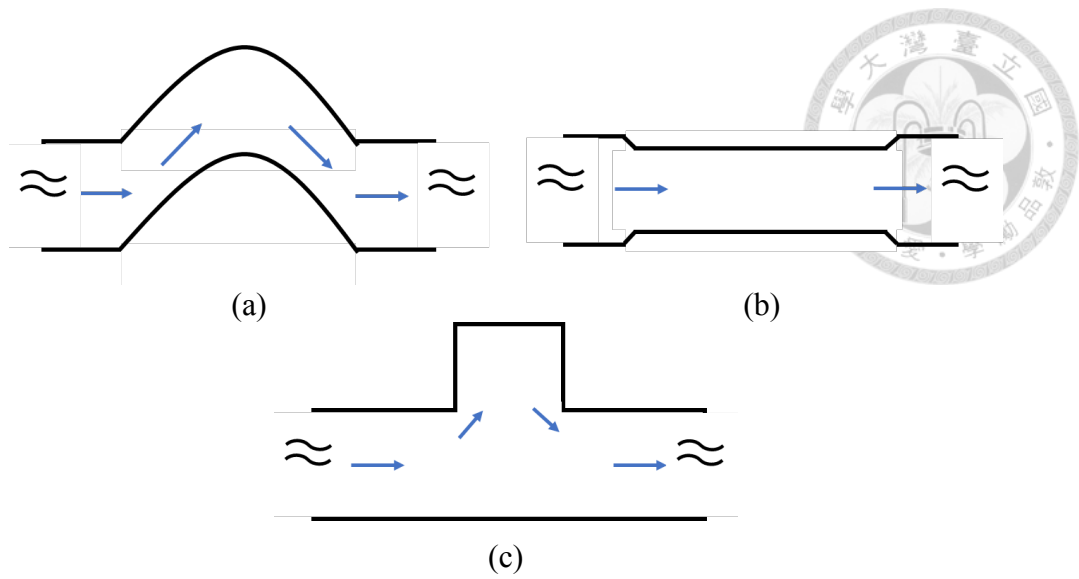


Fig. 4.1 Top view of SIW phase shifter (a) Curved phase shifter (b) Straight phase shifter (c) Stub phase shifter

As shown in Fig. 4.1(c), a short-ended or open-ended stub is connected to the middle of the original transmission line. The simple equivalent circuit for the stub phase shifter with short stub is shown in Fig. 4.2.

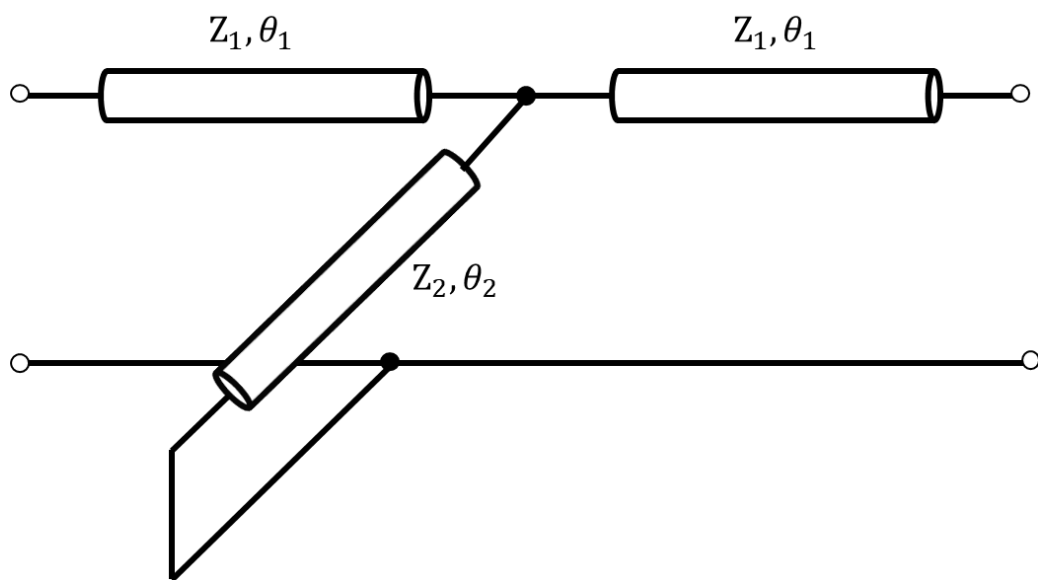
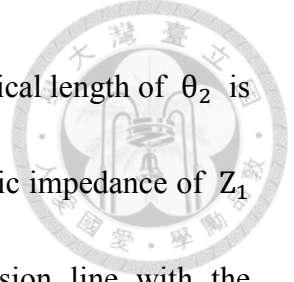


Fig. 4.2 The equivalent circuit of the stub phase shifter



A short stub with the characteristic impedance of Z_2 and electrical length of θ_2 is shunted in the middle of two transmission lines with the characteristic impedance of Z_1 and electrical length of θ_1 , which is equivalent to a transmission line with the characteristic impedance of Z_3 and electrical length of θ_3 . Then, the ABCD matrix of the transmission line and short stub is used to calculate the characteristic impedance of the transmission line and short stub, and the electrical length of the transmission line and short stub. The above derivation is shown in formula (4.1).

$$\begin{aligned} & \begin{bmatrix} \cos \theta_1 & jZ_1 \sin \theta_1 \\ j\frac{1}{Z_1} \sin \theta_1 & \cos \theta_1 \end{bmatrix} \begin{bmatrix} 1 & 0 \\ j \tan \theta_2 / Z_2 & 1 \end{bmatrix} \begin{bmatrix} \cos \theta_1 & jZ_1 \sin \theta_1 \\ j\frac{1}{Z_1} \sin \theta_1 & \cos \theta_1 \end{bmatrix} \\ &= \begin{bmatrix} \cos \theta_3 & jZ_3 \sin \theta_3 \\ j\frac{1}{Z_3} \sin \theta_3 & \cos \theta_3 \end{bmatrix} \end{aligned} \quad (4.1),$$

where $\begin{bmatrix} \cos \theta_i & jZ_i \sin \theta_i \\ j\frac{1}{Z_i} \sin \theta_i & \cos \theta_i \end{bmatrix}$ is the ABCD matrix of the transmission line, $i = 1, 3$.

$\begin{bmatrix} 1 & 0 \\ j \tan \theta_2 / Z_2 & 1 \end{bmatrix}$ is the ABCD matrix of the shunted short stub.

Then simplified the formula (4.1) as

$$\begin{aligned} & \begin{bmatrix} \cos 2\theta_1 + \frac{Z_1 \sin 2\theta_1}{2Z_2 \tan \theta_2} & j(Z_1 \sin 2\theta_1 + \frac{Z_1^2 \sin^2 \theta_1}{Z_2 \tan \theta_2}) \\ j(\frac{1}{Z_1} \sin 2\theta_1 - \frac{\cos^2 \theta_1}{Z_2 \tan \theta_2}) & \cos 2\theta_1 + \frac{Z_1 \sin 2\theta_1}{2Z_2 \tan \theta_2} \end{bmatrix} \\ &= \begin{bmatrix} \cos \theta_3 & jZ_3 \sin \theta_3 \\ j\frac{1}{Z_3} \sin \theta_3 & \cos \theta_3 \end{bmatrix} \end{aligned} \quad (4.2).$$

From formula(4.2), it can obtain three equation as following:

$$\cos 2\theta_1 + \frac{Z_1 \sin 2\theta_1}{2Z_2 \tan \theta_2} = \cos \theta_3 \quad (4.3)$$



$$Z_1 \sin 2\theta_1 + \frac{Z_1^2 \sin^2 \theta_1}{Z_2 \tan \theta_2} = Z_3 \sin \theta_3 \quad (4.4)$$

$$\frac{1}{Z_1} \sin 2\theta_1 - \frac{\cos^2 \theta_1}{Z_2 \tan \theta_2} = \frac{1}{Z_3} \sin \theta_3 \quad (4.5)$$

Equation (4.3) and (4.4) can be simplified as

$$Z_2 \tan \theta_2 = \frac{Z_1 \sin 2\theta_1}{2 \cos \theta_3 - 2 \cos 2\theta_1} \quad (4.6)$$

$$Z_2 \tan \theta_2 = \frac{Z_1^2 \sin^2 \theta_1}{Z_3 \sin \theta_3 - Z_1 \sin 2\theta_1} \quad (4.7)$$

Equation (4.6) and (4.7) can obtain the Z_1 equal

$$Z_1 = \frac{Z_3 \sin \theta_3 \cot \theta_1}{\cos \theta_3 + 1} \quad (4.8)$$

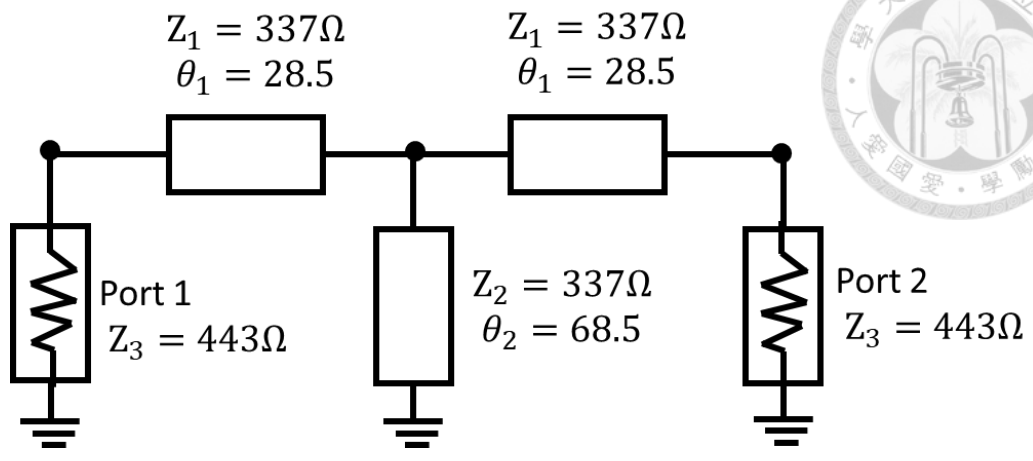
Then, equation (4.4) and (4.5) can be simplified as

$$Z_2 \tan \theta_2 = \frac{Z_1^2 Z_3}{(Z_3^2 - Z_1^2) \sin \theta_3} \quad (4.9)$$

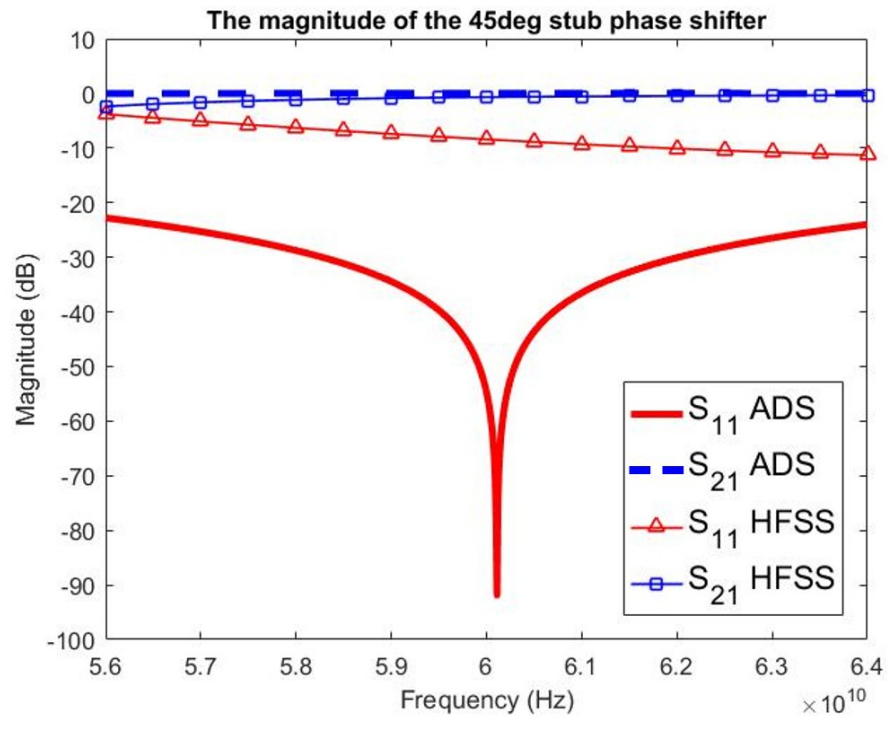
The Z_3 and θ_3 of the transmission line is known from the desired transmission line.

Assume the Z_2 and θ_1 , then using equation (4.8) and (4.9) can obtain the Z_1 and θ_2 .

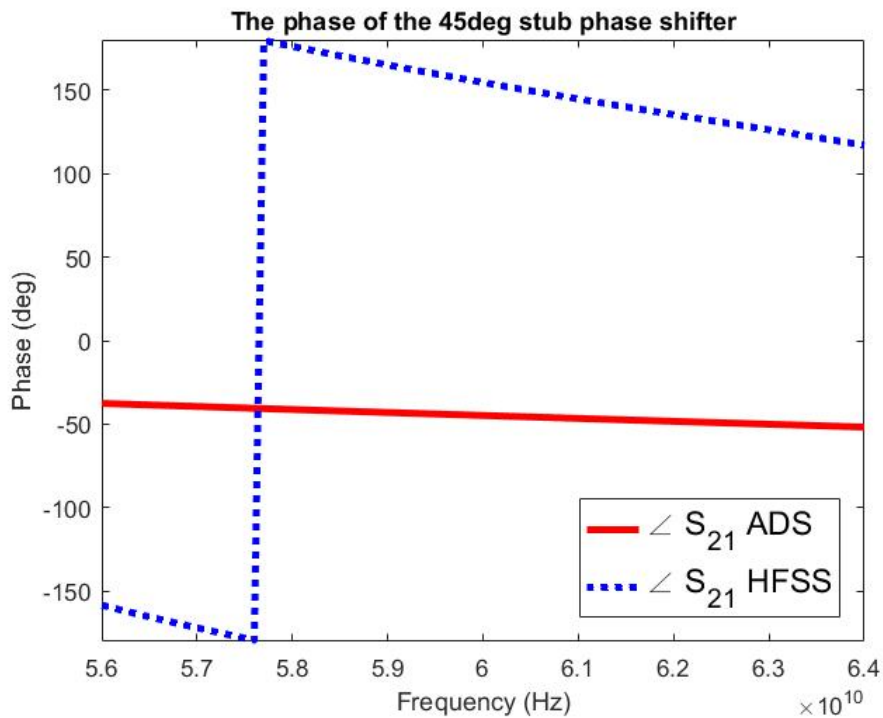
For example, we can choose the target impedance and phase as $Z_3 = 443 \Omega$ and $\theta_3 = 45^\circ$ and also assume $Z_2 = 337 \Omega$ and $\theta_1 = 28.5^\circ$ are given. Then, the $Z_1 = 337 \Omega$ and $\theta_2 = 68.5^\circ$ is obtained by the equation (4.8) and (4.9). The ADS software is used to verify this data. And also, we can transfer impedance and phase to corresponding structural parameters in AFSIW to simulate a stub phase shifter in HFSS. The results are shown in Fig. 4.3.



(a)



(b)

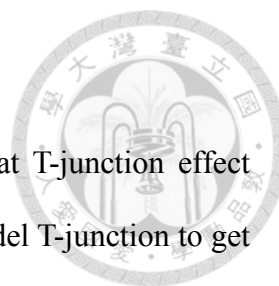


(c)

Fig. 4.3 Use the ADS and HFSS to simulate the stub phase shifter (a) ADS circuit (b)

Magnitude (c) Phase

From Fig. 4.3, it's shown that the S_{11} of ADS is very deep at the 60 GHz, the S_{21} of ADS is close to 0 dB and the phase is clearly at -45° . So, following the design flow mentioned above, we can design an ideal stub phase shifter. But the simulation results of the HFSS don't match the results of the ADS. Thus, it implies that the T-junction effect on the AFSIW might not be ignored in the model of phase shifter. In the next section, we will discuss and analyze the model of AFSIW stub phase shifter.



4.2 Analysis of Stub Phase Shifter in AFSIW

From Fig. 4.3(b) and (c), the mismatch of results implies that T-junction effect should be taken into consideration. In this section, we will try to model T-junction to get a revised equivalent circuit model for phase shifter.

The T-junction in the waveguide is discussed by the waveguide handbook [33]. There are two types of T-junction in the waveguide. One is the E-plane T-junction, another is the H-plane T-junction. In the waveguide, the E-plane T-junction is extended in the height direction (E-plane). The H-plane T-junction is extended in the width direction (H-plane). They are shown in Fig. 4.4.

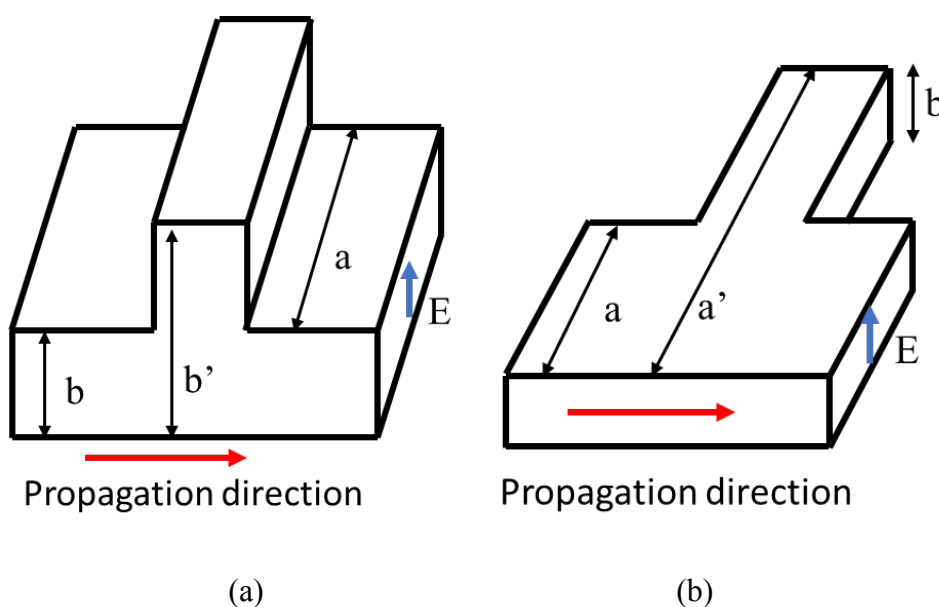


Fig. 4.4 (a) E-plane T-junction (b) H-plane T-junction

The E-plane T-junction might encounter some problems in the AFSIW fabrication process. First, the substrate thickness cannot fit the desired height. Second, the fabrication for connecting the AFSIW different layers is difficult. So, the H-plane is the best choice for design. The equivalent circuit of the H-plane T-junction in the waveguide is shown in Fig. 4.5. The stub is not included in the equivalent circuit of the T-junction in Fig. 4.5.

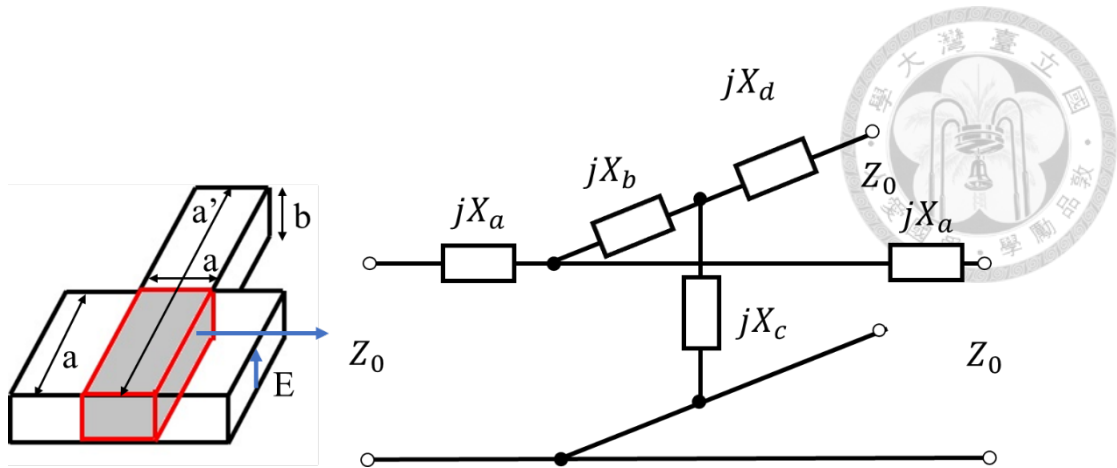


Fig. 4.5 The equivalent circuit of H-plane T-junction

From Fig. 4.5, two impedance of jX_a are shunted a series of complex circuits in the middle, which is composed of jX_b , jX_c and jX_d . The ABCD matrix of the T-junction is equal to

$$\begin{bmatrix} A_{\text{junction}} & B_{\text{junction}} \\ C_{\text{junction}} & D_{\text{junction}} \end{bmatrix} = \begin{bmatrix} 1 & jX_a \\ 0 & 1 \end{bmatrix} \begin{bmatrix} 1 & 0 \\ jX_b + \frac{1}{\frac{1}{jX_c} + \frac{1}{jX_d}} & 1 \end{bmatrix} \begin{bmatrix} 1 & jX_a \\ 0 & 1 \end{bmatrix} \quad (4.10),$$

where the equations about X_a, X_b, X_c, X_d are shown as following.

$$\frac{Z_0}{X_a} = \frac{1}{X_1} = \frac{\lambda_g}{2a} \left[x \cot \frac{\pi x}{2} - 0.0103 - \frac{\left(\frac{4}{5\pi} \frac{1+x^2}{4-x^2} + 0.2614 \right)^2}{\sqrt{3-x^2} - 0.0694} \right] \quad (4.11)$$

$$\frac{X_a + 2X_b + 2X_c}{Z_0} = X_2 = \frac{2a}{\lambda_g} \left[-\frac{A}{AC + B^2} - 0.057 + \frac{0.085}{1.62 - x^2} \right] \quad (4.12)$$

$$-\frac{2X_c}{Z_0} = X_3 = \frac{2a}{\lambda_g} \left(\frac{B}{AC + B^2} \right) \quad (4.13)$$

$$\frac{2X_d}{Z_0} = X_3 + X_4 = \frac{2a}{\lambda_g} \left(\frac{B + C}{AC + B^2} \right) \quad (4.14)$$

$$x = \frac{2a}{\lambda_g} \quad (4.15)$$



$$A = \frac{x}{2} \cot(\pi x) - 0.0322 \quad (4.16)$$

$$B = \frac{1}{\pi} \frac{1+x^2}{1-x^2} + 0.3246 \quad (4.17)$$

$$C = x \tan \frac{\pi x}{2} + 0.0195 \quad (4.18)$$

There are some limits to these equations. First, the wavelength should be inside the range between the width of the waveguide and twice the width of the waveguide ($a < \lambda < 2a$). Second, if the waveguide is in the range of $0 < 2a/\lambda_g < 1$, the error will be less than 15 percent. Third, the width of the junction's three-port should be the same width.

For the short-ended stub phase shifter, the short stub with the characteristic impedance of Z_1 and electrical length of θ_2 is connected after the impedance of jX_d . This circuit is called the middle network here. The equivalent circuit is shown in Fig. 4.6.

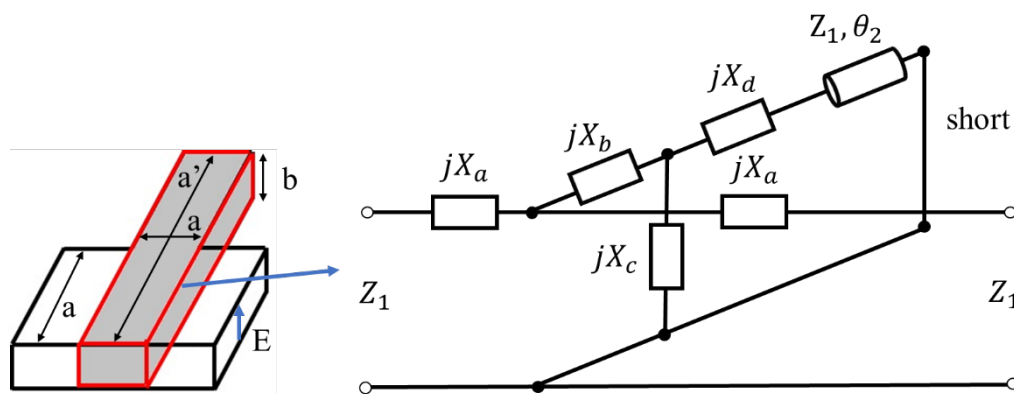
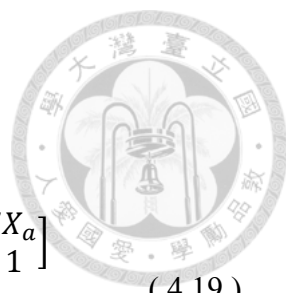


Fig. 4.6 The equivalent circuit of H-plane T-junction with short stub

The ABCD matrix of the middle network is equal to

$$= \begin{bmatrix} 1 & jX_a \\ 0 & 1 \end{bmatrix} \begin{bmatrix} A_{middle} & B_{middle} \\ C_{middle} & D_{middle} \end{bmatrix} \begin{bmatrix} 1 & 0 \\ jX_b + \frac{1}{\frac{1}{jX_c} + \frac{1}{j(X_d + Z_1 \tan \theta_2)}} & 1 \end{bmatrix} \begin{bmatrix} 1 & jX_a \\ 0 & 1 \end{bmatrix} \quad (4.19).$$


Then, as shown in the region BB'- CC' and DD'- EE' in Fig. 4.7, two sides of the middle network are extended to form a stub phase shifter with the characteristic impedance of Z_3 and the electrical length of θ_3 . And this circuit is called the unfinished (UF) network here. The ABCD matrix of the UF network can be obtained by

$$\begin{bmatrix} A_{UF} & B_{UF} \\ C_{UF} & D_{UF} \end{bmatrix} = \begin{bmatrix} \cos \theta_3 & jZ_3 \sin \theta_3 \\ j \frac{1}{Z_3} \sin \theta_3 & \cos \theta_3 \end{bmatrix}$$

$$= \begin{bmatrix} \cos \theta_1 & jZ_1 \sin \theta_1 \\ j \frac{1}{Z_1} \sin \theta_1 & \cos \theta_1 \end{bmatrix} \begin{bmatrix} A_{middle} & B_{middle} \\ C_{middle} & D_{middle} \end{bmatrix} \begin{bmatrix} \cos \theta_1 & jZ_1 \sin \theta_1 \\ j \frac{1}{Z_1} \sin \theta_1 & \cos \theta_1 \end{bmatrix} \quad (4.20).$$

As shown in (4.20), the stub phase shifter equivalent to the waveguide with the characteristic impedance of Z_3 and the electrical length of θ_3 . Two sides of the overall short-ended stub phase shifter should be designed with the characteristic impedance of Z_3 to match the UF network. As shown in the region AA'- BB' and EE'- FF' in Fig. 4.7, two sides of the UF network are connected to the waveguide with the characteristic impedance of Z_3 and the electrical length of θ_4 . So, the equivalent circuit of the overall short-ended stub phase shifter is completed. It's shown in Fig. 4.7.

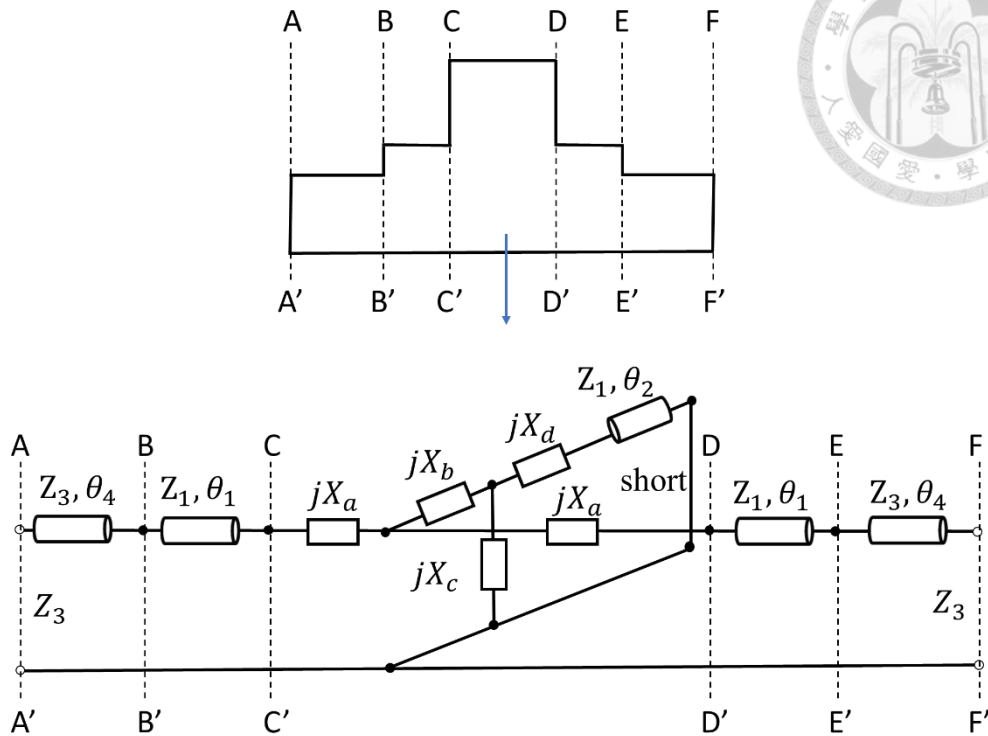


Fig. 4.7 The equivalent circuit of the overall short-ended stub phase shifter

The ABCD matrix of the overall short-ended stub phase shifter is given by

$$\begin{aligned}
 \begin{bmatrix} A_{overall} & B_{overall} \\ C_{overall} & D_{overall} \end{bmatrix} &= \begin{bmatrix} \cos \theta_5 & jZ_3 \sin \theta_5 \\ j \frac{1}{Z_3} \sin \theta_5 & \cos \theta_5 \end{bmatrix} \\
 &= \begin{bmatrix} \cos \theta_4 & jZ_3 \sin \theta_4 \\ j \frac{1}{Z_3} \sin \theta_4 & \cos \theta_4 \end{bmatrix} \begin{bmatrix} A_{UF} & B_{UF} \\ C_{UF} & D_{UF} \end{bmatrix} \begin{bmatrix} \cos \theta_4 & jZ_3 \sin \theta_4 \\ j \frac{1}{Z_3} \sin \theta_4 & \cos \theta_4 \end{bmatrix} \quad (4.21).
 \end{aligned}$$

As shown in (4.21), the overall short-ended stub phase shifter equivalents to the waveguide with the characteristic impedance of Z_3 and the electrical length of θ_5 .

4.2.1 Design Procedure

As shown in Fig. 4.7 and formula (4.21), except the parameters Z_3 and θ_5 are known, the others ($Z_1, \theta_1, \theta_2, \theta_4, jX_a, jX_b, jX_c, jX_d$) are unknown. Thus, we

determine the width of the T-junction in waveguide (a_1) at first to obtain the parameters of the junction (jX_a, jX_b, jX_c, jX_d) and the characteristic impedance (Z_1). Second, the θ_1, θ_2 and θ_4 are calculated in MATLAB. The detailed procedure is listed as follows:

Step 1: The characteristic impedance of the waveguide is related to the width of the waveguide. When the fundamental mode of the waveguide is the TE_{10} mode, the characteristic impedance of the waveguide is equal to [34]

$$Z_{0,TE_{10}} = \frac{\frac{2b}{a} \sqrt{\frac{\mu_0}{\epsilon_0 \epsilon_r}}}{\sqrt{1 - \left(\frac{f_c}{f}\right)^2}} \quad (4.22),$$

where a is the width of the waveguide, and b is the height of the waveguide.

As shown in formula (4.11) - (4.18), the parameters jX_a, jX_b, jX_c, jX_d are related to the width of the T-junction in waveguide (a_1) with the characteristic impedance of Z_1 .

Thus, if the width of the T-junction in waveguide (a_1) is determined, only parameters θ_1, θ_2 and θ_4 are unknown.

Step 2: Since the physical length of the phase shifter is same to the physical length of the crossover, θ_4 can be simplified as

$$\theta_4 = \frac{l_{cross} - a_1 - 2 \left(\lambda_{g,a_1} \times \frac{\theta_1}{360} \right)}{2} \times \frac{360}{\lambda_{g,a_3}} \quad (4.23),$$

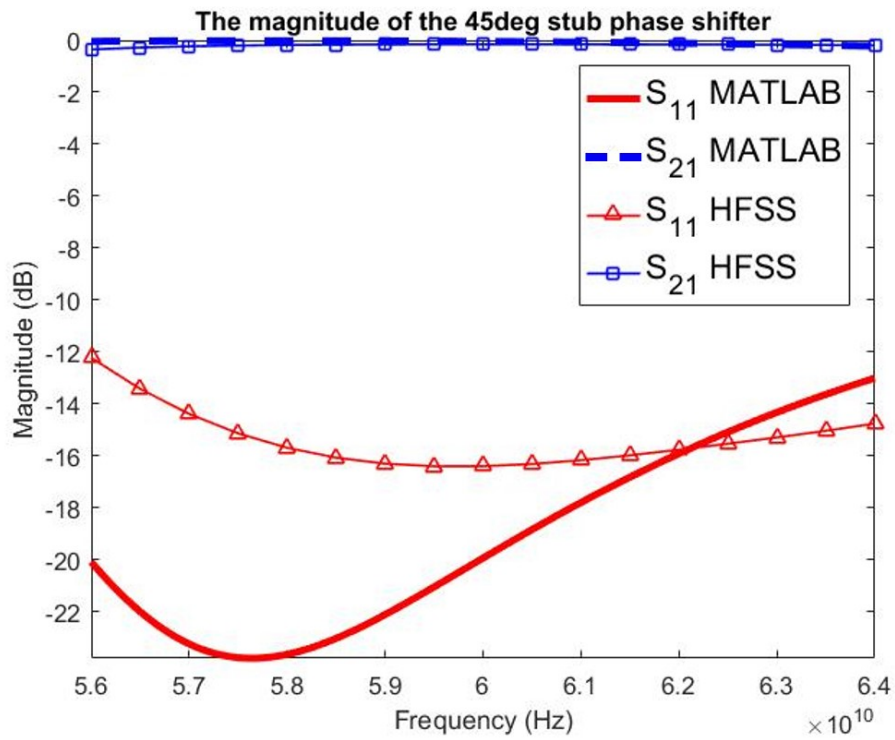
where l_{cross} is the physical length of the crossover, λ_{g,a_i} is the guided wavelength of the waveguide with the characteristic impedance of Z_i , where $i = 1, 3$.

The parameters θ_1 , θ_2 and θ_4 are calculated by the formula (4.11) - (4.23) in MATLAB. Thus, the overall short-ended stub phase shifter is designed.

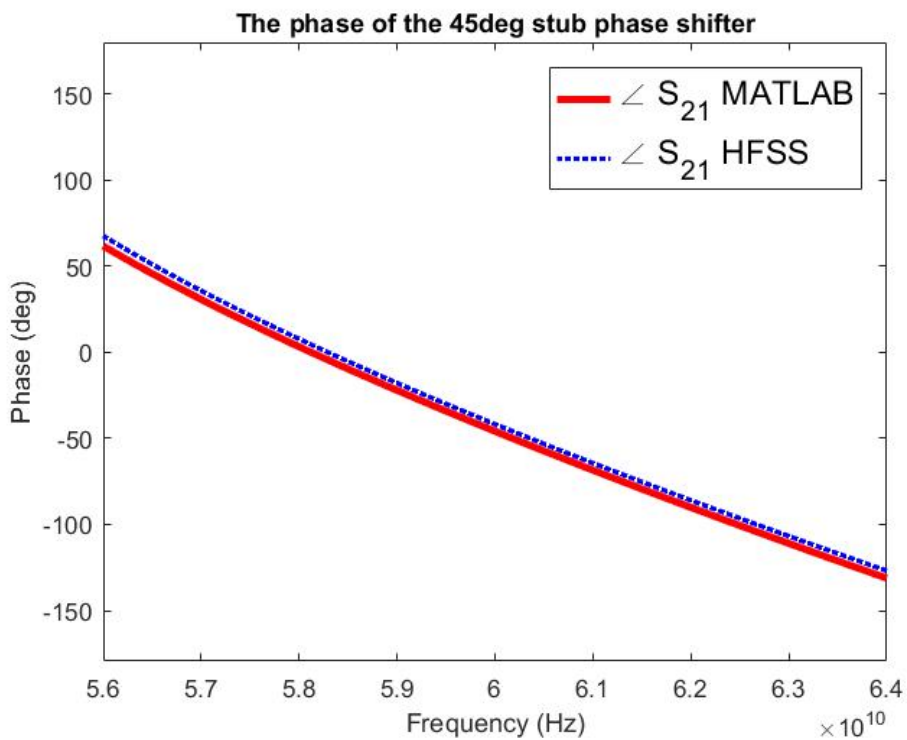
For example, given the height of the waveguide b is 0.744mm and the width of the waveguide a_3 is 2.8mm, the characteristic impedance of the waveguide $Z_3 = 445\Omega$ at $f = 60$ Hz can be calculated by formula (4.22). And we set the desired phase (θ_5) shift from the phase shifter to be 45 degree. Then we can start to analyze the UF network part.

First, we assume the width of the T-junction in waveguide (a_1) is 3mm. Second, $\theta_1 = 70^\circ$ and $\theta_2 = 40^\circ$ are calculated by the formula (4.11) - (4.23) in MATLAB. The desired stub phase shifter is proposed. This example is simulated and verified by HFSS. The results of the MATLAB and the HFSS are shown in Fig. 4.8.

In Fig. 4.8, the result of HFSS is slightly mismatched with the result of MATLAB. As mentioned from [33], there is a 15 percent error on the T-junction. But overall, the result of HFSS and the result of MATLAB are roughly the same. The magnitude of the S21 of the HFSS is -0.15 dB at 60 GHz. The magnitude of the S21 of the MATLAB is -0.04 dB at 60 GHz. The phase of the S21 of the HFSS is -41.8° at 60 GHz. The phase of the S21 of the MATLAB is -45.8° at 60 GHz.



(a)



(b)

Fig. 4.8 The 45-degree stub phase shifter compared by HFSS and MATLAB

(a) Magnitude (b) Phase



4.3 AFSIW Stub Phase Shifter Design

From the previous verification, the formula (4.10) - (4.23) can be used to design the stub phase shifter. According to the Butler matrix concept in Fig. 2.6, the phase of the proposed stub phase shifter should be compared to the phase of crossover. Also, for a compact design, we have to restrict the physical length of the stub phase shifter to the same length of the crossover. With these criterions, the design formula in (4.10) - (4.23) and the design flow mentioned in 4.2.1 can be used to find the rough value of parameters Z_1 , θ_1 , θ_2 by MATLAB. With these rough values, we can further use HFSS to optimize the performance of the stub phase shifter.

The configuration of the theoretical phase shifter is shown in Fig. 4.9. The geometrical dimensions of the theoretical 0-degree phase shifter and 45-degree phase shifter are summarized in Table 4.1. Then, the results of the HFSS are shown in Fig. 4.10. We know the phase of the proposed crossover is -47.1° , and the detailed design of the proposed crossover will be discussed in the next chapter.

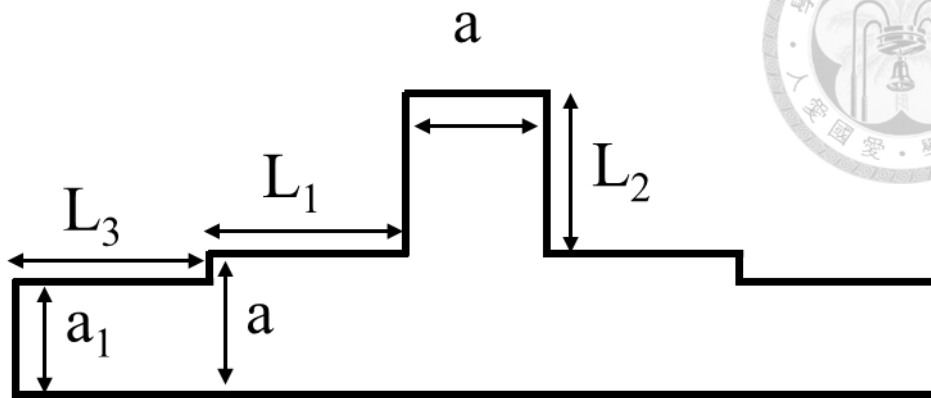
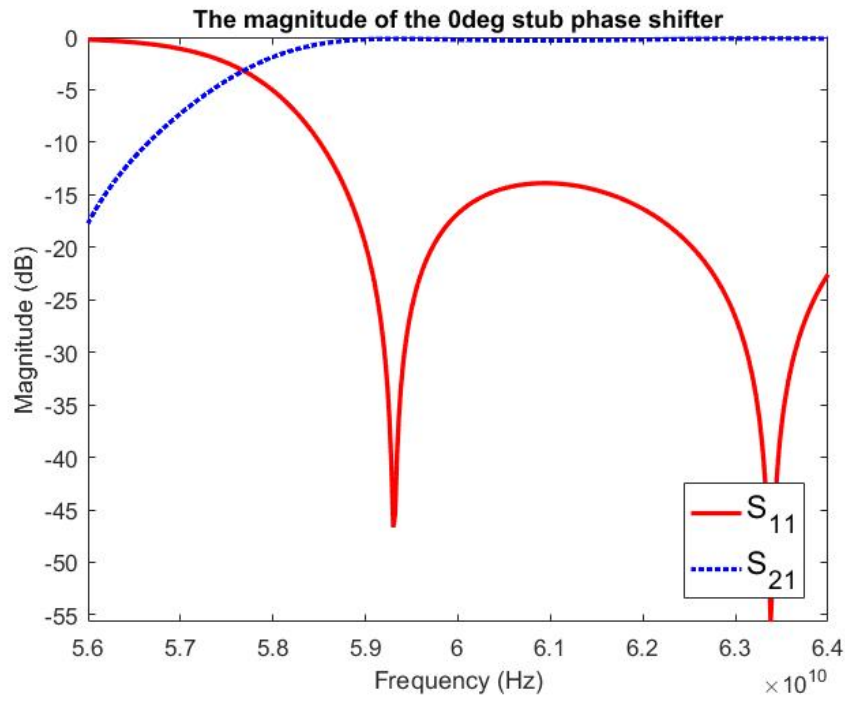
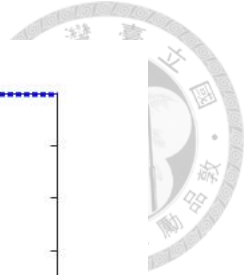


Fig. 4.9 The configuration of top view of the theoretical phase shifter

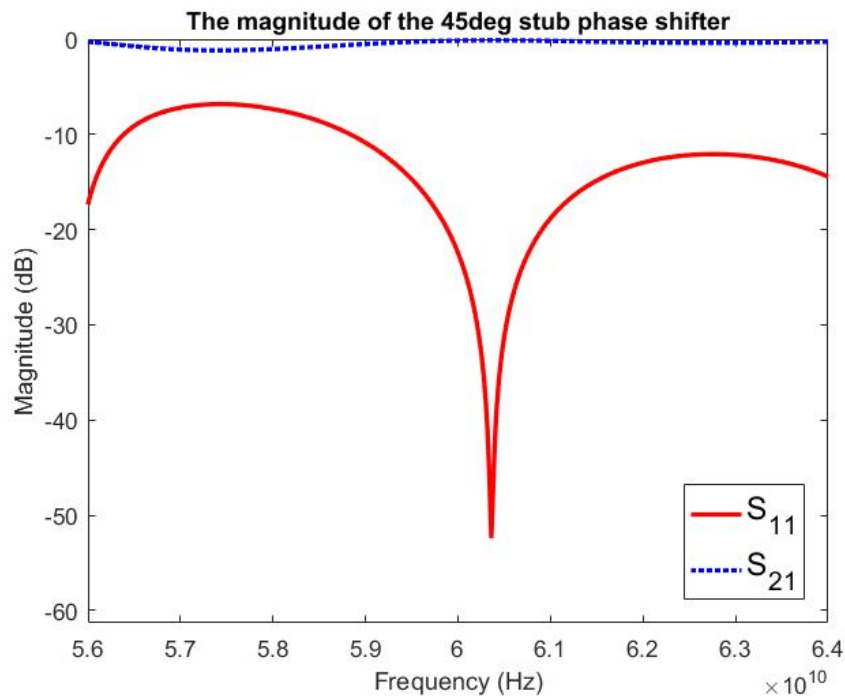
	0 deg phase shifter	45 deg phase shifter
a	3.5 mm	3.5 mm
a_1	2.8 mm	2.8 mm
L_1	6.5 mm	7.4 mm
L_2	3.4 mm	4.0 mm
L_3	4.7 mm	3.8 mm

Table 4.1 Geometrical dimensions of the theoretical phase shifter.

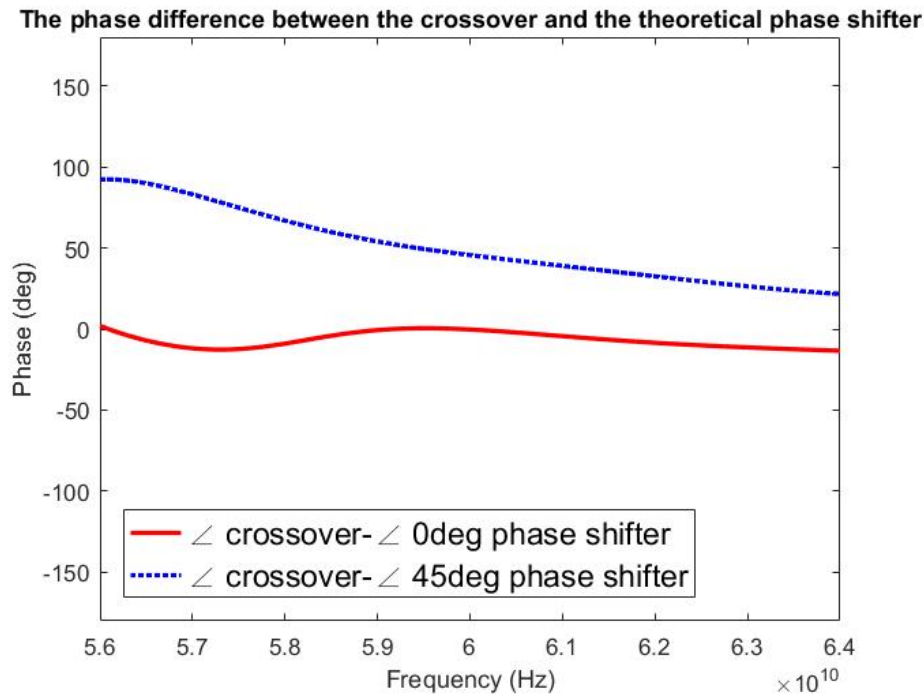
In Fig. 4.10, the magnitude of the S_{21} of the 0-deg phase shifter is -0.22 dB at 60 GHz. The magnitude of the S_{21} of the 45-deg phase shifter is -0.15 dB at 60 GHz. The bandwidth (defined by the desired phase difference $\pm 5^\circ$) of the phase difference between the crossover and the 0-degree phase shifter is between 58.4 to 61.1 GHz. The bandwidth (defined by the desired phase difference $\pm 5^\circ$) of the phase difference between the crossover and the 45-degree phase shifter is between 59.4 to 60.8 GHz.



(a)



(b)



(c)

Fig. 4.10 The theoretical phase shifter (a) 0-deg phase shifter magnitude (b) 45-deg phase shifter magnitude (c) the phase difference between the crossover and the 0/45-deg phase shifter

The theoretical phase shifters in Table 4.1 are the theoretical cases. After these, parameter analysis and some optimizations are done to find whether there is better performance. The most influential part is that if the width of the junction is larger than the junction limit from [33] ($0 < 2a/\lambda_g < 1$), the bandwidth (defined by S_{11} lower than -15 dB) will be better in some cases. As a result, we can try to set the width of the stub as a new variable to get an AFSIW stub phase shifter with larger bandwidth.

The configuration of the proposed tuning phase shifter is shown in Fig. 4.11. The geometrical dimensions of the proposed tuning 0-degree phase shifter and 45-degree phase shifter are summarized in Table 4.2. Then, the result of the HFSS is shown in Fig. 4.12. We know the phase of the proposed crossover is -146.6° .

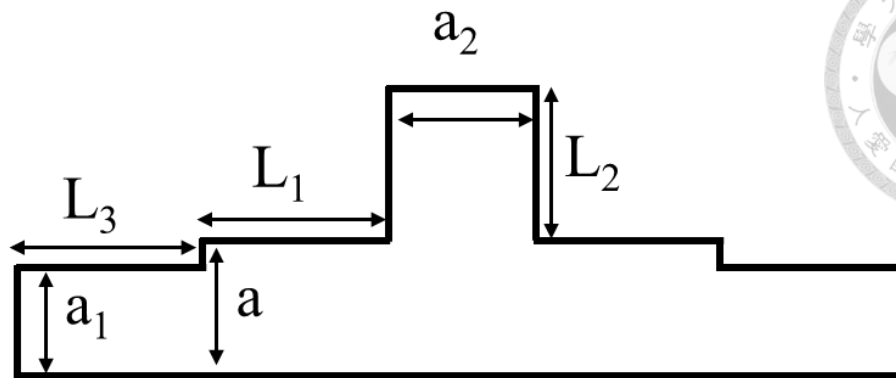


Fig. 4.11 The configuration of top view of the proposed tuning phase shifter

	0 deg phase shifter	45 deg phase shifter
a	4.2 mm	4 mm
a_1	2.8 mm	2.8 mm
a_2	3 mm	4 mm
L_1	4.1 mm	5.6 mm
L_2	1.8 mm	2.5 mm
L_3	3.35 mm	1.35 mm

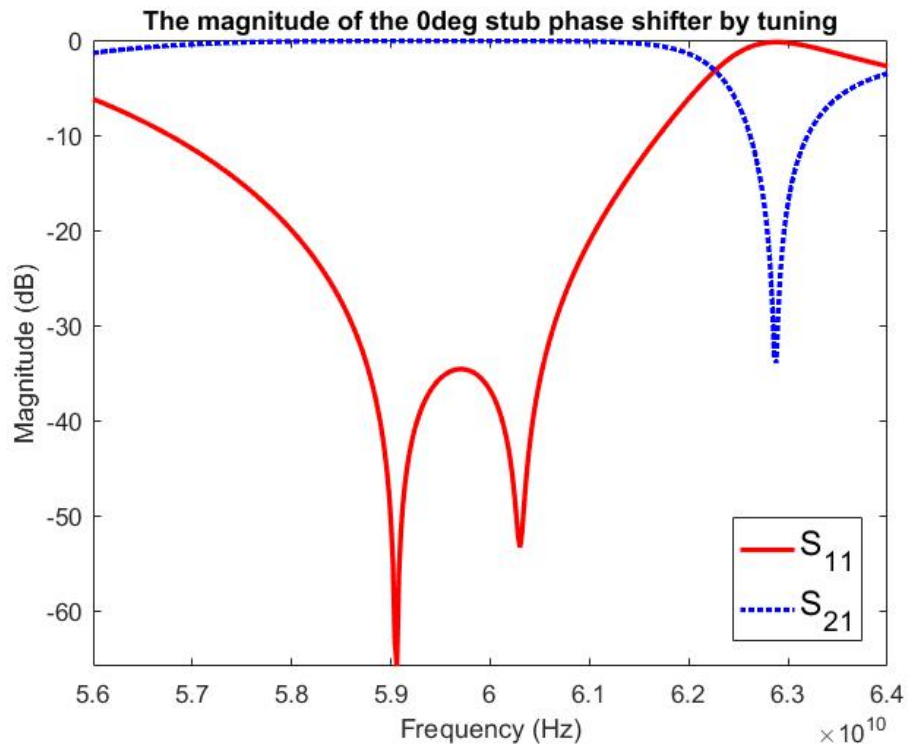
Table 4.2 Geometrical dimensions of the proposed tuning phase shifter.

In Fig. 4.12, the magnitude of the S_{21} of the 0-deg phase shifter is -0.09 dB at 60 GHz. The magnitude of the S_{21} of the 45-deg phase shifter is -0.08 dB at 60 GHz. The bandwidth (defined by the desired phase difference $\pm 5^\circ$) of the phase difference between the crossover and the 0-degree phase shifter is between 57.2 to 61.2 GHz. The bandwidth (defined by the desired phase difference $\pm 5^\circ$) of the phase difference between the crossover and the 45-degree phase shifter is between 58.4 to 62 GHz.

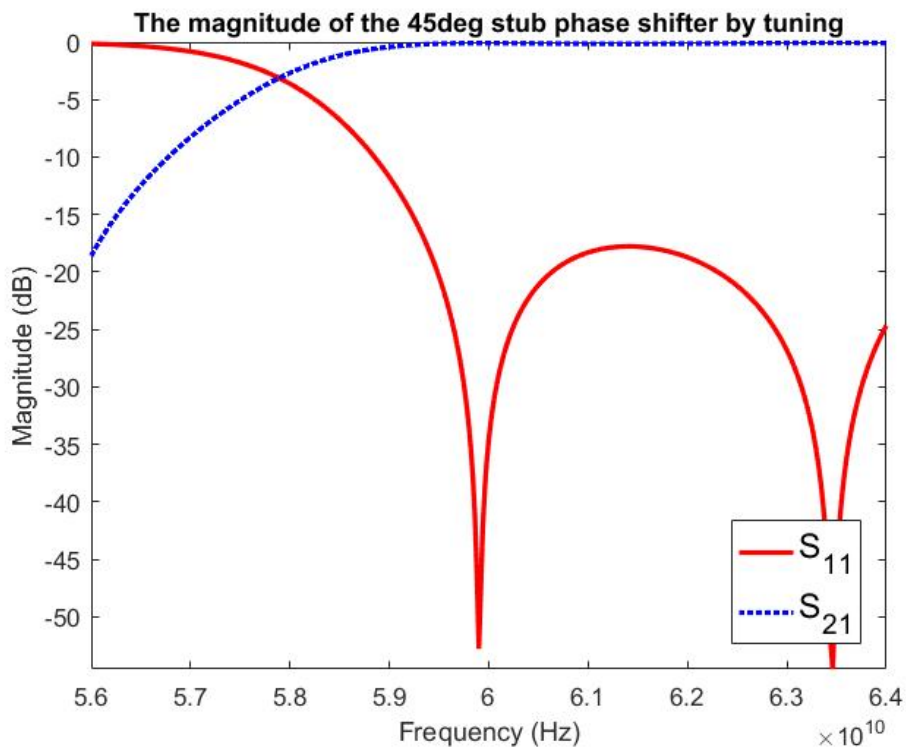
From Fig. 4.10(c) and Fig. 4.12(c), the phase of tuning phase shifter is flatter than the theoretical phase shifter. Because the tuning phase shifter has one more variable

compared to the theoretical case, where the widths of the junction (a and a_2 in Fig. 4.11)

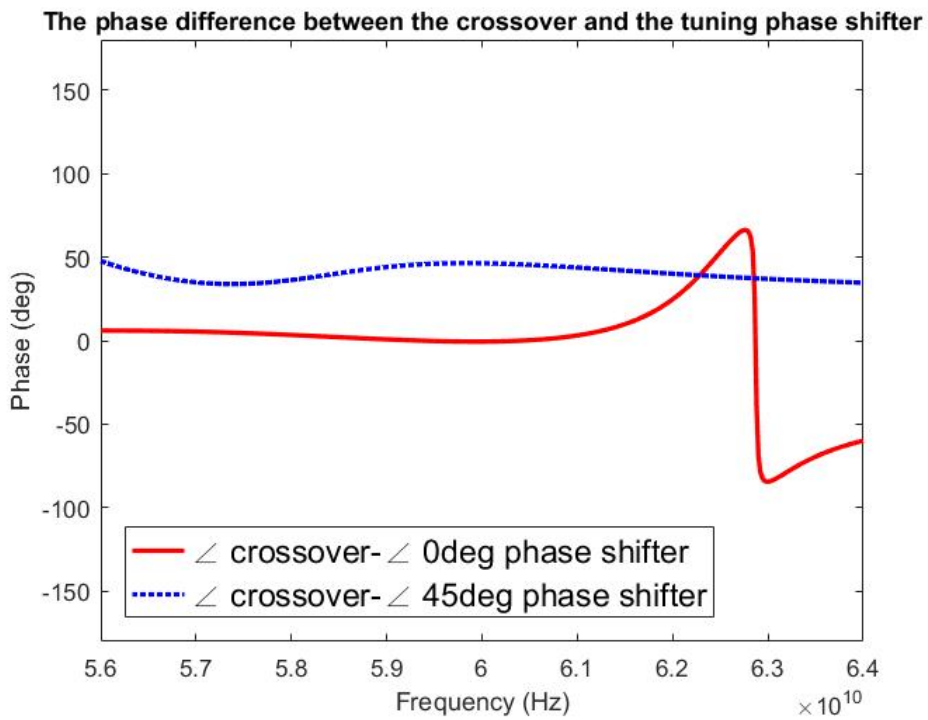
should be the same according to the restriction of the theory.



(a)



(b)



(c)

Fig. 4.12 The proposed tuning phase shifter (a) 0-deg phase shifter magnitude (b) 45-deg phase shifter magnitude (c) the phase difference between the crossover and the



4.4 **Measurement and Discussion**

The photographs of the proposed phase shifters are shown in Fig. 4.13. Fig. 4.13 shows the 0/45-deg theoretic phase shifter and the 0/45-deg tuning phase shifter. The measured and simulated results of the 0-deg tuning phase shifter without calibration are shown in Fig. 4.14. It's shown that the S_{21} of the measured result is below than -15 dB. Thus, we guess that there might be some serious structural error in manufacturing process, such as the collapse of air channel or the copper paste flowing into the air channel. When some parts of the slot in feeding part are blocked by the copper paste, it will cause radiation and radiation loss. As shown in Fig. 4.15, the slot of B region is black which represents the copper paste.

It is necessary to check the cross-section cut of the phase shifter to find the actual reason of the failure for future research. Since the 0/45-deg theoretic phase shifter and the 0/45-deg tuning phase shifter are both failed, we only show the measurement of the 0/45-deg tuning phase shifter.

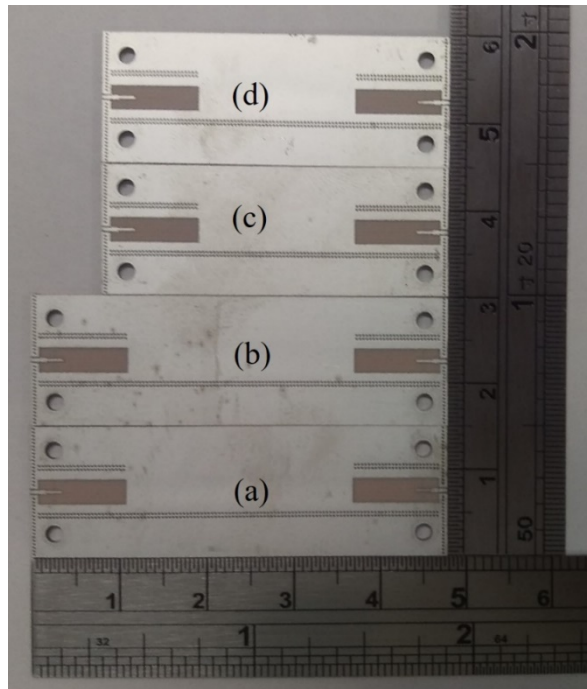


Fig. 4.13 The photograph of the proposed phase shifters. (a) 0-deg theoretic (b) 45-deg theoretic (c) 0-deg tuning (d) 45-deg tuning

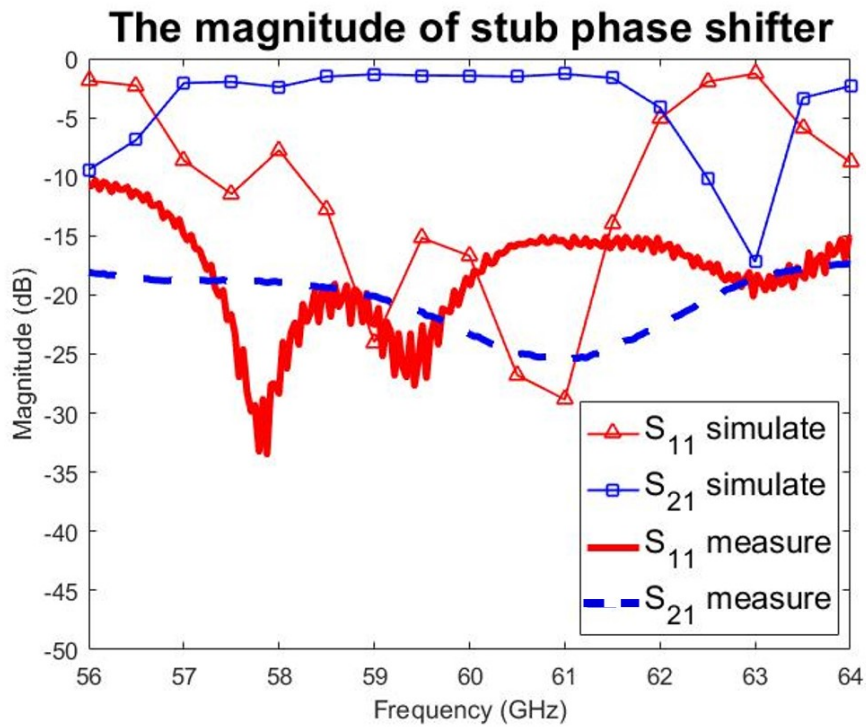


Fig. 4.14 The measured and simulated results of the 0-deg tuning phase shifter without

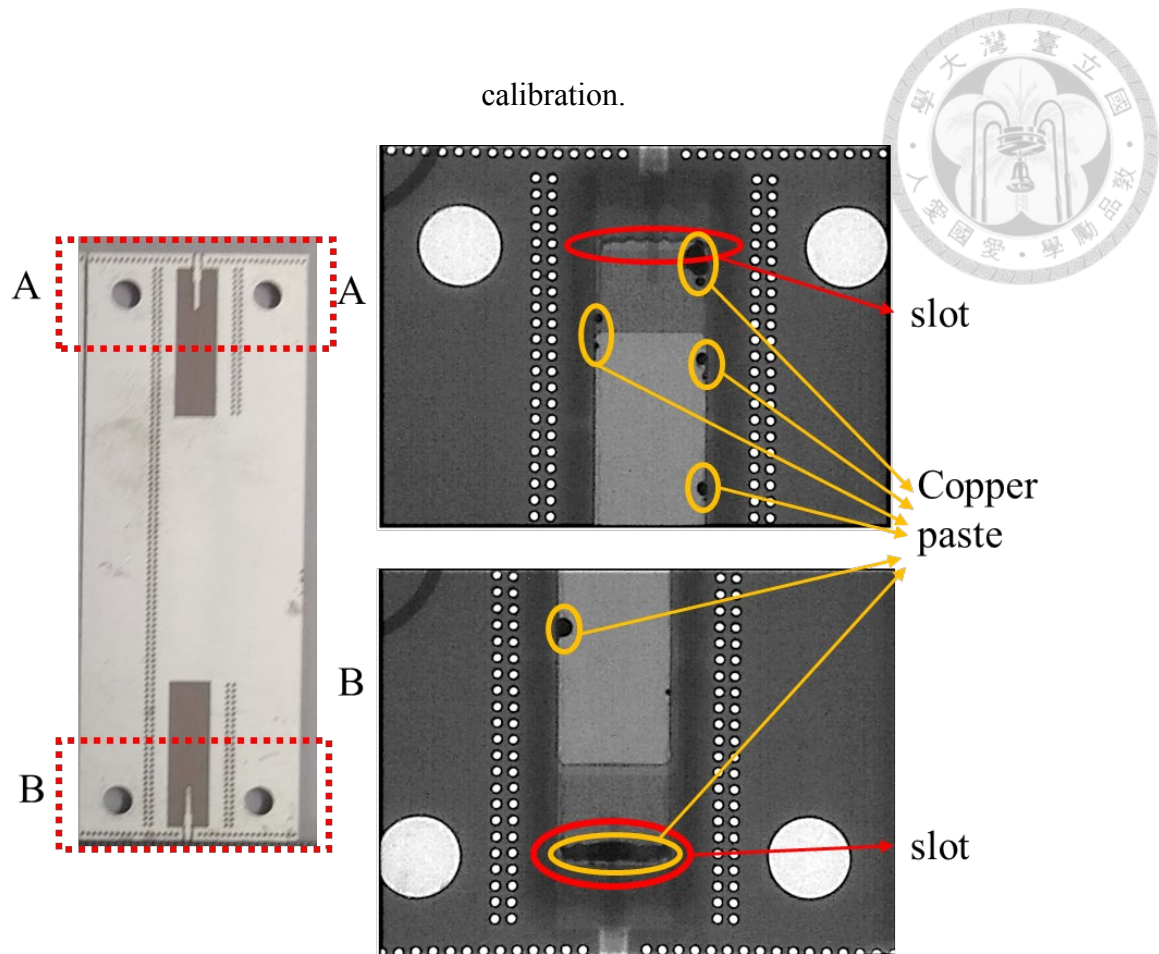
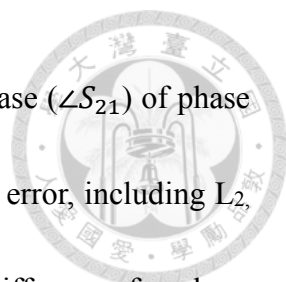


Fig. 4.15 The X-ray photo of phase shifter.

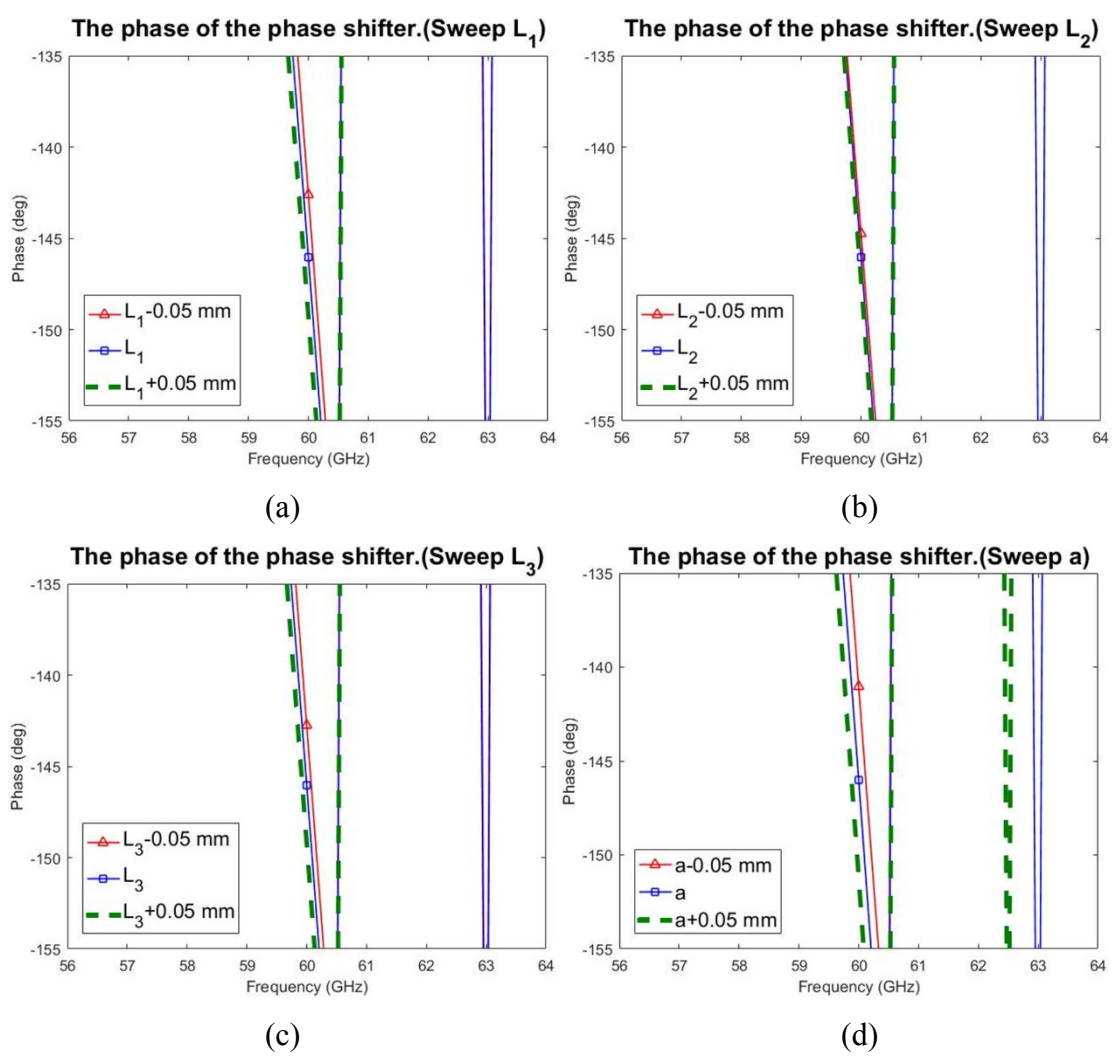
4.5 Sensitivity About Fabrication

Because the dimension error from fabrication will make the performance worse, we will discuss each parameter about stub phase shifter. We choose 0-deg tuning phase shifter to discuss as follows. As shown in Fig. 4.11, there are 6 parameters (a , a_1 , a_2 , L_1 , L_2 , L_3). We took the values of Table 4.2 and swept $\pm 0.5\text{mm}$ on simulation as the fabrication error.

For the magnitudes of the S-parameter, there are not large difference when parameters are changed. However, phase of the phase shifter is important factor which affects the phase difference of Butler matrix. Thus, we just focus on the phase of the phase



shifter at 60 GHz. As shown in Fig. 4.16, when $L_1 \pm 0.05\text{mm}$, the phase ($\angle S_{21}$) of phase shifter will differ in $\pm 3^\circ$. And the other parameters with $\pm 0.05\text{mm}$ error, including L_2 , L_3 , a , a_1 , and a_2 , will lead to $\pm 1^\circ$, $\pm 3^\circ$, $\pm 5^\circ$, $\pm 17^\circ$, and $\pm 4^\circ$ difference for phase ($\angle S_{21}$). From the above all, we can find that the phase is very sensitive to a_1 .



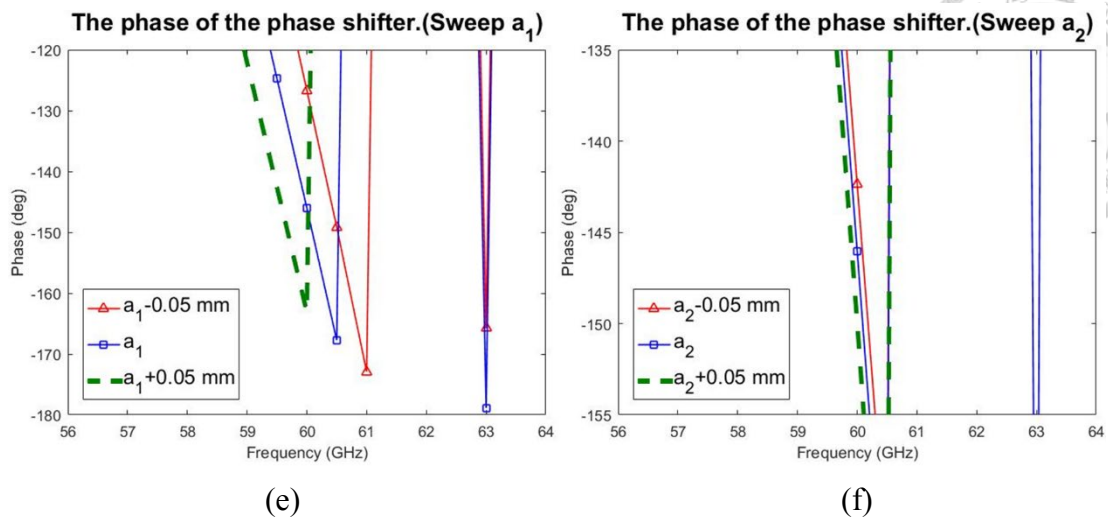


Fig. 4.16 Sweep the parameters $\pm 0.05\text{mm}$ in phase shifter.

(a)L₁ (b)L₂ (c)L₃ (d)a (e)a₁ (f)a₂



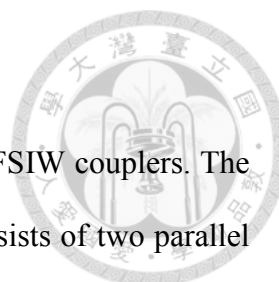


Chapter 5

AFSIW 4x4 Butler Matrix Antenna Array

A beamforming antenna array is composed by crossovers, couplers, phase shifters and the antenna array. Among them, we have successfully designed the phase shifter in Chapter 4. In this chapter, we are going to discuss the design of coupler and crossover based on AFSIW configuration, respectively. And then, the Butler matrix will be combined by couplers, crossovers and phase shifters. The comparison of the phase between each output port will be given.

After the Butler matrix design, slot antenna array in AFSIW configurations has been designed and connected to the Butler matrix. The simulation results for the overall beamforming antenna array will be shown. Also, the measured results will be included in this chapter. Lastly, a comparison between the proposed Butler matrix and the previous work will be given.



5.1 Coupler Design

In this thesis, we use the configuration in [19] to design the AFSIW couplers. The configuration is called short-slot coupler. The short-slot coupler consists of two parallel waveguides with the common wall removed in the center, which forms a slot region of size with $w \times l$. It's shown in Fig. 5.1. By adjusting the dimension of the slot region, the TE_{10} and TE_{20} modes can be generated. And by theory, the short-slot coupler can achieve any power ratio. The design equations are derived by the even-odd mode as following.

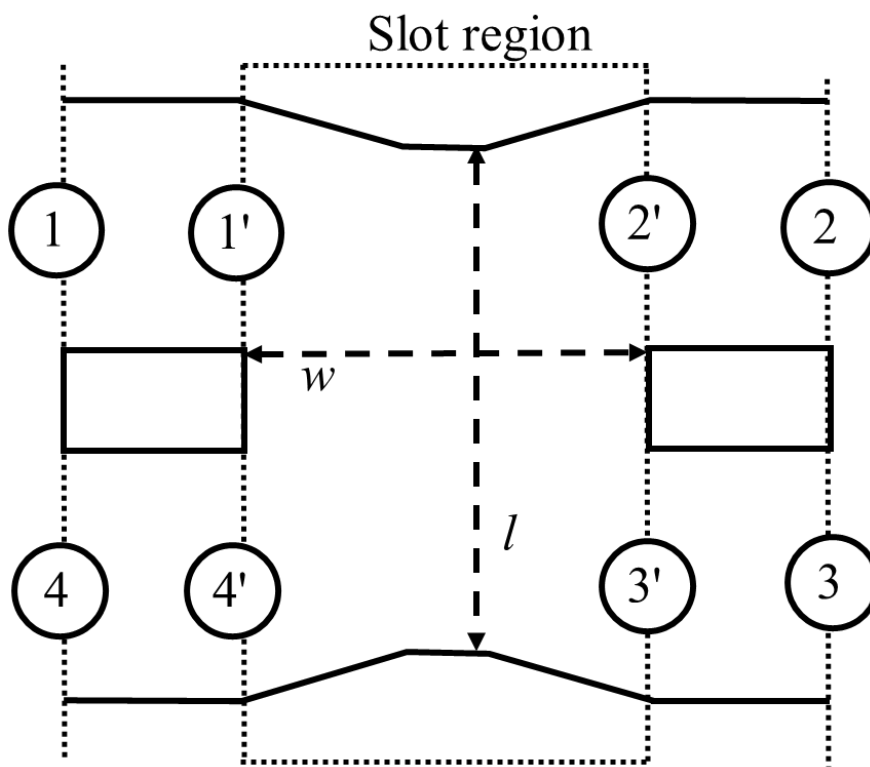


Fig. 5.1 The configuration of the coupler (Top view)

The incident waves of the port 1 – 4 are respectively equal to $\bar{a} = [a_1, 0, 0, 0]$. The even mode incident waves of the port 1 – 4 are respectively equal to $\bar{a}_e = [a_1/2, 0, 0, a_1/2]$. The odd mode incident waves of the port 1 – 4 are respectively equal to $\bar{a}_o = [a_1/2, 0, 0, -a_1/2]$. The relationship of the incident wave is that $\bar{a} = \bar{a}_e + \bar{a}_o$.

To easily discuss the slot region of the coupler, the port 1' – 4' represent the port on the slot region, which is shown in Fig. 5.1. It's obvious that between port 1 and port 1', there is a phase shift of the incident wave. And the same situations occur between port 2 – 4 and port 2' – 4', respectively. Here we represent the wave at port 1' – 4' as $\bar{a}', \bar{a}'_e, \bar{a}'_o, \bar{b}', \bar{b}'_e, \bar{b}'_o$, which are different from $\bar{a}, \bar{a}_e, \bar{a}_o, \bar{b}, \bar{b}_e, \bar{b}_o$ at port 1 – 4 with phase shifts. And $\bar{b}, \bar{b}_e, \bar{b}_o, \bar{b}', \bar{b}'_e, \bar{b}'_o$ are the reflected wave here.

For the even mode, the TE₁₀ mode is induced to propagate in the slot region. And for the odd mode, the TE₂₀ mode is induced to propagate in the slot region. So, the reflected wave of the port 1' – 4' for the even mode is $\bar{b}'_e = (a'_1/2) \times [0, e^{-j\beta_{10}l}, e^{-j\beta_{10}l}, 0]$. The reflected wave of the port 1' – 4' for the odd mode is $\bar{b}'_o = (a'_1/2) \times [0, e^{-j\beta_{20}l}, -e^{-j\beta_{20}l}, 0]$. The relationship of the reflected wave is $\bar{b}' = \bar{b}'_e + \bar{b}'_o$. The reflected wave of the port 1' – 4' is $\bar{b}' = (a'_1/2) \times [0, e^{-j\beta_{10}l} + e^{-j\beta_{20}l}, e^{-j\beta_{10}l} - e^{-j\beta_{20}l}, 0]$. Then, the S-parameter of the slot region is obtained as follows:

$$\begin{aligned}
 S_{1'1'} &= 0, \\
 S_{2'1'} &= (1/2) \times (e^{-j\beta_{10}l} + e^{-j\beta_{20}l}) \\
 &= \cos[(\beta_{10} - \beta_{20})\frac{l}{2}] e^{-j(\beta_{10} + \beta_{20})\frac{l}{2}}, \\
 S_{3'1'} &= (1/2) \times (e^{-j\beta_{10}l} - e^{-j\beta_{20}l}) \\
 &= -j\sin[(\beta_{10} - \beta_{20})\frac{l}{2}] e^{-j(\beta_{10} + \beta_{20})\frac{l}{2}},
 \end{aligned} \tag{5.1}$$

$$S_{4'1'} = 0$$

where β_{10} and β_{20} are the phase constant of the TE₁₀ and TE₂₀ mode in the waveguide, respectively. By the equation (5.1), it can be derived that



$$\sin^{-1}|S_{3'1'}| = (\beta_{10} - \beta_{20}) \frac{l}{2} \quad (5.2).$$

There is an even mode junction discontinuity as shown in Fig. 5.2, which is the left side of Fig. 5.1. The reflected wave at port 1' and 4' are given that

$$b'_1 = b'_4 \approx \left(\frac{a'_1}{2}\right) \times [S_{AA} + (S_{BA} e^{-j\beta_{10}l})^2 S_{BB}] \quad (5.3).$$

It can be approximated [6] and simplified to

$$1 + e^{-j2\beta_{10}l} = 0 \quad (5.4).$$

Then, the length of the slot region can be derived by

$$l = \frac{(2n + 1)\pi}{2\beta_{10}} \quad (5.5),$$

where n is a positive integer.

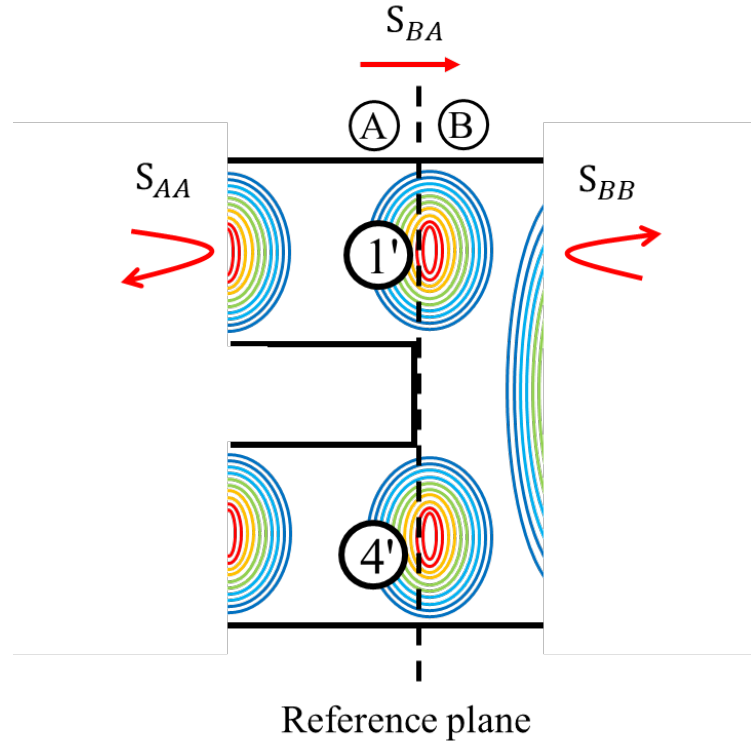
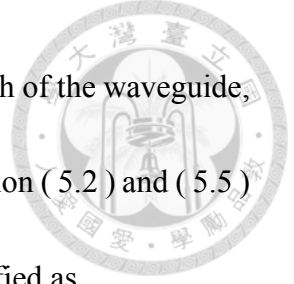


Fig. 5.2 The even mode junction discontinuity of the coupler (Top view)



From equation (2.13), the β_{10} and β_{20} are related to the width of the waveguide, so they are also related to the width of the slot region. Then, the equation (5.2) and (5.5) are related to the length and width of the slot region. It can be simplified as

$$w = \frac{\pi}{k} \sqrt{\frac{[\pi(2n + 1) + 4 \sin^{-1}|S_{3'1'}|] [3\pi(2n + 1) - 4 \sin^{-1}|S_{3'1'}|]}{8 \sin^{-1}|S_{3'1'}| [\pi(2n + 1) - 2 \sin^{-1}|S_{3'1'}|]}} \quad (5.6),$$

where k is the wavenumber. From equation (5.5) and (5.6), we can obtain the dimension of the slot region to design the coupler.

The target coupler for our proposed Butler matrix is a 3-dB coupler with 90-degree phase difference between couple port and through port. So, assigning the $|S_{3'1'}| = 1/\sqrt{2}$ into the equation (5.5) and (5.6) we can obtain the length and width equations of the slot region.

$$w = \frac{\pi}{k} \sqrt{\frac{4(3n + 1)(n + 1)}{4n + 1}} \quad (5.7)$$

$$l = \frac{\pi}{k} \sqrt{\frac{(3n + 1)(n + 1)}{3}} \quad (5.8)$$

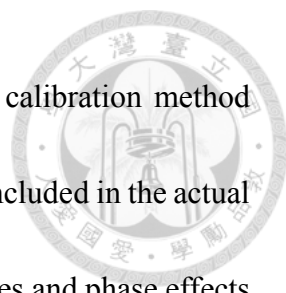
When $n = 1 - 4$, w and l is obtained from the equation (5.7) and (5.8). The parameters are summarized in Table 5.1.

<i>n</i>	1	2	3	4
<i>w</i> (mm)	6.32	7.64	8.77	9.78
<i>l</i> (mm)	4.08	6.61	9.13	11.64

Table 5.1 Width and length of the slot region of the coupler.

When choosing the width, it is necessary to pay attention to whether the TE₃₀ mode will be generated in the AFSIW structure at 60 GHz. So, the dimensions of $n = 1$ are chosen as the initial value of the simulation on HFSS software. Then, the width and length of the slot region are optimized on HFSS software so that the phase difference between couple port and through port is close to 90-degree and the magnitude difference between couple port and through port is close to 0-dB.

The final geometrical dimensions of the proposed coupler are shown in Fig. 5.3. And the photograph of the coupler is shown in Fig. 5.4. The simulation results on the HFSS software and measurement results are shown in Fig. 5.5. The S_{21} and S_{31} of the simulated coupler respectively are -3.13 dB and -3.14 dB at 60 GHz. The bandwidth (defined by S_{11} lower than -15 dB) of the simulated coupler is between 57.8 to 80 GHz. The bandwidth is very wide. The S_{41} of the simulated coupler is below -15 dB from 57.7 GHz to 80 GHz. The phase difference between S_{21} and S_{31} is $90^\circ \pm 5^\circ$ between 56.2 to 65.6 GHz on simulation.



The measurements are calibrated by Thru-Reflect-Line (TRL) calibration method [26] due to the calibrating part (Fig. 5.4 AA'-BB' and CC'-DD') are included in the actual measurements. TRL calibration is a method removing the excess losses and phase effects to obtain the accurate S-parameter of the object to be measured. The error box of TRL is the calibrating part which includes the end launch, curved microstrip line, the feeding of AFSIW and a small segment AFSIW. The measurement results of device under test (DUT) (Fig. 5.4 BB'-CC') are shown in Fig. 5.5.

From 60.5 GHz to 61.5 GHz, the measured maximum difference between S_{21} and S_{31} is 1 dB. The phase difference between S_{21} and S_{31} is $90^\circ \pm 5^\circ$ between 59.4 to 62.4 GHz on measurement. The reason why the measurement results are not match to simulation will be discussed in Section 5.5.

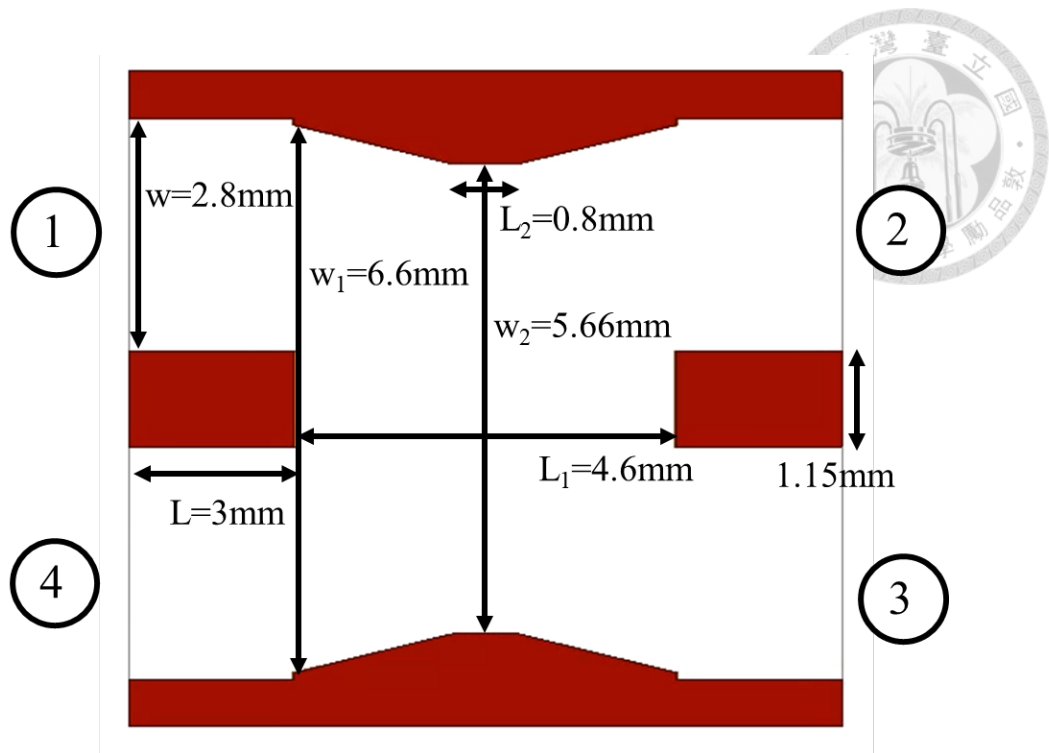


Fig. 5.3 The geometrical dimensions of the proposed coupler. (Top view)

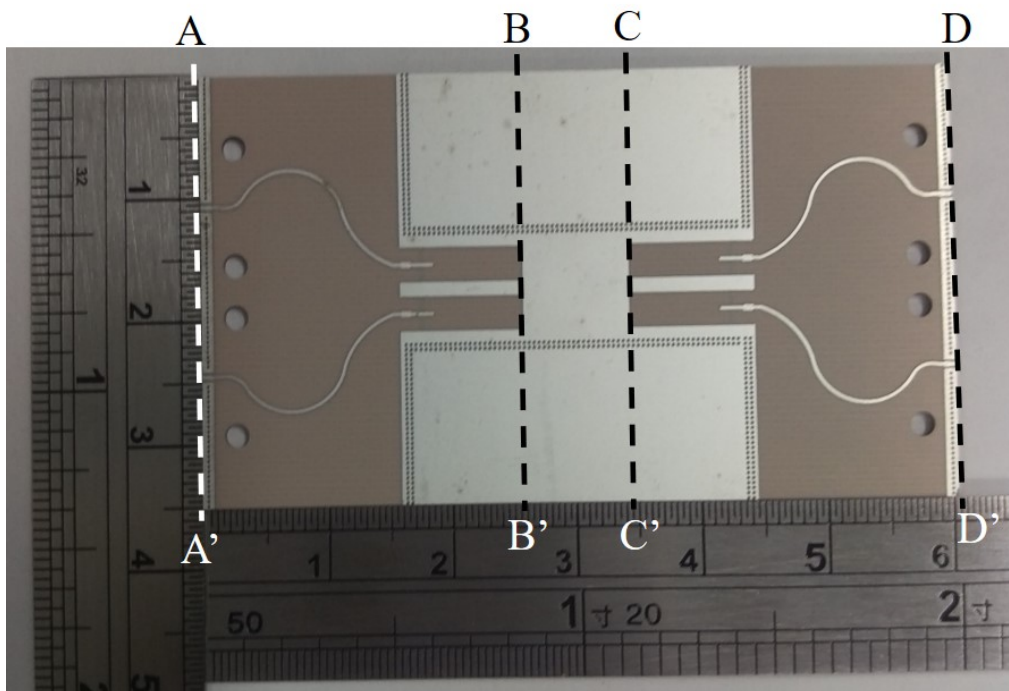
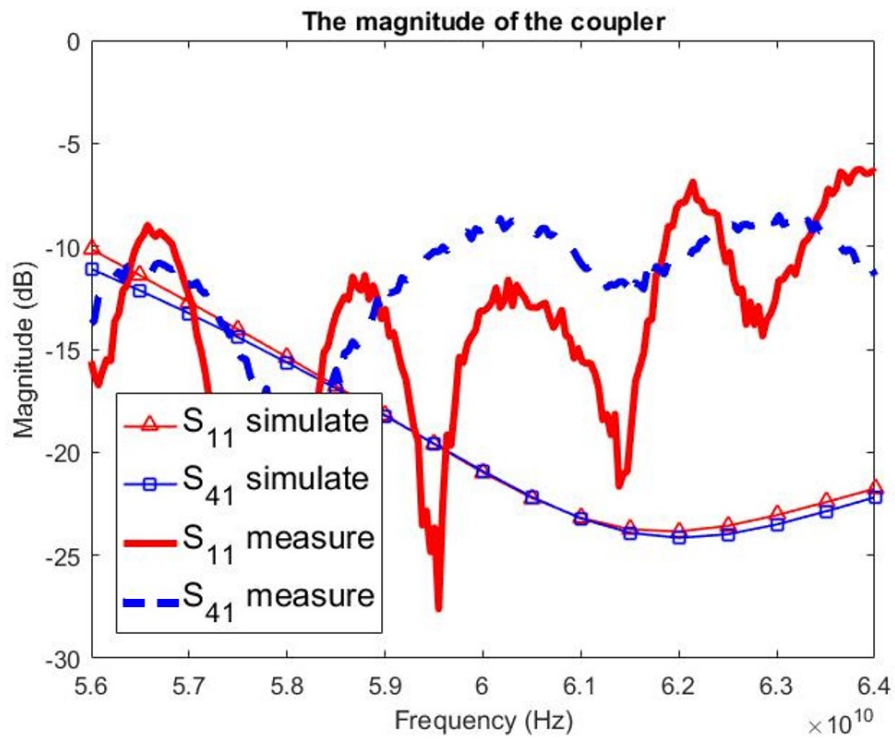
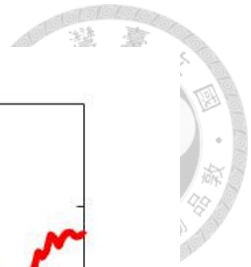
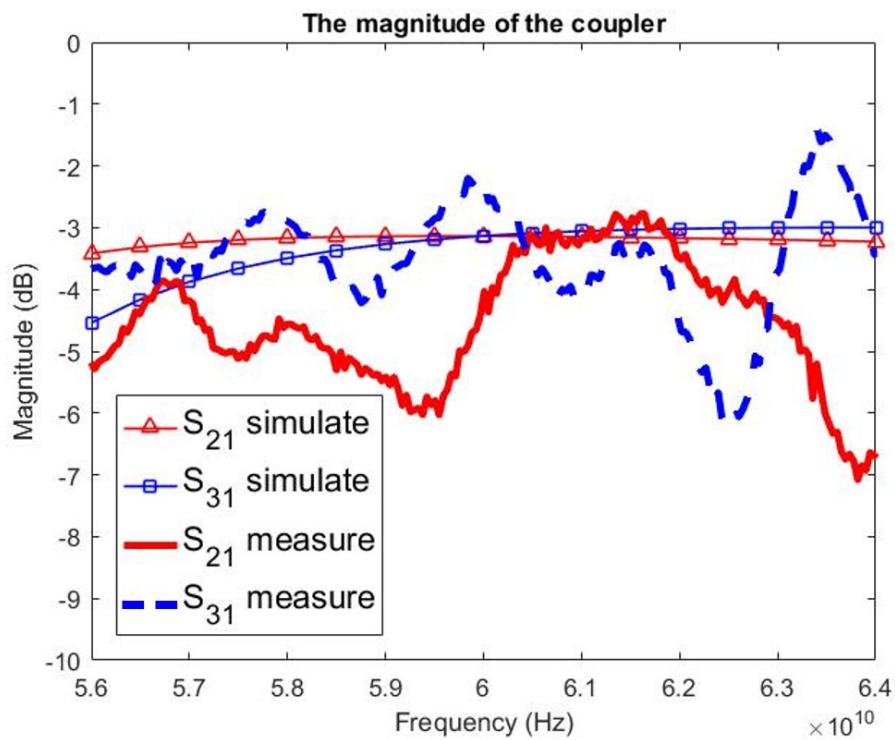


Fig. 5.4 The photograph of the coupler.



(a)



(b)

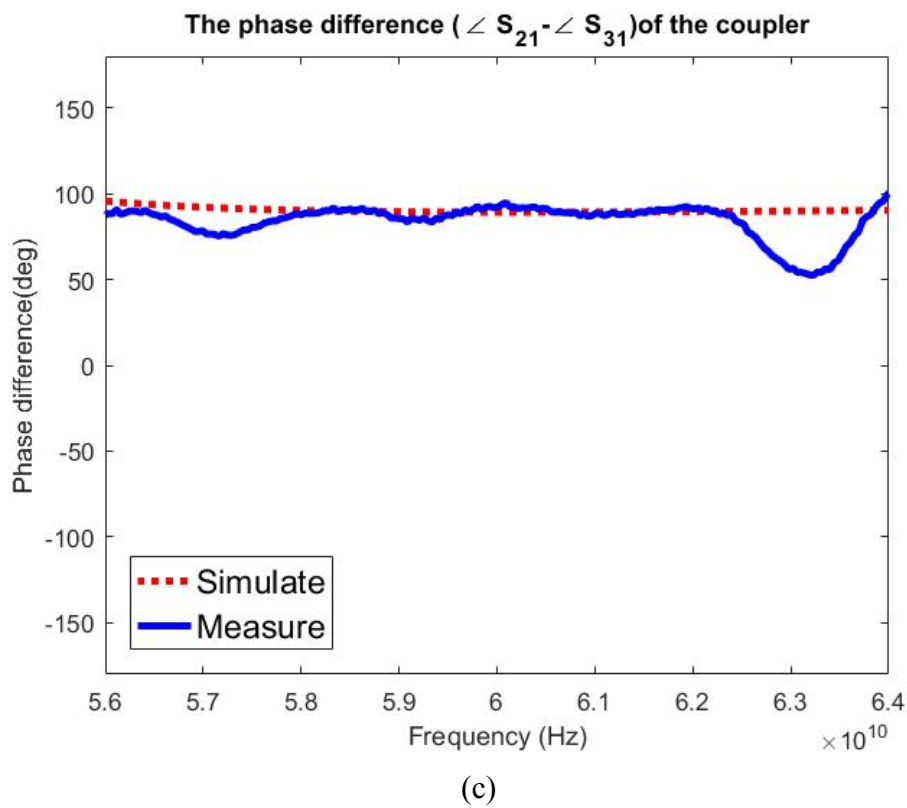


Fig. 5.5 The simulation results and measurement results of the proposed coupler. (a) S_{11} and S_{31} (b) S_{21} and S_{31} (c) Phase difference

5.2 Crossover Design

The design method of the crossover is the same as the coupler. So we can also use the equation (5.5) and (5.6) to obtain the dimensions of the slot region to design the crossover. The proposed crossover is the 0-dB coupler. Assigning the $|S_{3'1'}| = 1$ into the equation (5.5) and (5.6) we can obtain the length and width equation of the slot region.

$$w = \frac{\pi}{k} \sqrt{\frac{(6n + 1)(2n + 3)}{8n}} \quad (5.9)$$



$$l = \frac{\pi}{k} \sqrt{\frac{(6n + 1)(2n + 3)}{12}} \quad (5.10)$$

When $n = 1 - 4$, w and l is obtained from the equation (5.9) and (5.10). It's summarized in Table 5.2.

n	1	2	3	4
w (mm)	5.23	5.96	6.67	7.33
l (mm)	4.27	6.88	9.44	11.97

Table 5.2 Width and length of the slot region of the crossover.

The dimensions of $n = 3$ are chosen as the initial value of the simulation and optimize on HFSS software so that the magnitude of S_{31} is close to 0-dB. Due to the phase shifter is designed on Chapter 4, there are three important restrictions that we have to pay attention to. The first restriction is that the total physical length of the crossover should be the same as the total physical length of the phase shifter. This restriction is to simplify the complexity of the Butler matrix circuit and reduce the overall circuit size. The second one is that the phase of S_{31} of the crossover should be different from the phase of the phase shifter by 0 degrees or 45 degrees. The last one is that when choosing the width, it is necessary to avoid the generation of TE_{30} mode.

The final geometrical dimensions of the proposed crossover are shown in Fig. 5.6. And the photograph of the crossover is shown in Fig. 5.7. The simulation results on the HFSS software and measurement results are shown in Fig. 5.8. The S_{31} of the simulated crossover is -0.15 dB at 60 GHz. The bandwidth (defined by S_{11} lower than -15 dB) of



the crossover is between 58.7 to 61.6 GHz on simulation. The phase of S_{31} of the simulated crossover is -146.6° at 60 GHz.

The measurements are calibrated by TRL calibration due to the calibrating part (Fig. 5.7 AA'-BB' and CC'-DD') are included in the actual measurements. The error box of TRL is the calibrating part which includes the end launch, curved microstrip line, the feeding of AFSIW and a small segment AFSIW. The measurement results of the DUT (Fig. 5.7 BB'-CC') are shown in Fig. 5.8.

The S_{31} of the measured crossover is -2 dB at 60 GHz. The phase of S_{31} of the measured crossover is -163.1° at 60 GHz. The frequency deviation phenomenon can be found from the phase comparison. The reason why the measurement results are not match to simulation will be discussed in Section 5.5.

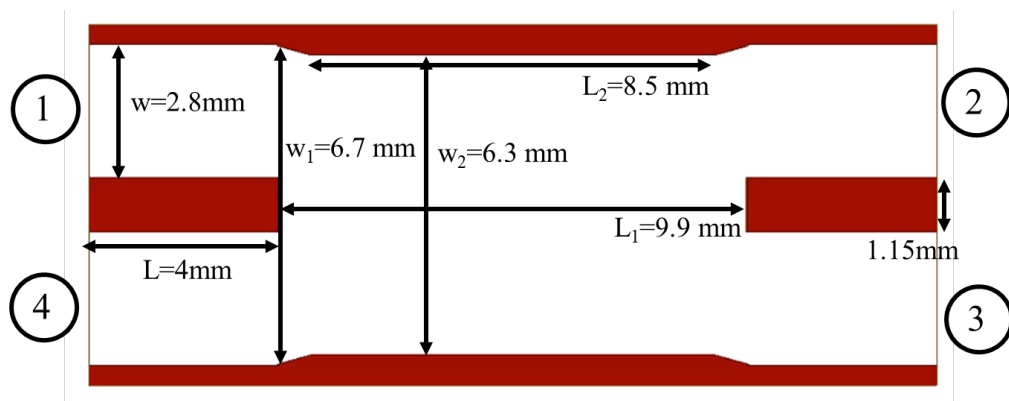


Fig. 5.6 The geometrical dimensions of the proposed crossover. (Top view)

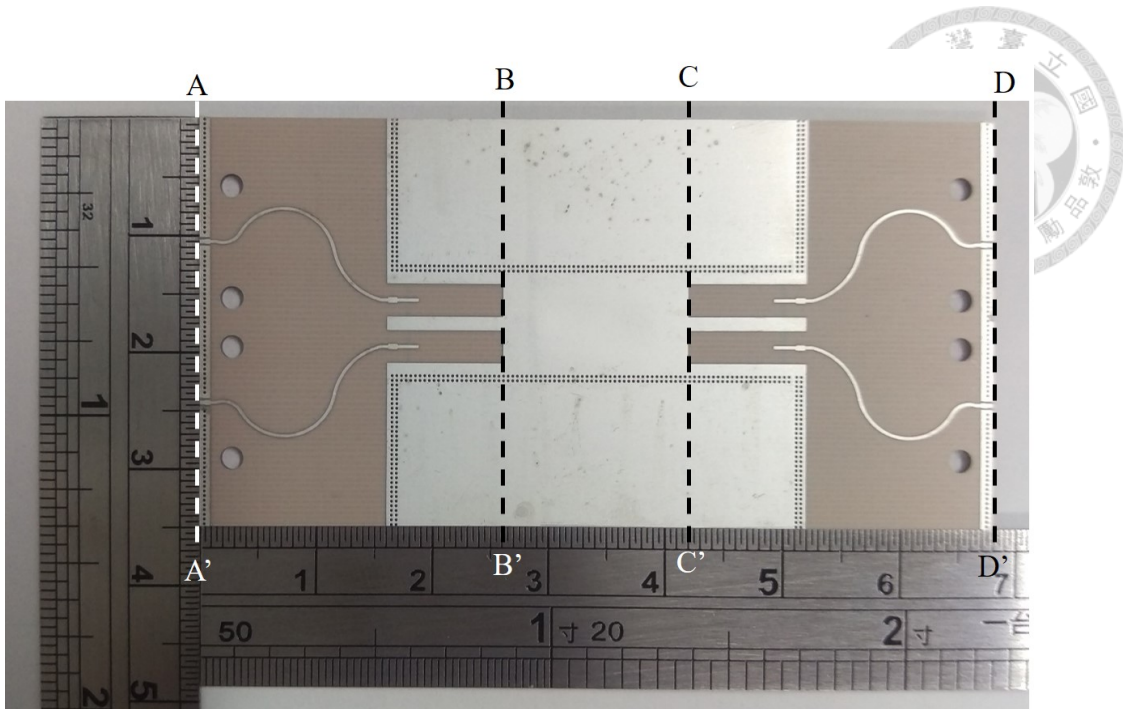
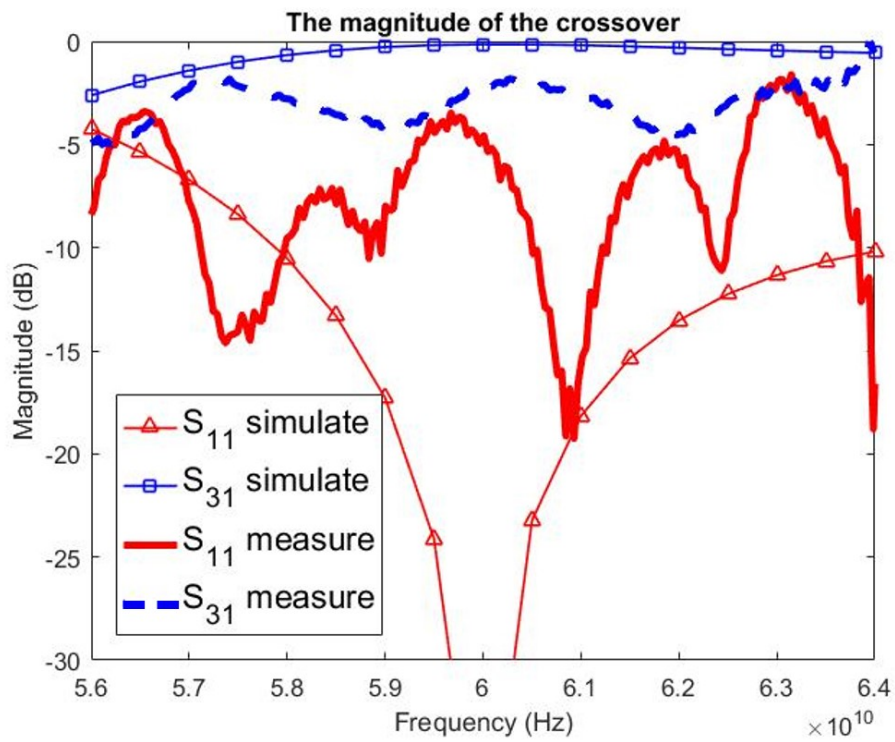


Fig. 5.7 The photograph of the crossover.



(a)

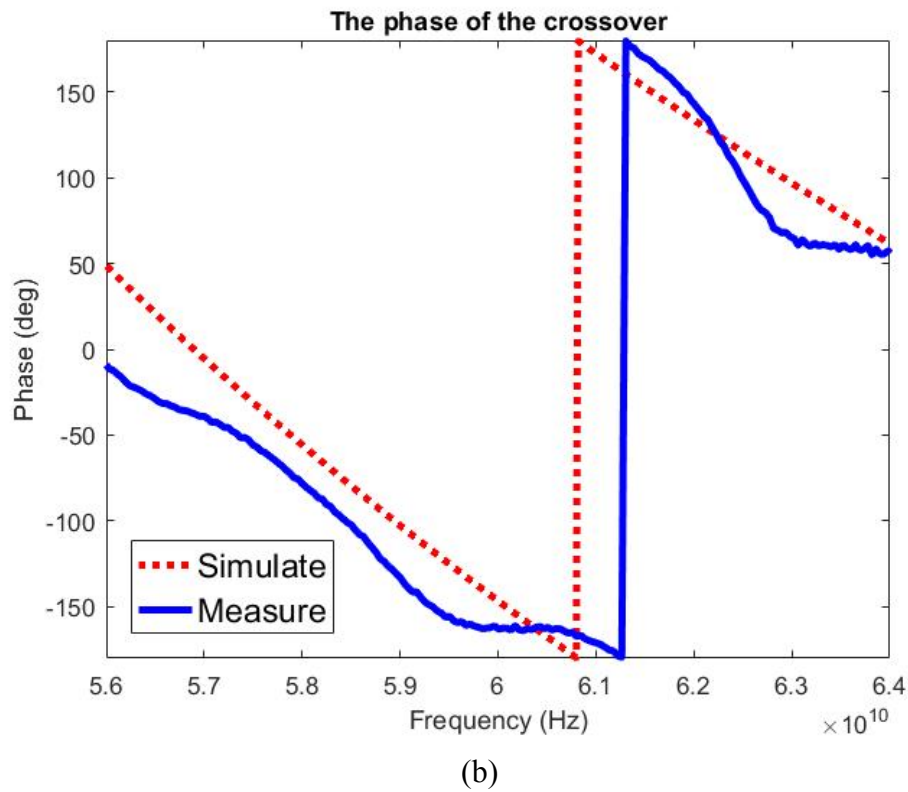
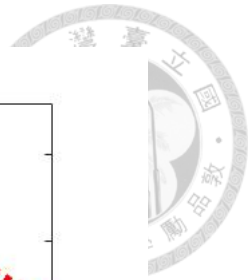


Fig. 5.8 The simulation results and measurement results of the proposed crossover. (a)

magnitude (b) phase

5.3 Slot Antenna Array Design

5.3.1 Slot Antenna Design

The transverse wave currents on the short-circuited waveguide is shown in Fig. 5.9 [35]. The design rules of slot antenna in waveguide are shown as follows.

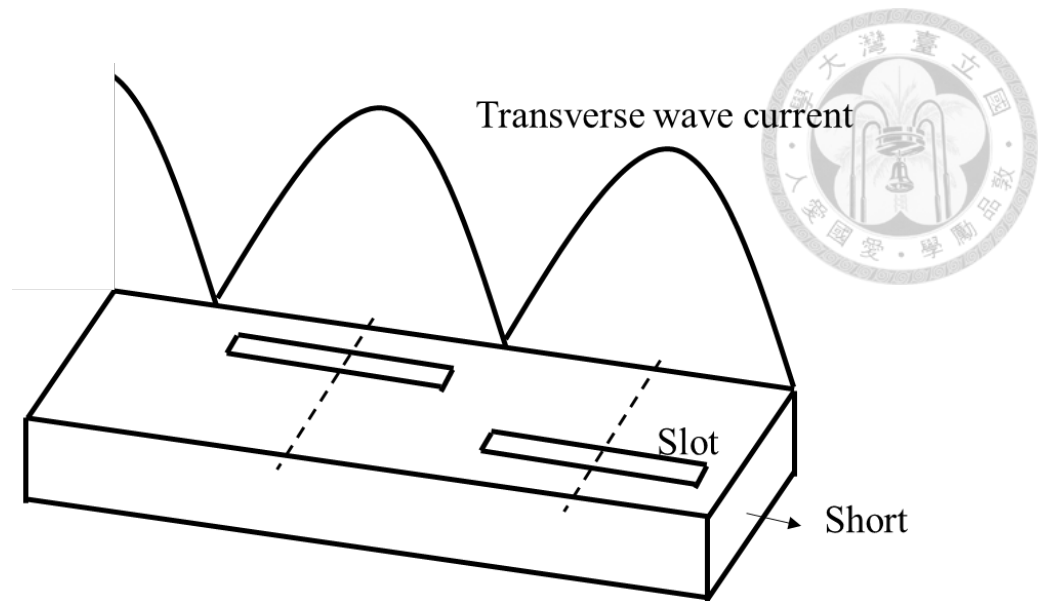


Fig. 5.9 The transverse wave currents on the short-circuited waveguide

First, the end of the waveguide is a short end. The short end is realized by the via wall. Second, the distance of the first slot (closest to the short-end) to the short-end is $\lambda_g/4$. It can be regarded as open circuit at the slot center of the first slot for impedance matching. The length of the slots is $\lambda/2$. Finally, each slot should be separated by $\lambda_g/2$.

Also, each slot should be offset from the right or left side of the centerline. The reason of this design rule can be observed from Fig. 5.10 and Fig. 5.11. The peaks of two adjacent transverse wave current with $\lambda_g/2$ spacing are shown in Fig. 5.10. We can find that the currents are 180° out of phase on the two sides of the centerline, which means there is a negative sign between the peak of two adjacent transverse wave current. So, the slot is separated $\lambda_g/2$ and be placed on the other side of the centerline to compensate for out of phase from the peaks of two adjacent transverse wave current. The structure of the slot antenna is shown in Fig. 5.11.

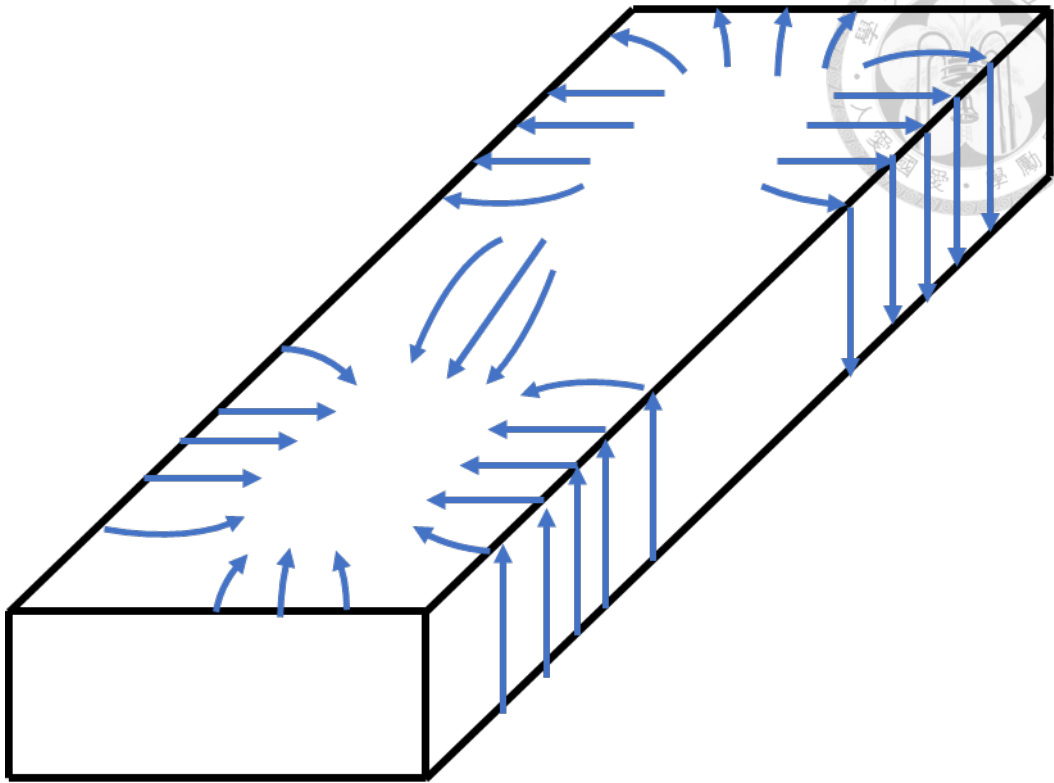


Fig. 5.10 TE₁₀ mode waveguide transverse wave currents.

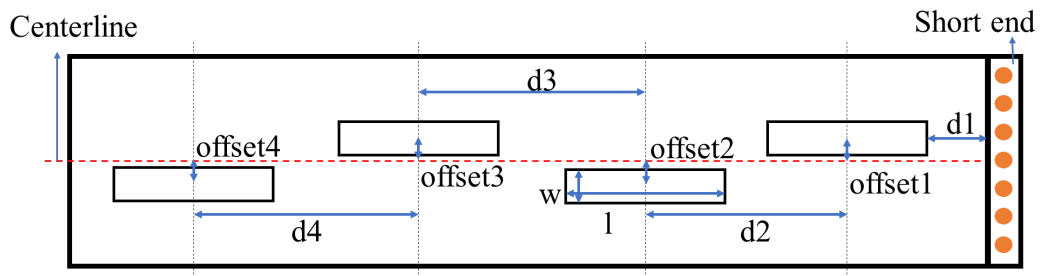


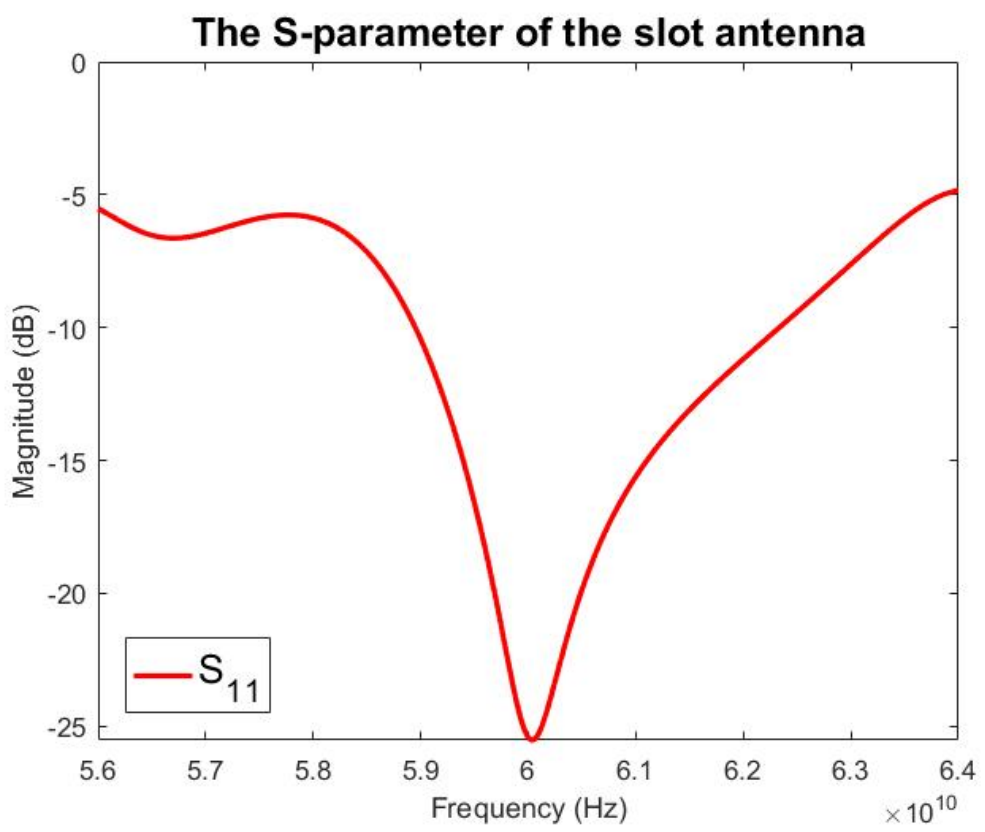
Fig. 5.11 Structure of the slot antenna

The geometry of the slot antenna is summarized on Table 5.3. And the simulation results of the slot antenna are shown in Fig. 5.12. The bandwidth (defined by S_{11} lower than -10 dB) of the slot antenna is between 58.9 GHz and 62.3 GHz. The gain of the slot antenna is 14.7 dB.



d1	d2	d3	d4	w
<i>2.5 mm</i>	5 mm	5 mm	5 mm	0.2 mm
offset1	offset2	offset3	offset4	l
<i>0.2 mm</i>	0.15 mm	0.15 mm	0.15 mm	2.3 mm

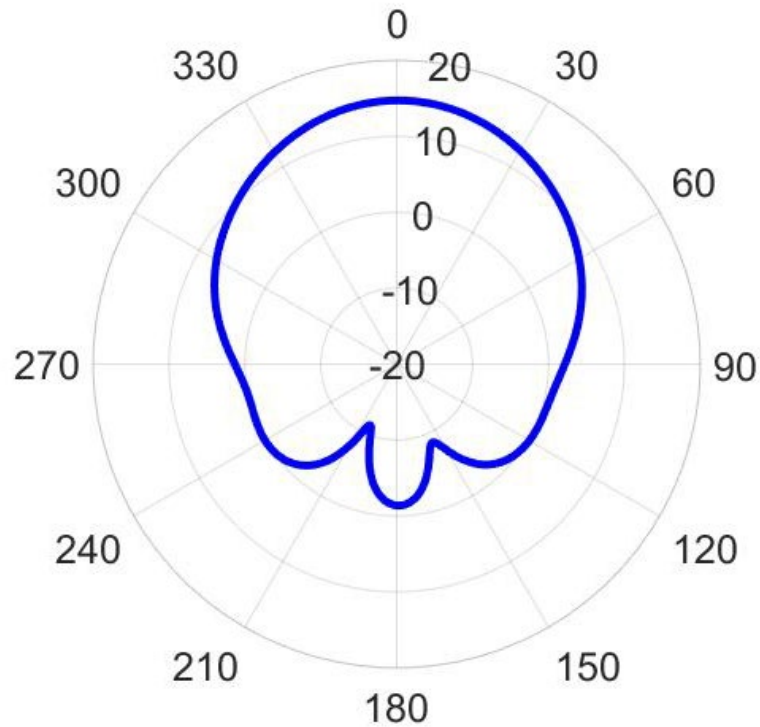
Table 5.3 Geometry of the slot antenna



(a)



Radiation pattern of the slot antenna



(b)

Fig. 5.12 The simulation results of the slot antenna. (a) S-parameter (b) Radiation pattern ($\phi = 0$)

5.3.2 Slot Antenna Array

The proposed slot antenna is used and be separated by same distance to implement the slot antenna array for broadside radiation. There are two issues affecting the radiation pattern of the antenna array. The first issue is the spacing between each antenna element, which is the key parameter for array factor. The second issue is the mutual coupling between each antenna element.

In general, in order to achieve proper main beam directivity, reduce sidelobe level and avoid grating lobe generation, the distance of the antenna elements (or called inter-element distance) in antenna array is designed with half wavelength spacing. However,

the width of AFSIW structure is designed as 0.5λ to handle the fundamental mode in the center hollow part. Considering fabrication limit and manufacturing problems, some space needs to be reserved between the antenna array. So, the spacing of the antenna array must be larger than 0.5λ .

In order to observe the effect of the inter-element distance on the radiation pattern, we choose two cases to compare the radiation pattern. One is the case with half wavelength spacing. The other one is a larger spacing that can be made after considering the fabrication limit.

The radiation patterns with different inter-element distances are obtained by using the radiation pattern of the proposing slot antenna and the array factor derived from Section 2.3. The radiation patterns of the beamforming antenna array with 4 elements are shown in Fig. 5.13. These four figures show the radiation patterns with four different phase differences provided by the Butler matrix, respectively. As shown Fig. 5.13, when d (inter-element distance) is larger than 0.5λ , the sidelobe becomes large and the grating lobe exists. The angle between the direction angle of main beam and 0 degrees becomes small.

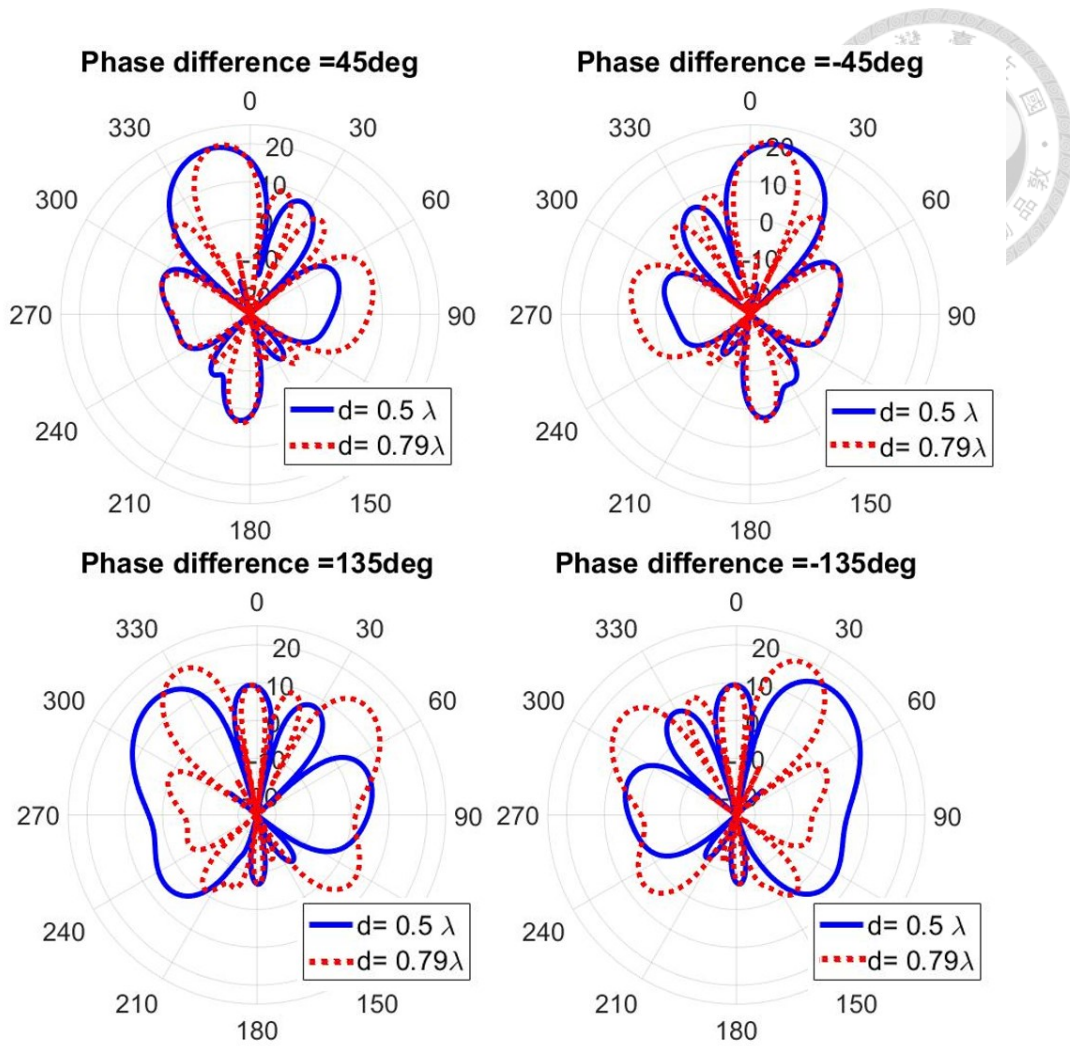


Fig. 5.13 The radiation pattern of the antenna array calculated by MATLAB with different inter-element distances.

In order to improve the second issue, from [36], many methods are mentioned for reducing the mutual coupling of each antenna. Such as decoupling network, frequency-selective surface (FSS), electromagnetic bandgap (EBG) or making a drilling slot between the antennas. Thus, in this thesis, we choose making a drilling slot between the antennas to reduce the mutual coupling, as shown in Fig. 5.14. There are drilling slots in the antenna array from M1 to PP2.

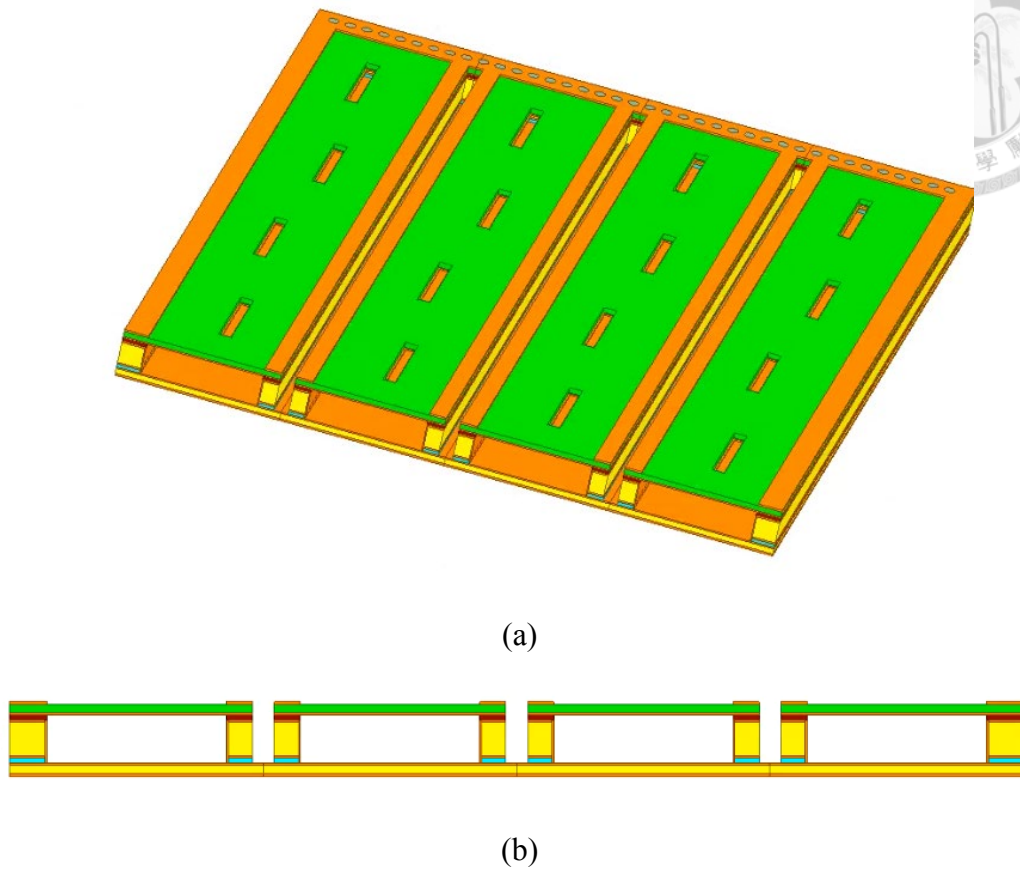


Fig. 5.14 The structure of the antenna array with isolation (a) 3D view (b) front view

To observe the effect of the mutual coupling on the radiation pattern, some cases are compared by following methods:

Considering the proposed slot antenna array in this thesis, the distance of each antenna element is 0.79λ and the number of antenna element is 4 ($N = 4$). The radiation pattern of the single antenna simulated on HFSS is multiplied by array factor to calculate final radiation pattern by MATLAB. This case is the ideal case without non-ideal mutual coupling. The results are shown by case 1. The antenna array consisting of four proposed slot antennas and without drilling slot between antennas is simulated on HFSS. The simulated results are shown by case 2. Case 3 is an antenna array simulated on HFSS which is composed of four proposed slot antennas and drilling slots between antennas.

For case 4, compared to case 3, the drilling slot is changed to a row of through-hole via. The simulated results of these cases are shown in Fig. 5.15 and Fig. 5.16.

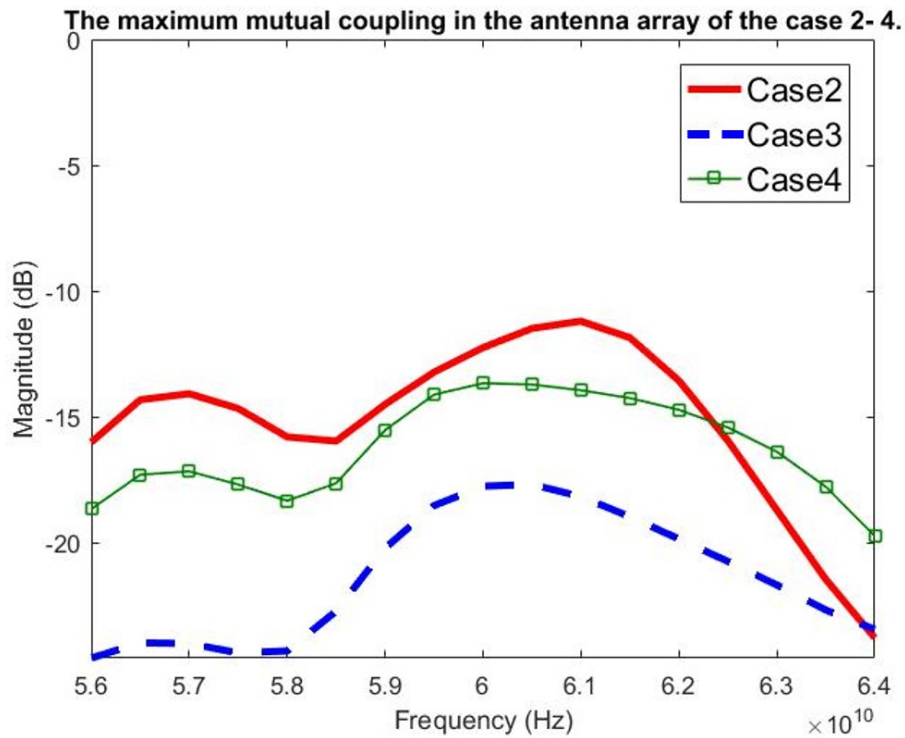
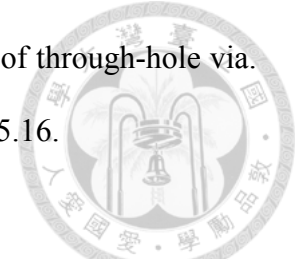


Fig. 5.15 The maximum mutual coupling in the antenna array of the case 2- 4.

From Fig. 5.15, since the case2 is without any isolation design, the magnitude of the mutual coupling is larger than case3 and case4. For case3, compared to case4, the magnitude of the mutual coupling is smaller than case4. Thus, it can be observed that making drilling slots between the antennas is the best method to reduce mutual coupling.

From Fig. 5.16, case 2 does not match case 1. When array factor is multiplied by the radiation pattern of single antenna simulated on HFSS, ideal isolation between each element is assumed. In comparison, the results of case2 are from complete full wave simulation, so the mutual coupling will be induced by each element. And also, the main beam of case 1 is larger than that of case 2. And the grating lobe of case 2 is larger than

case1. For case3, the main beam is larger compared to case 2. Because the mutual coupling is reduced by the drilling slot design, the main beam is increased. With the drilling slot design, the main beam level can be approximately similar to ideal case. From these data, we can summarize that mutual coupling affects the radiation pattern.

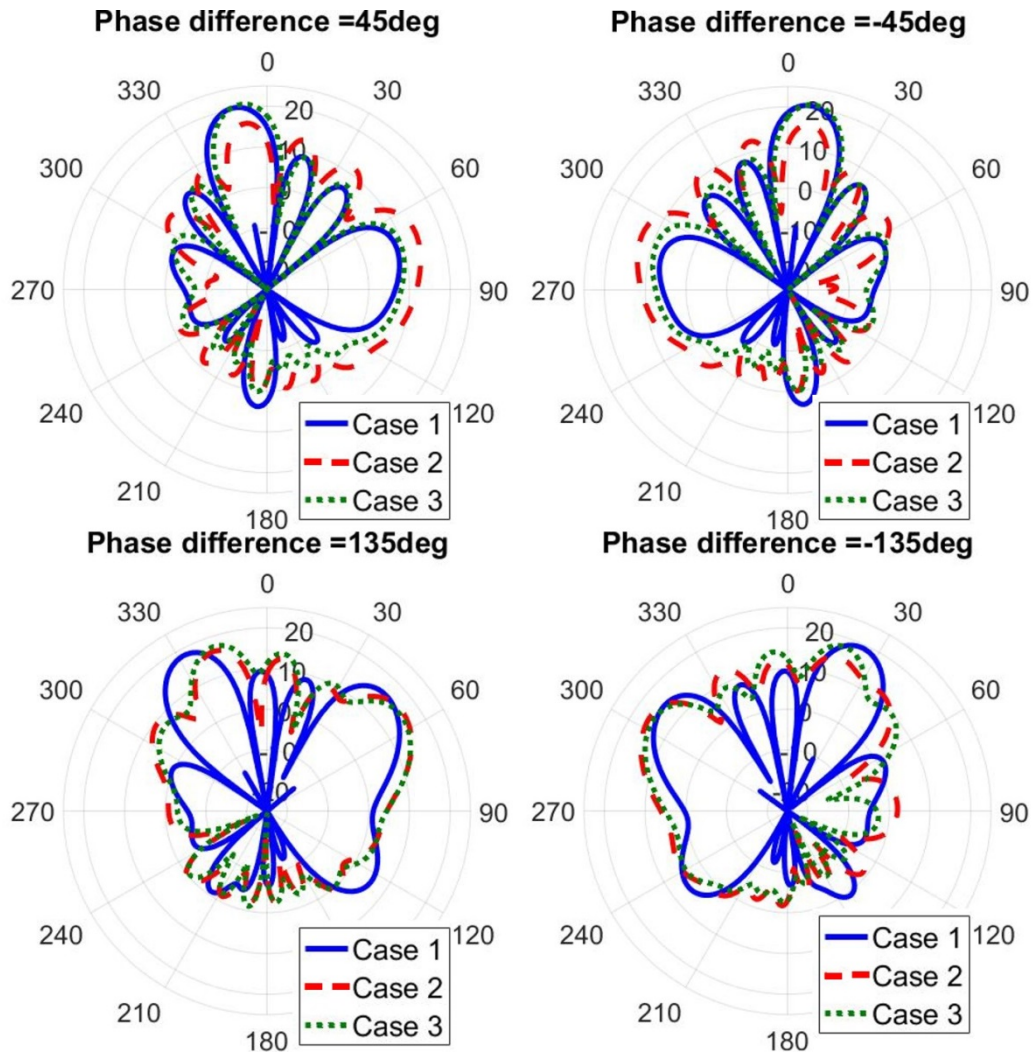
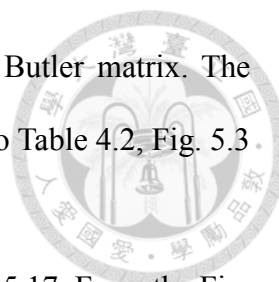


Fig. 5.16 Slot antenna array radiation pattern of case 1- 3.

5.4 AFSIW 4x4 Butler Matrix Antenna Array

5.4.1 Butler Matrix

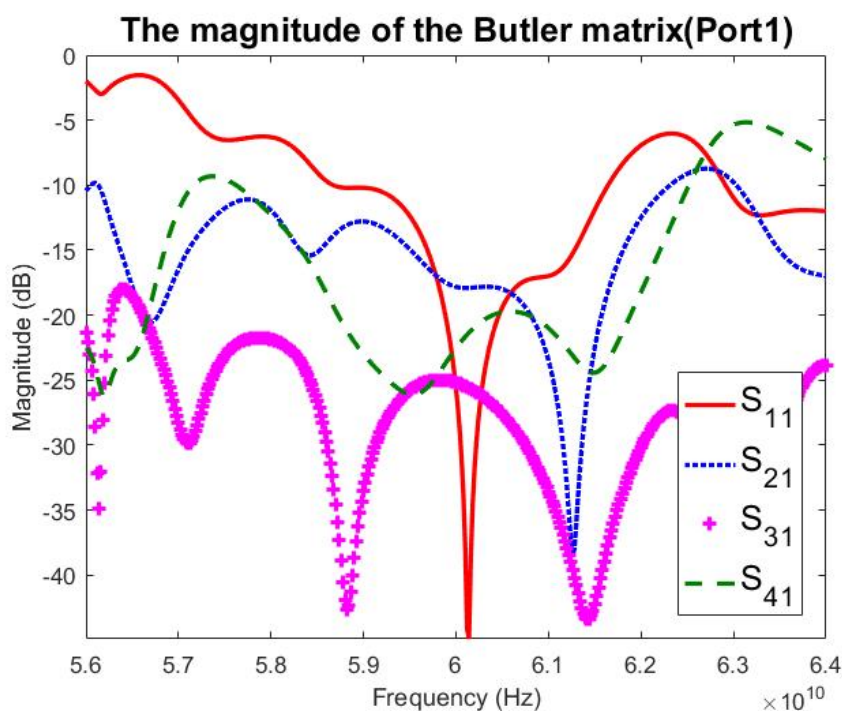
Butler matrix is composed of the previously designed coupler, crossover and phase shifter. Since the bandwidth of the tuning phase shifter is wider than the bandwidth of the



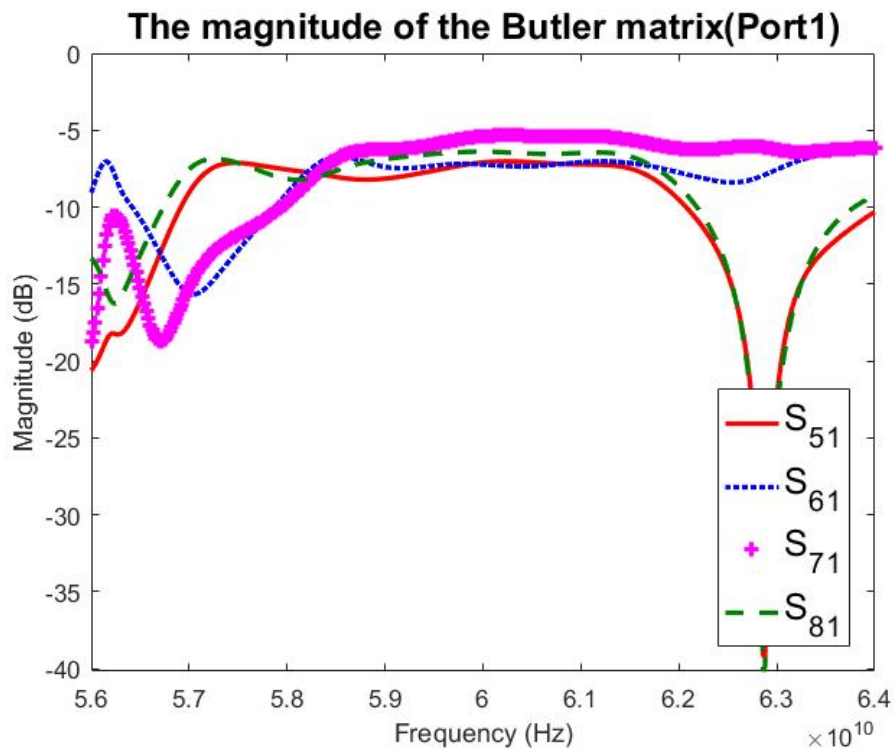
theoretic phase shifter. The tuning phase shifter is chosen for the Butler matrix. The dimension of the phase shifter, coupler and crossover are according to Table 4.2, Fig. 5.3 and Fig. 5.6, respectively.

The S-parameter of the proposed Butler matrix is shown in Fig. 5.17. From the Fig. 5.17(a) and (b), when input port is port 1, the simulated S_{11} , S_{21} , S_{31} , and S_{41} are all smaller than -15 dB from 59.7 GHz to 61.3 GHz. The simulated S_{51} , S_{61} , S_{71} , and S_{81} are kept within -6.3 ± 1 dB from 59.7 GHz to 61.3 GHz.

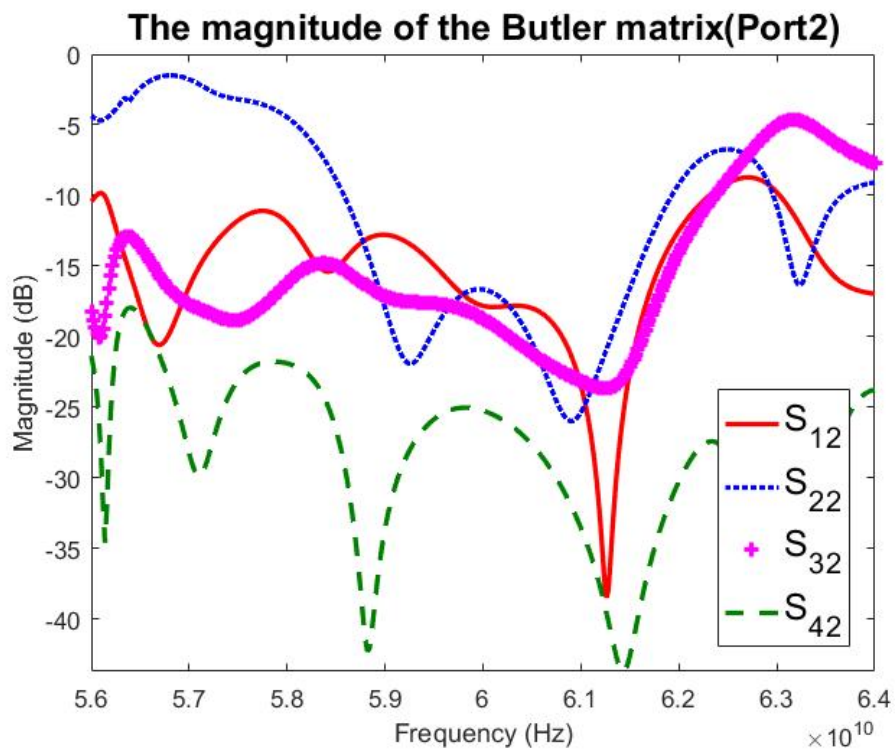
From Fig. 5.17(c) and (d), when input port is port 2, the simulated S_{12} , S_{22} , S_{32} , and S_{42} are all smaller than -15 dB from 59.5 GHz to 61.6 GHz. The simulated S_{52} , S_{62} , S_{72} , and S_{82} are kept within -6.8 ± 1.1 dB from 59.5 GHz to 61.6 GHz.



(a)



(b)



(c)

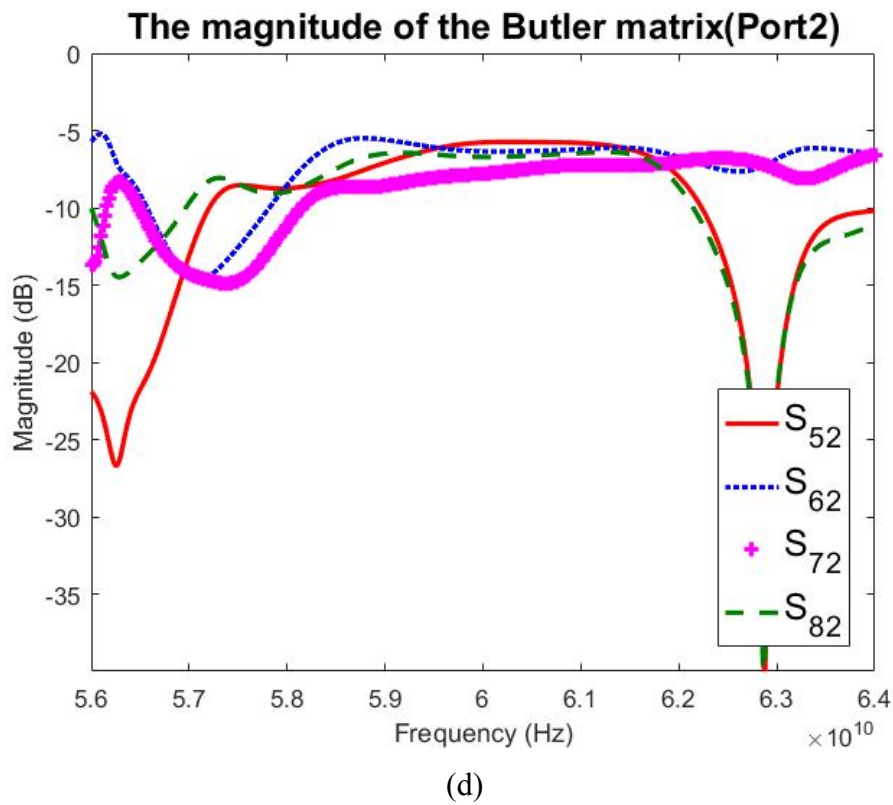


Fig. 5.17 S-parameter of the butler matrix on HFSS while exciting at port 1 and port 2.

(a) S_{11} , S_{21} , S_{31} , S_{41} , (b) S_{51} , S_{61} , S_{71} , S_{81} , (c) S_{12} , S_{22} , S_{32} , S_{42} , and (d) S_{52} , S_{62} , S_{72} , S_{82} .

The total power insertion loss is defined as

$$L = -10 \log_{10}(|S_{5q}|^2 + |S_{6q}|^2 + |S_{7q}|^2 + |S_{8q}|^2) \quad (5.11),$$

where $q = 1$ or 2 represents the exciting port. The simulated total power insertion loss while exciting port is port 1 or port 2 are shown in Fig. 5.18. The simulated total power insertion losses are smaller than 2 dB from 58.29 GHz to 62.05 GHz. Compared to [19], the power insertion losses are below 2.5 dB from 58-62 GHz. Thus, the proposed AFSIW Butler matrix can provide extremely low loss.

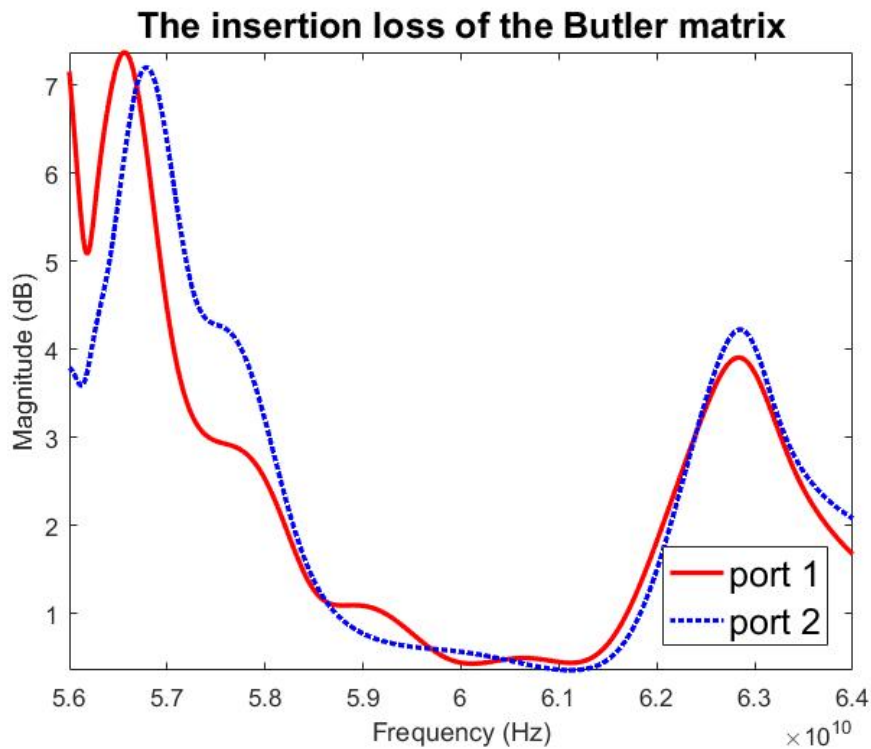


Fig. 5.18 The total power insertion loss of the Butler matrix

The bandwidth of the Butler matrix is defined as the frequency range where the error of the phase difference between the output ports is within $\pm 10^\circ$. The phase difference of the Butler matrix is shown in Fig. 5.19. For ideal case, while the input ports are port 1 and port 2, the phase differences between output ports are -45° and 135° , respectively. For the proposed design here, while the input port is port 1, the simulated bandwidth is between 59.3 GHz to 61.6 GHz. While the input port is port 2, the simulated bandwidth is between 58.9 GHz to 60.7 GHz.

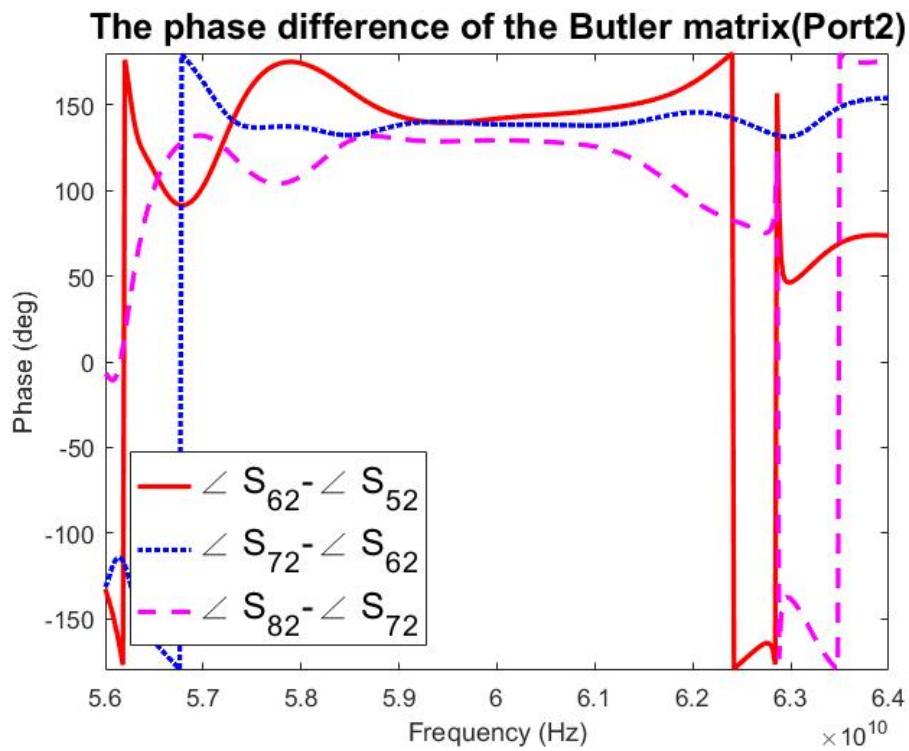
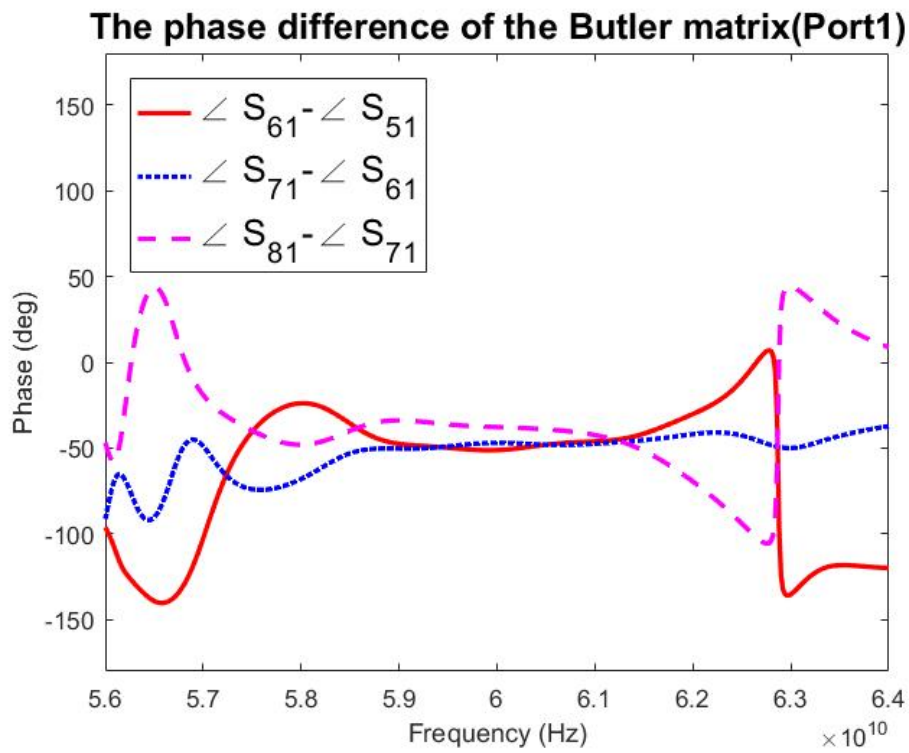


Fig. 5.19 Phase difference of the butler matrix on HFSS. (a) Port 1 (b) Port 2

5.4.2 Proposed Beamforming Antenna Array Using AFSIW

Structure

The proposed beamforming antenna array is composed of the previously designed butler matrix and the slot antenna array. The inter-element distance of the slot antenna array is 0.79λ . The radiation pattern is shown in Fig. 5.20. The four figures are the radiation pattern with different port as exciting port. And the three cases are slot antenna array with and without isolation design and ideal case. The radiation pattern of the single antenna simulated on HFSS is multiplied by array factor to calculate final radiation pattern by MATLAB. The results are shown by “ideal case”. The “with isolation” case represents the HFSS simulation results of Butler matrix antenna array with isolation design. The “without isolation” case represents the HFSS simulation results of Butler matrix antenna array without isolation.

From Fig. 5.20, it's shown that the main beam of the Butler matrix antenna array with isolation almost match the ideal case. The gain of the Butler matrix antenna array is summarized on Table 5.4. It's shown that while exciting port is port 1 and 4, the gain of the “with isolation” case is almost equal to ideal case, respectively. But while exciting port is port 2 and 3, the gain of the “with isolation” case is smaller than ideal case about 2 dB. The direction of the Butler matrix antenna array is summarized on Table 5.5. It's shown that the errors of the direction angle are within $\pm 3^\circ$.

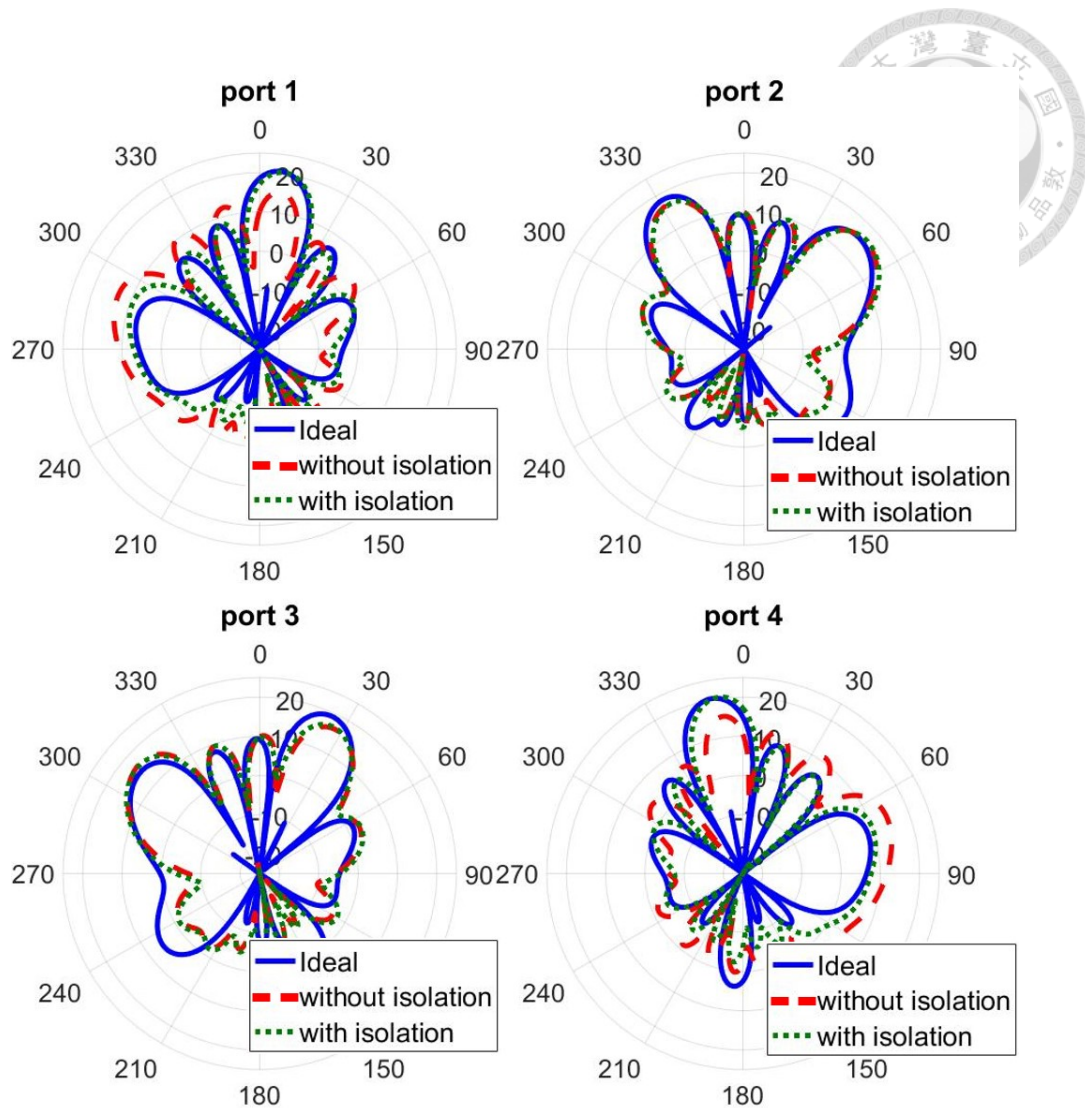


Fig. 5.20 Butler matrix antenna array radiation pattern on HFSS.

<i>Input</i>	Port1	Port2	Port3	Por4
<i>Ideal</i>	20.56 dB	18.72 dB	18.96 dB	20.48 dB
<i>without isolation</i>	15.27 dB	16.51 dB	16.8 dB	15.39 dB
<i>with isolation</i>	20.43 dB	16.67 dB	16.44 dB	20.38 dB

Table 5.4 The gain of the Butler matrix antenna array.



<i>Input</i>	Port1	Port2	Port3	Por4
<i>Ideal</i>	8°	335°	25°	352°
<i>without isolation</i>	8°	334°	28°	353°
<i>with isolation</i>	8°	333°	27°	352°

Table 5.5 The direction angle of the Butler matrix antenna array.

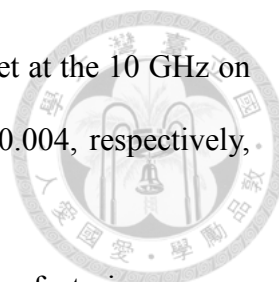
5.5 Measured result and discussion

5.5.1 Coupler and Crossover

Since coupler and crossover are based on the same design method and similar structure, we will only discuss the measured results of the coupler.

From Fig. 5.5 and Fig. 5.8, the measurement results are not match to the simulation results. The reason for the difference will be discussed in the following part.

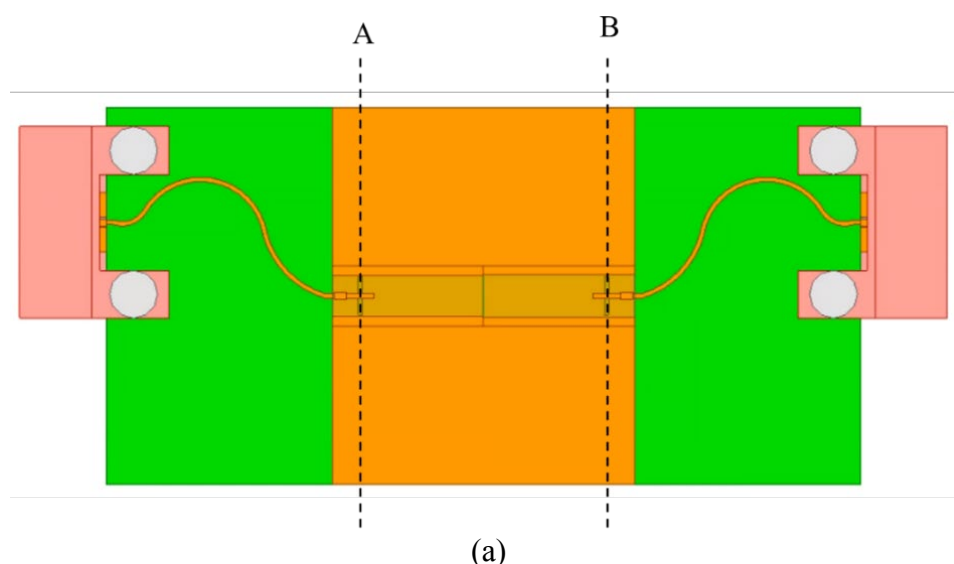
Due to the manufacturing process errors, the calibrating part (Fig. 5.4 AA'-BB' and CC'-DD') of each TRL component and DUT are not the same. The cut-section of Thru and Line are shown in Fig. 5.21. As shown in Fig. 5.21(a), the cut position is at slot for AFSIW. In Fig. 5.21(b) and (c), it's obviously shown that there are large differences between the calibrating parts no matter we compare region A or region B of the Thru and Line.

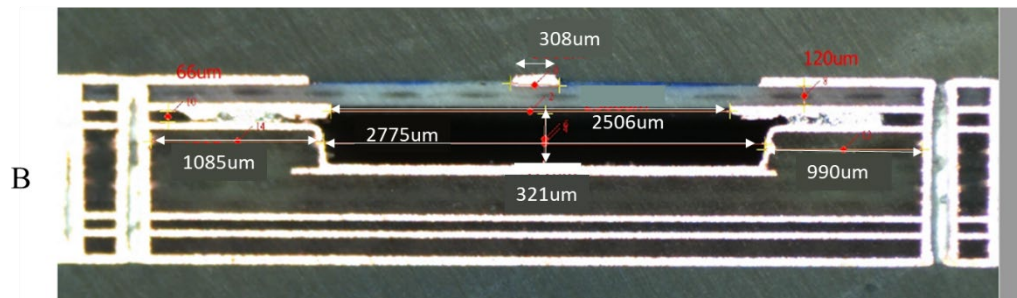
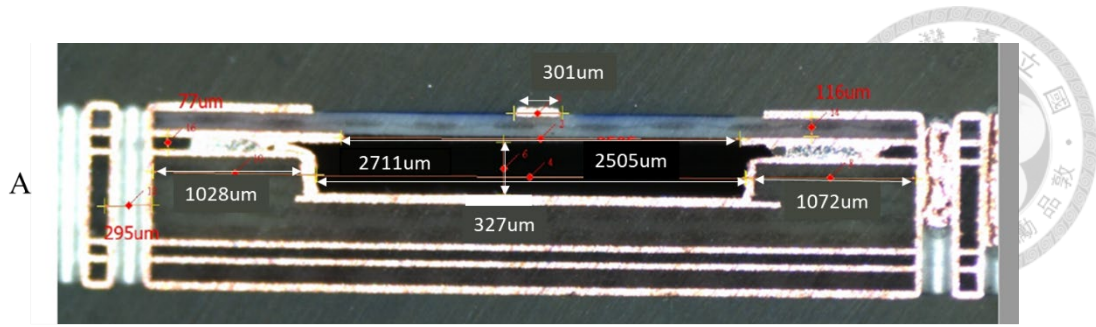


Another reason is that the D_k and D_f of the substrate are set at the 10 GHz on simulation first. The real D_k and D_f at 60 GHz are 3.16 and 0.004, respectively, which are found by measuring the microstrip line at 60 GHz.

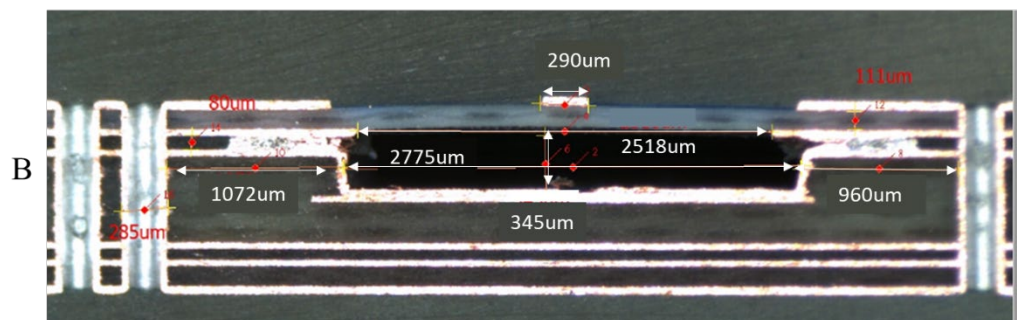
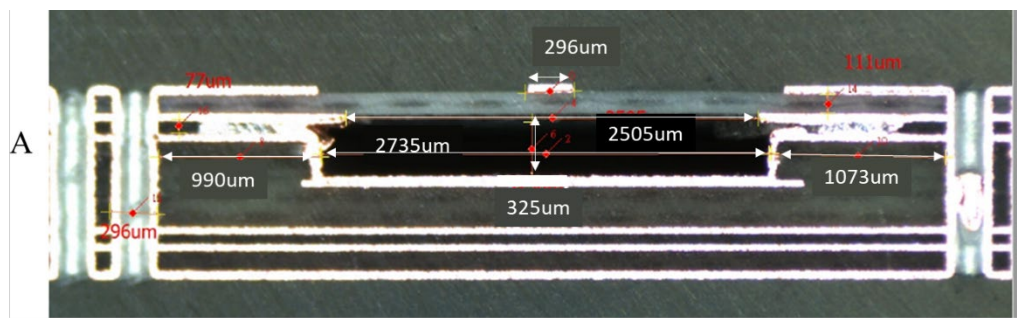
We use post-simulation to observe possible source of the manufacturing process error for calibrating part. The new D_k , D_f and value of the cut-section on feeding slot are used to post-simulate on HFSS.

The post-simulated results and the error box of the TRL are shown in Fig. 5.22. From Fig. 5.22(a), the post-simulated results still didn't match the measured results. So we guess that there are still some structural parameters affecting the performance severely but we can't check the actual value by cut-section, such as the length of the stepped-feeding for AFSIW (as shown Fig. 3.6 (c)). From Fig. 5.22(b), S_{11} of the post-simulated results is more similar to the measured results. But S_{21} still has difference about 4 dB.



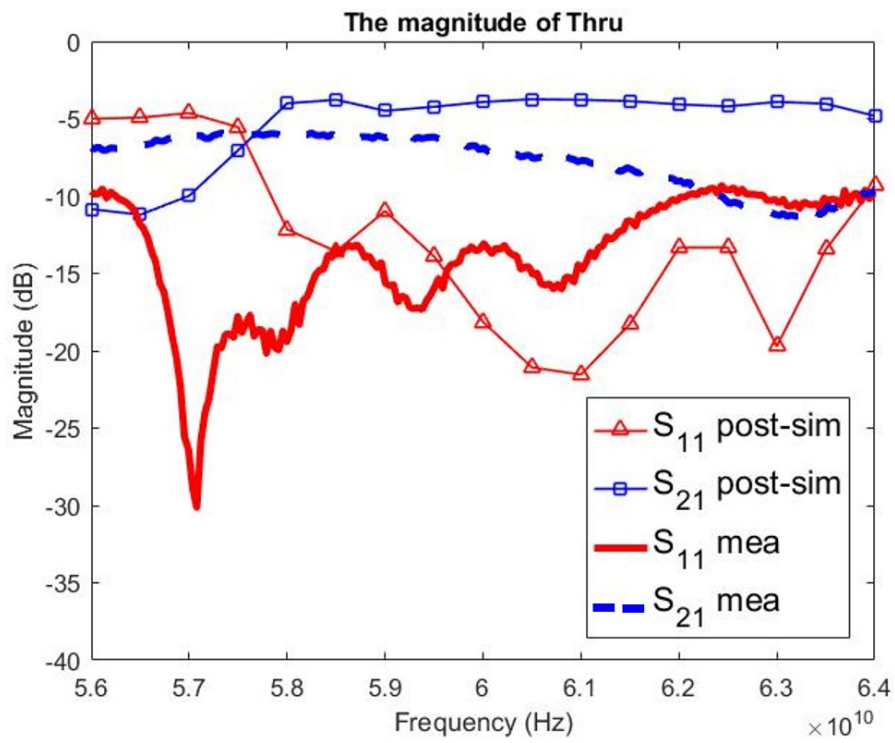


(b)

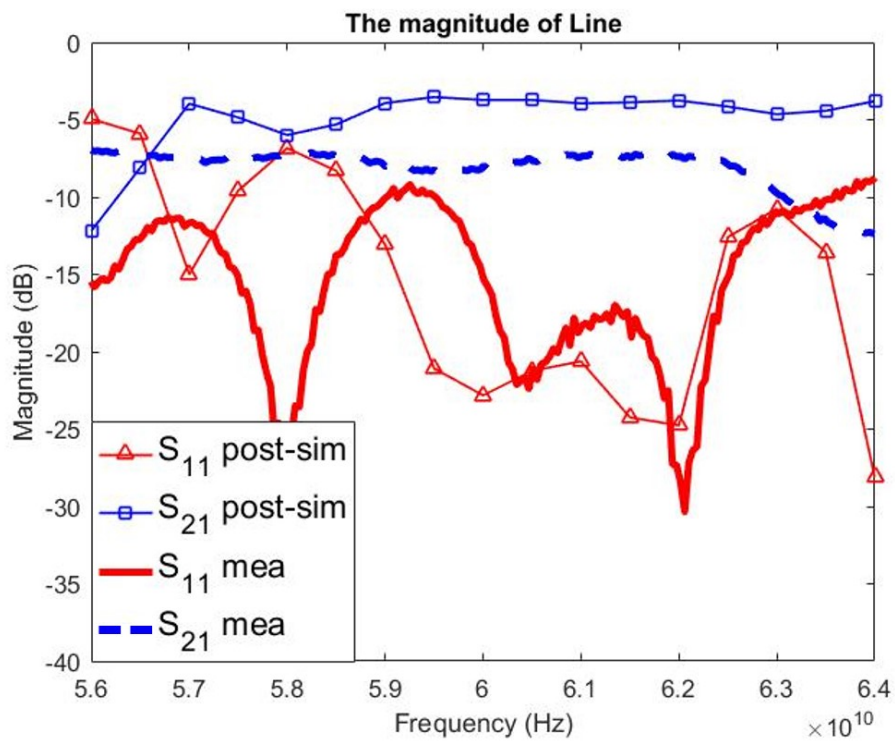


(c)

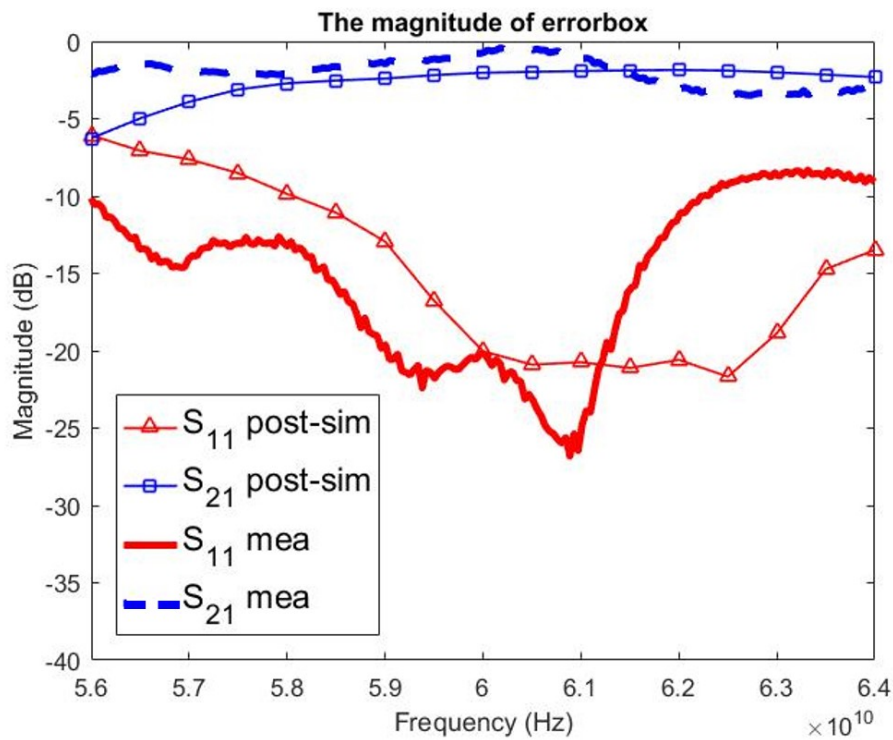
Fig. 5.21 The cut-section of the thru and line. (a) The position of the cut-section. (Top view) (b) Thru (c) Line



(a)



(b)

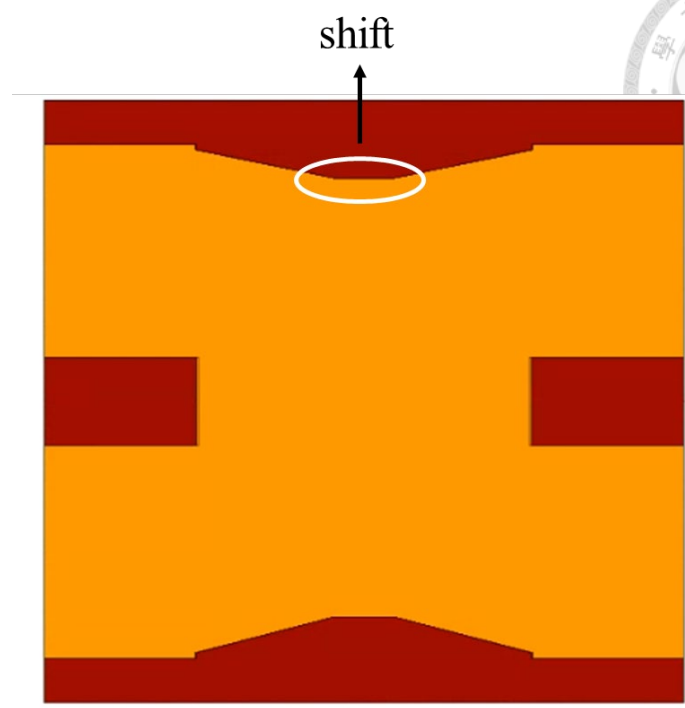


(c)

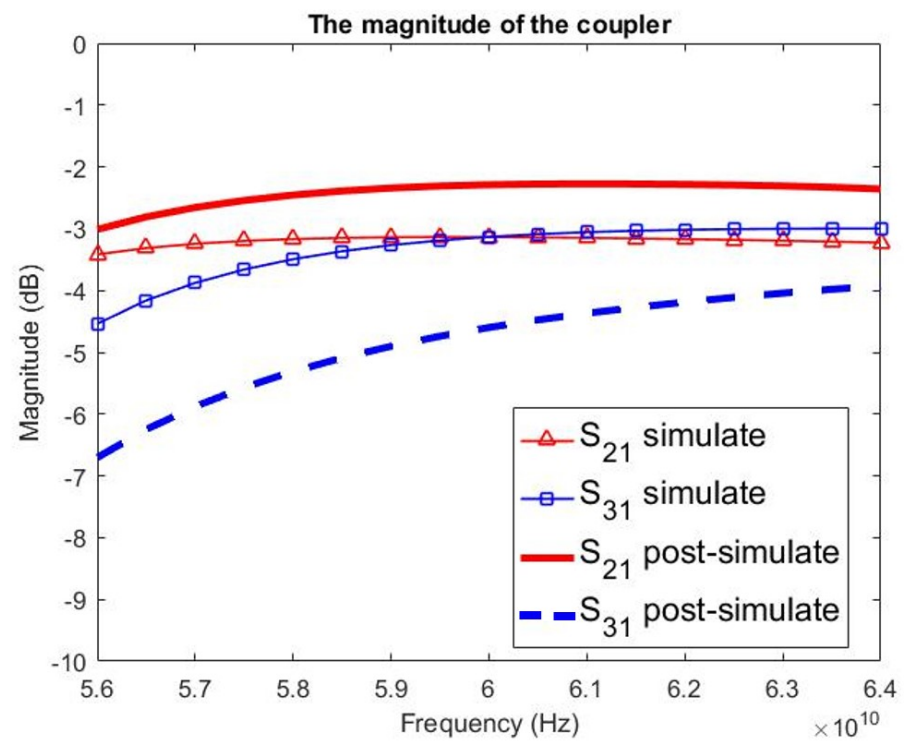
Fig. 5.22 The post-simulated results and the error box of the TRL. (a) Thru (b) Line (c) Error box

Except for the effect from the manufacturing process error in calibrating part, the reason for why S_{21} and S_{31} of coupler has difference on 60.5 GHz to 61.5 GHz is that the coupler is not symmetry. For example, the sidewall of wide air channel at the center is shifted as shown in Fig. 5.23(a). In Fig. 5.23(b), it's shown that asymmetry coupler will increase the difference between S_{21} and S_{31} .

In summary, there are too many factors that might affect the performance, including the error and inconsistency of the manufacturing process on calibration element and DUT, actual performance of end launch and the accuracy of dk and df at our target frequency.



(a)



(b)

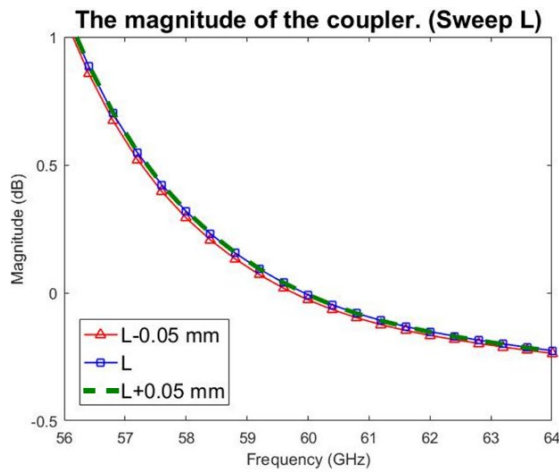
Fig. 5.23 The post-simulated results of asymmetry coupler. (a) Top view of asymmetry coupler (b) S_{21} and S_{31} of post-simulated results



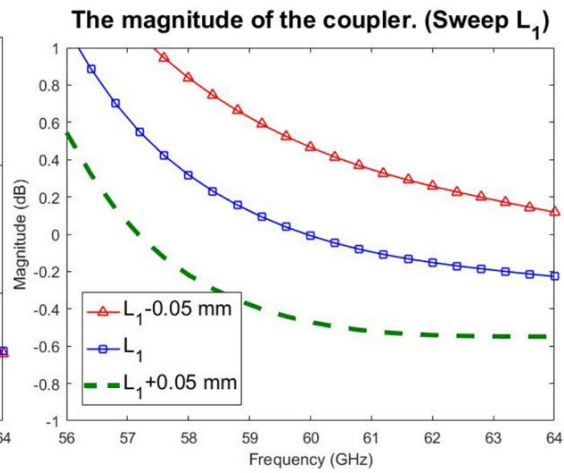
■ Sensitivity About Fabrication

Because the dimension error from fabrication will worsen performance of coupler and crossover, we will discuss each parameter about coupler and crossover in this section. As shown in Fig. 5.3, there are 6 parameters (w , w_1 , w_2 , L , L_1 , L_2). We took the value of Fig. 5.3 and swept $\pm 0.5\text{mm}$ on simulation as the fabrication error.

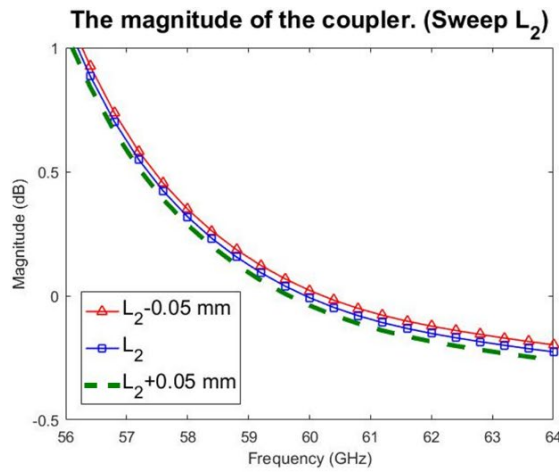
There are not much differences of the magnitudes of S_{11} and S_{41} when parameters of coupler are changed. However, the magnitude of S_{21} and S_{31} in coupler should be as similar as possible to avoid the output power of two output ports inconsistent. Thus, we just focus on the magnitude difference of coupler between S_{21} and S_{31} at 60 GHz. As shown in Fig. 5.24, when $L \pm 0.05\text{mm}$, the magnitude differences ($S_{21} - S_{31}$) of coupler will differ in ± 0.02 dB. And the other parameters with $\pm 0.05\text{mm}$ error, including L_1 , L_2 , w , w_1 , and w_2 , will lead to ± 0.5 dB, ± 0.02 dB, ± 0.1 dB, ± 0.01 dB, and ± 0.03 dB difference for magnitude differences ($S_{21} - S_{31}$). From the above all, we can find that the magnitude difference is very sensitive to L_1 .



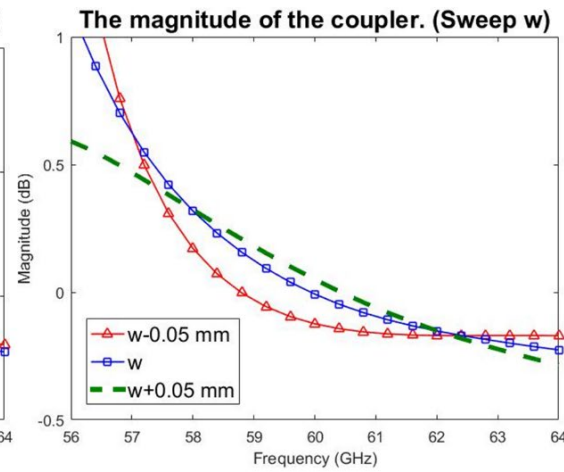
(a)



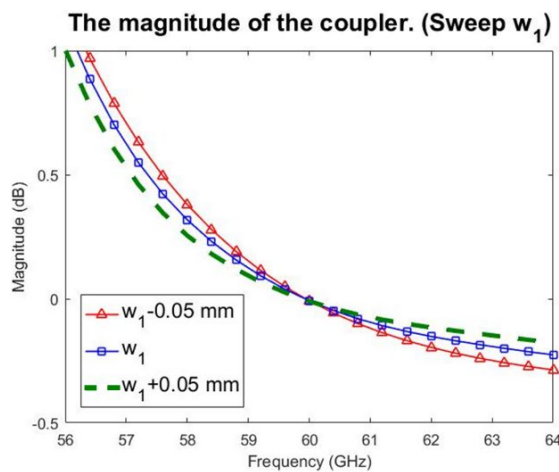
(b)



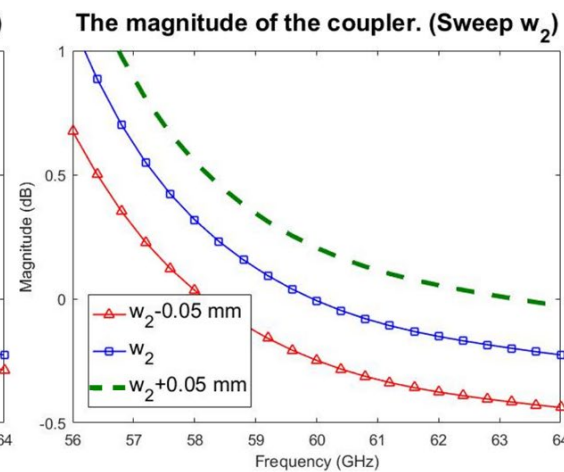
(c)



(d)



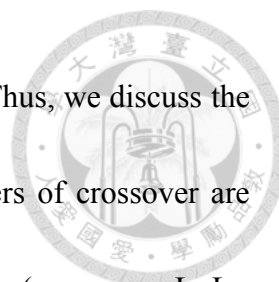
(e)



(f)

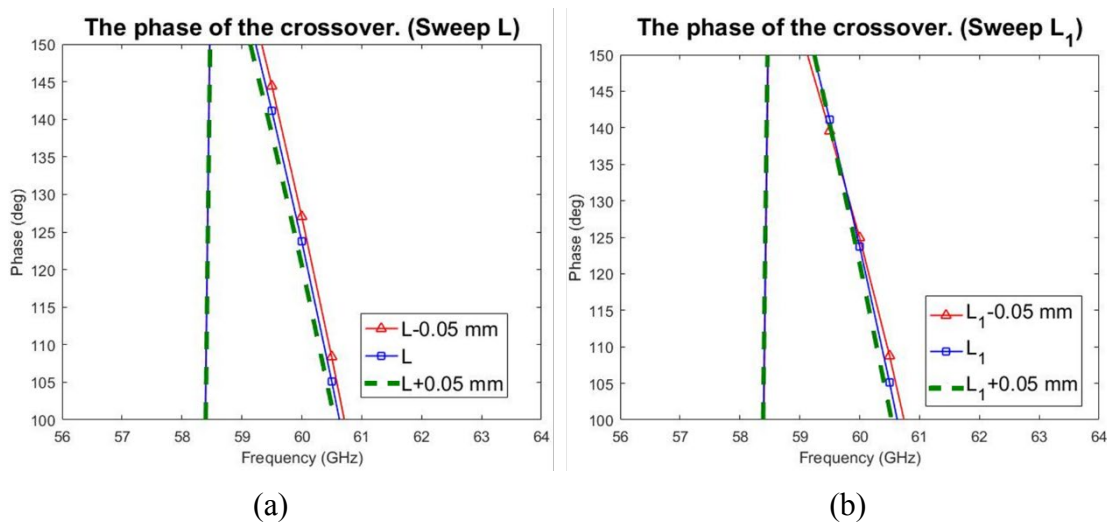
Fig. 5.24 Sweep the parameters $\pm 0.05\text{mm}$ in coupler.

(a)L (b)L₁ (c)L₂ (d)w (e)w₁ (f)w₂



The phase of the crossover in Butler matrix is important. Thus, we discuss the variation of phase in crossover at 60 GHz when the parameters of crossover are changed as follow. As shown in Fig. 5.6, there are 6 parameters (w , w_1 , w_2 , L , L_1 , L_2). We took the value of Fig. 5.6 and swept $\pm 0.5\text{mm}$ on simulation as the fabrication error.

As shown in Fig. 5.25, when $L \pm 0.05\text{mm}$, the phase ($\angle S_{31}$) of coupler will $\pm 3^\circ$. And the other parameters with $\pm 0.05\text{mm}$ error, including L_1 , L_2 , w , w_1 , and w_2 , will lead to $\pm 2^\circ$, $\pm 2^\circ$, $\pm 20^\circ$, $\pm 1^\circ$, and $\pm 5^\circ$ difference for phase ($\angle S_{31}$). From the above all, we can find that the magnitude difference is very sensitive to w .



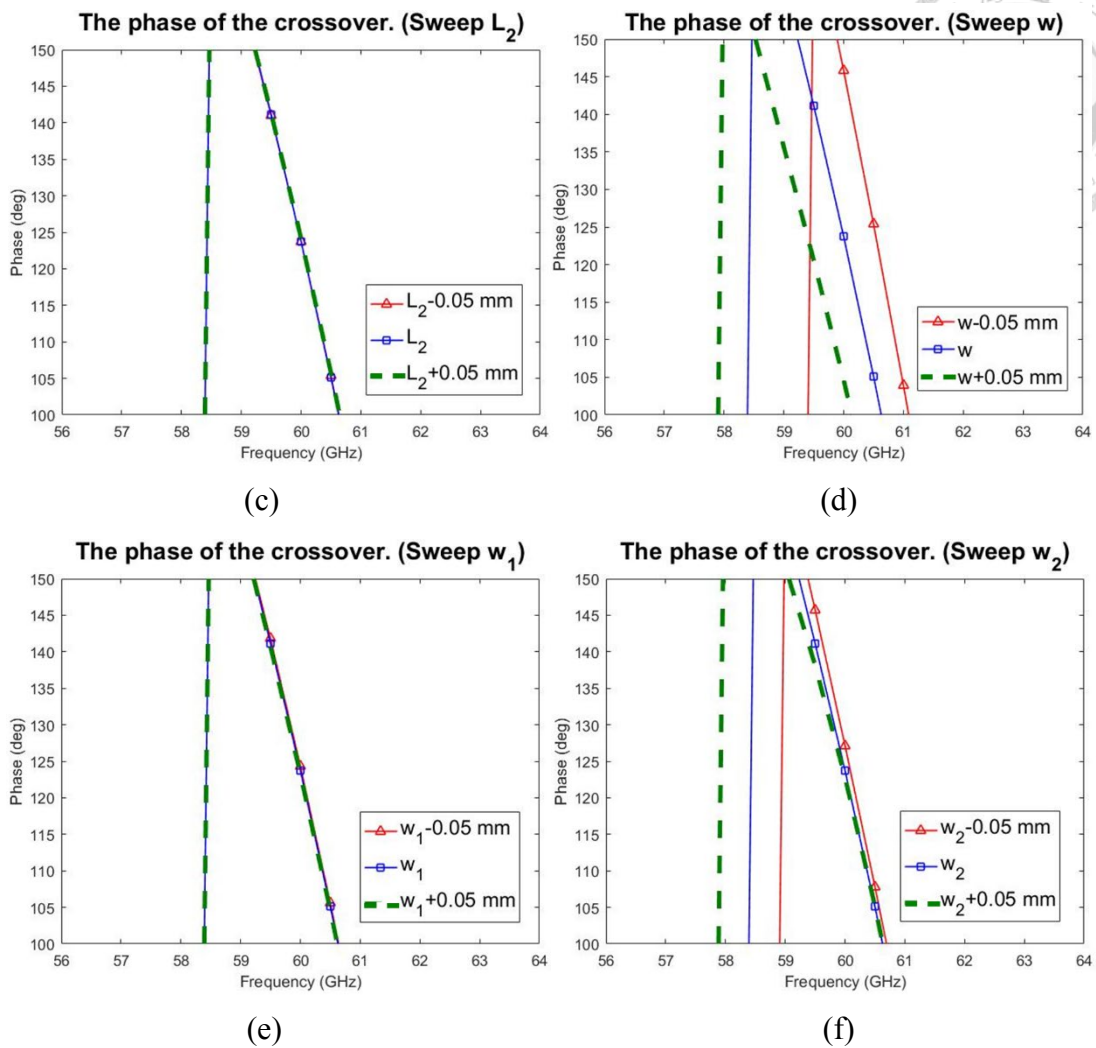
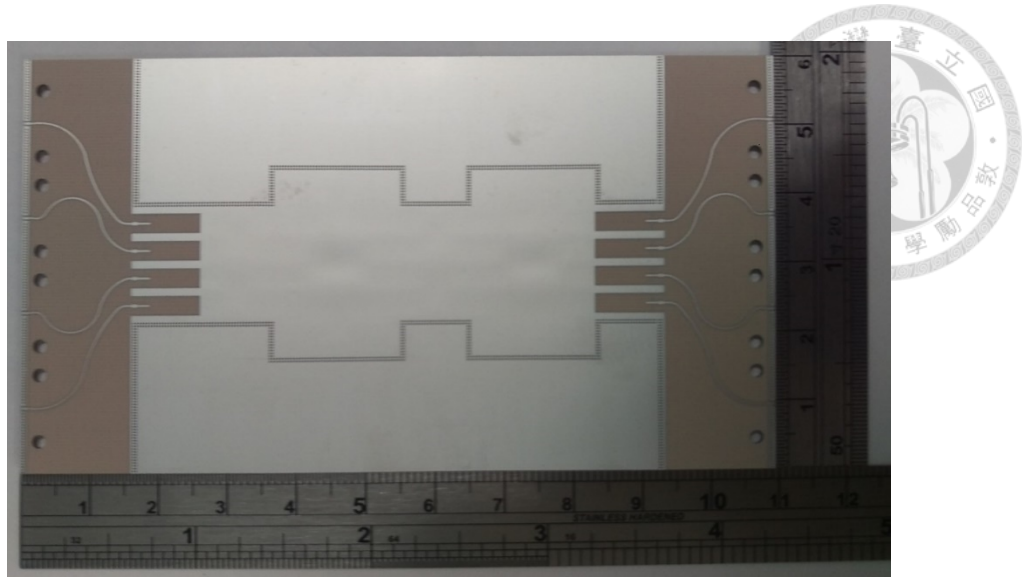


Fig. 5.25 Sweep the parameters ± 0.05 mm in crossover.

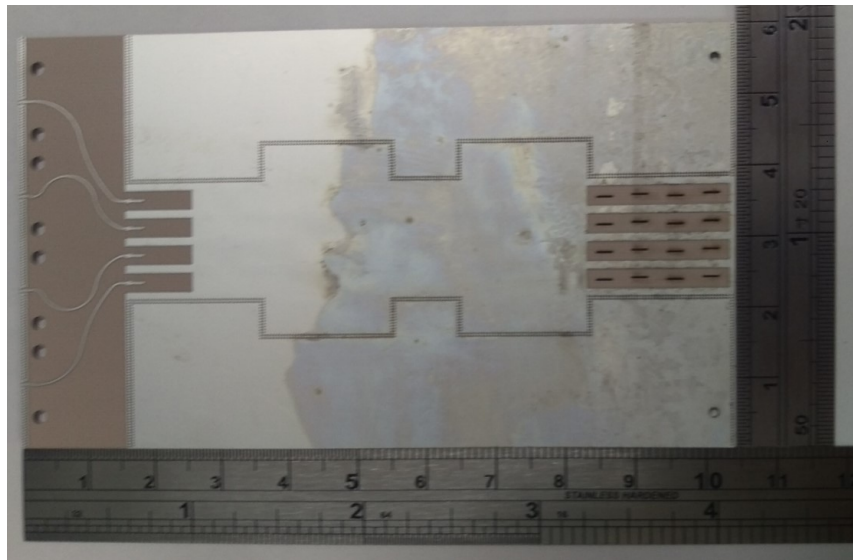
(a)L (b) L_1 (c) L_2 (d) w (e) w_1 (f) w_2

5.5.2 Butler Matrix and Butler Matrix Antenna Array

The photograph of the Butler matrix and Butler matrix antenna array are shown in Fig. 5.26.



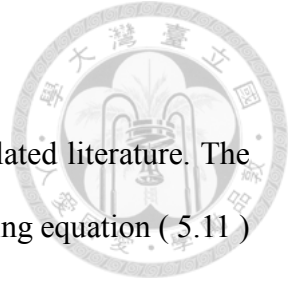
(a)



(b)

Fig. 5.26 The photograph of (a) Butler matrix (b) Butler matrix antenna array.

The measured results of the Butler matrix and Butler matrix antenna array are also failed. The reason might be the same as the phase shifter manufacturing mentioned in Section 4.4. Also, the manufacturing errors for crossover and coupler discussed above might occur in the Butler matrix and Butler matrix antenna array. Further cut-section is needed to check the detailed root cause for this failure.



5.5.3 Comparison and Discussion

Table 5.6 compares several previous Butler matrices in related literature. The structure (SIW/AFSIW) and the total power insertion losses (using equation (5.11) to calculate) are included in the table. Since phase difference of each output port is related to the directions of main beam, the phase errors are included in the table, too. The phase errors are defined as the error of the ideal phase difference at center frequency. Since the measurement has not been successful, the simulation results are compared.

As shown in Table 5.6, the total power insertion losses of previous works are larger than this work because these works are designed based on SIW. In [8],[12],[13],[22], the total power insertion losses are lower than 1 dB since the substrates inside the SIW are low-loss material.

In [6],[9],[20], phase error of them are below 10° . Since the coupler in [6] is modified with hollow rectangular holes in a dielectric substrate and [9],[20] are designed without the crossover, these methods can achieve smaller phase error. But the total power losses of them are larger than 1 dB.

Only in [12], both total power insertion losses are below 1 dB and the phase error is below 10° . Since the coupler in [12] is double-layer structure, it can reduce the size and remove the crossover to reduce total power insertion loss and phase error. But the total power insertion losses per lambda (total power insertion losses \div length of the Butler matrix) in [12] are still higher than this work.

The size is defined as the width and length of Butler matrix. The size of this work is $4.44\lambda \times 11.4\lambda$. Although the size of this work is the largest among all works listed in Table 5.6, the total power insertion loss of this work is the smallest. The

total power insertion loss of this work is 0.6 dB. Compared with the works with center frequency of 60 GHz, the phase error of this work is the smallest one.

Ref.	Center frequency	Structure	Size ($w \times l$)	total power insertion loss	Phase error (@ center frequency)
[3]	26 GHz	SIW	$3.03\lambda \times 9.53\lambda$	N/A	$< 10^\circ$
[6]	26 GHz	SIW	$3.47\lambda \times 5.11\lambda$	< 2 dB	7°
[7]	60 GHz	SIW	N/A	1.4 dB* (@59.5 GHz)	$< 20^{\circ*}$
[8]	16 GHz	SIW	$5.87\lambda \times 9.33\lambda$	< 1 dB*	N/A
[9]	38 GHz	SIW (2 layer)	$7.6\lambda \times 8.16\lambda$	1.8 dB*	$5^{\circ*}$
[12]	12.5 GHz	SIW (2 layer)	$1.51\lambda \times 3.47\lambda$	< 1 dB	10°
[13]	60 GHz	SIW (3 layer)	$2.6\lambda \times 6.4\lambda$	< 1 dB*	$< 15^{\circ*}$
[16]	9.5 GHz	SIW (2 layer)	$1.08\lambda \times 1.74\lambda$	N/A	$< 10^\circ$
[17]	30 GHz	SIW	N/A	N/A	$13^{\circ*}$
[19]	60 GHz	SIW	$3.56\lambda \times 5.42\lambda$	< 2.5 dB	17°
[20]	77 GHz	SIW	$7.32\lambda \times 8.09\lambda$	1.6 dB**	$4^{\circ*}$
[22]	60 GHz	SIW	$3\lambda \times 3.8\lambda$	< 1 dB*	$< 32^{\circ*}$
[23]	60 GHz	SIW	$1.76\lambda \times 4.74\lambda$	< 2.7 dB*	$< 15^{\circ*}$
This work	60 GHz	AFSIW	$4.44\lambda \times 11.4\lambda$	0.6 dB*	$14^{\circ*}$

N/A: Did not mention in the paper.

** : Estimated measurement result

* : Simulated result

Table 5.6 Performance summary and comparison of Butler matrix to related literature.





Chapter 6

Conclusions

In this thesis, the low loss beamforming antenna array using AFSIW applying at mm-Wave is proposed. The motivation is to reduce the path-loss of the beamforming antenna array. The proposed method is to develop the novel structure AFSIW, which changes the lossy dielectric substrate of the conventional SIW into the air. Therefore, the AFSIW structure can avoid the loss from the substrate. The Butler matrix on AFSIW structure provides extremely low path-loss compared to the Butler matrix on SIW structure. In addition, since AFSIW is modified from the SIW, AFSIW has the same planar characteristic of the SIW and is easy for system packaging.

In Chapter 3, the novel structure is developed. It deals with the problem of the path-loss. In Chapter 4, the shorted-end stub phase shifter is designed on AFSIW structure. The stub phase shifter formulas are derived and design flow for AFSIW phase shifter are introduced. In Chapter 5, the other components of the Butler matrix are designed on the AFSIW to form a low loss beamforming antenna array.

The phase shifter is designed to produce a desired phase difference compared to crossover for Butler matrix. And the bandwidth is the frequency range where the phase difference error is in $\pm 5^\circ$ in contrast to desired phase difference. The bandwidth of 0-

degree phase shifter is 4GHz on simulation. The bandwidth of 45-degree phase shifter is 3.6 GHz on simulation.

The coupler and crossover are designed based on the short-slot method. The S_{21} and S_{31} of the simulated coupler respectively are -3.13 dB and -3.14 dB at 60 GHz. The phase difference between the S_{21} and S_{31} is $90^\circ \pm 5^\circ$ between 56.2 to 65.6 GHz on simulation. The S_{31} of the simulated crossover is -0.15 dB at 60 GHz. The bandwidth (defined by S_{11} lower than -15 dB) of the crossover is between 58.7 to 61.6 GHz on simulation.

The proposed Butler matrix is composed of the above components. The simulated total power insertion losses are 0.6 dB at 60 GHz. Compared with the other works in related literature, the proposed Butler matrix has the lowest total power insertion losses. While the input port is port 1, the simulated bandwidth (defined by the desired phase difference $\pm 10^\circ$) is 2.3 GHz. While the input port is port 2, the simulated bandwidth is 1.8 GHz. Then, the gain of proposed Butler matrix antenna array without isolation is between 15 to 17 dB on simulation. The gain of proposed Butler matrix antenna array with isolation is between 16 to 21 dB on simulation. The isolation of the antenna array is improved obviously.

So far, the isolations of proposed beamforming antenna array are improved on simulation. But the measurements of the proposed beamforming antenna array are failed. In the future, more cut-sections are needed to check the main root cause of measurement failure. We can try to design the proposed beamforming antenna array in the stable manufacturing process to prevent failure. The bandwidth (defined by the desired phase difference $\pm 10^\circ$) of the Butler matrix can be wider by optimizing crossover or phase shifter to improve the error of phase difference. The end launch can be changed to probe to avoid the bad performance caused by human influence. In the future based on stable


manufacturing process, we can provide an extremely low path-loss beamforming array for 5G communication.

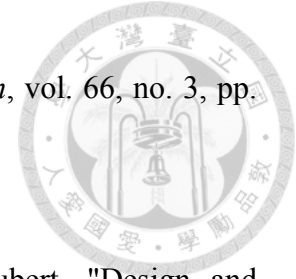


REFERENCE

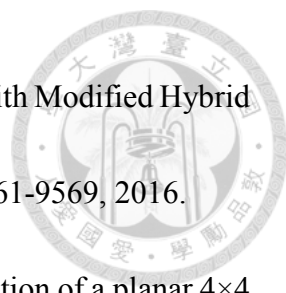


- [1] Y. Niu, Y. Li, D. Jin, L. Su, A. Vasilakos, "A survey of millimeter wave communications (mmWave) for 5G: Opportunities and challenges", *Wireless Netw.*, pp. 1-20, Apr. 2015.
- [2] B. Yang, Z. Yu, Y. Dong, J. Zhou and W. Hong, "Compact Tapered Slot Antenna Array for 5G Millimeter-Wave Massive MIMO Systems," in *IEEE Transactions on Antennas and Propagation*, vol. 65, no. 12, pp. 6721-6727, Dec. 2017.
- [3] S. Yamamoto, J. Hirokawa and M. Ando, "A beam switching slot array with a 4-way Butler matrix installed in a single layer post-wall waveguide," *IEEE Antennas and Propagation Society International Symposium (IEEE Cat. No.02CH37313)*, San Antonio, TX, USA, 2002, pp. 138-141 vol.1.
- [4] P. Chen, W. Hong, Z. Kuai and J. Xu, "A Double Layer Substrate Integrated Waveguide Blass Matrix for Beamforming Applications," in *IEEE Microwave and Wireless Components Letters*, vol. 19, no. 6, pp. 374-376, June 2009.
- [5] T. Djerafi, N. J. G. Fonseca and K. Wu, "Planar Ku-Band 4×4 Nolen Matrix in SIW Technology," in *IEEE Transactions on Microwave Theory and Techniques*, vol. 58, no. 2, pp. 259-266, Feb. 2010.

- 
- [6] S. Yamamoto, J. Hirokawa, M. Ando, "A half-sized post-wall short-slot directional coupler with hollow rectangular holes in a dielectric substrate", *IEICE Trans. Electron.*, vol. 88, no. 7, pp. 1387-1394, Jul. 2005.
- [7] F. F. He, K. Wu, W. Hong, L. Han and X. Chen, "Low-Cost 60-GHz Smart Antenna Receiver Subsystem Based on Substrate Integrated Waveguide Technology," in *IEEE Transactions on Microwave Theory and Techniques*, vol. 60, no. 4, pp. 1156-1165, April 2012.
- [8] P. Chen *et al.*, "A Multibeam Antenna Based on Substrate Integrated Waveguide Technology for MIMO Wireless Communications," in *IEEE Transactions on Antennas and Propagation*, vol. 57, no. 6, pp. 1813-1821, June 2009.
- [9] Y. Cao, K. Chin, W. Che, W. Yang and E. S. Li, "A Compact 38 GHz Multibeam Antenna Array With Multifolded Butler Matrix for 5G Applications," in *IEEE Antennas and Wireless Propagation Letters*, vol. 16, pp. 2996-2999, 2017.
- [10] J. Lian, Y. Ban, J. Zhu, K. Kang and Z. Nie, "Compact 2-D Scanning Multibeam Array Utilizing the SIW Three-Way Couplers at 28 GHz," in *IEEE Antennas and Wireless Propagation Letters*, vol. 17, no. 10, pp. 1915-1919, Oct. 2018.
- [11] J. Lian, Y. Ban, Q. Yang, B. Fu, Z. Yu and L. Sun, "Planar Millimeter-Wave 2-D Beam-Scanning Multibeam Array Antenna Fed by Compact SIW Beam-Forming

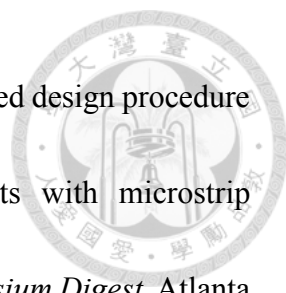


- Network," in *IEEE Transactions on Antennas and Propagation*, vol. 66, no. 3, pp. 1299-1310, March 2018.
- [12] A. A. M. Ali, N. J. G. Fonseca, F. Coccetti and H. Aubert, "Design and Implementation of Two-Layer Compact Wideband Butler Matrices in SIW Technology for Ku-Band Applications," in *IEEE Transactions on Antennas and Propagation*, vol. 59, no. 2, pp. 503-512, Feb. 2011.
- [13] X. Cheng *et al.*, "A Compact Multi-Beam End-Fire Circularly Polarized Septum Antenna Array for Millimeter-Wave Applications," in *IEEE Access*, vol. 6, pp. 62784-62792, 2018.
- [14] H. J. Riblet, "The Short-Slot Hybrid Junction," in *Proceedings of the IRE*, vol. 40, no. 2, pp. 180-184, Feb. 1952.
- [15] F. Carrera, D. Navarro, M. Baquero-Escudero and V. M. Rodrigo-Peñarrocha, "Compact substrate integrated waveguide directional couplers in Ku and K bands," *The 40th European Microwave Conference*, Paris, 2010, pp. 1178-1181.
- [16] S. Karamzadeh, V. Rafii, M. Kartal and B. S. Virdee, "Compact and Broadband 4×4 SIW Butler Matrix With Phase and Magnitude Error Reduction," in *IEEE Microwave and Wireless Components Letters*, vol. 25, no. 12, pp. 772-774, Dec. 2015.

- 
- [17] Q. Yang, Y. Ban, J. Lian, Z. Yu and B. Wu, "SIW Butler Matrix with Modified Hybrid Coupler for Slot Antenna Array," in *IEEE Access*, vol. 4, pp. 9561-9569, 2016.
- [18] T. Djerafi, N. J. G. Fonseca and K. Wu, "Design and implementation of a planar 4×4 butler matrix in SIW technology for wideband applications," *The 40th European Microwave Conference*, Paris, 2010, pp. 910-913.
- [19] C. Chen and T. Chu, "Design of a 60-GHz Substrate Integrated Waveguide Butler Matrix—A Systematic Approach," in *IEEE Transactions on Microwave Theory and Techniques*, vol. 58, no. 7, pp. 1724-1733, July 2010.
- [20] T. Djerafi and K. Wu, "A Low-Cost Wideband 77-GHz Planar Butler Matrix in SIW Technology," in *IEEE Transactions on Antennas and Propagation*, vol. 60, no. 10, pp. 4949-4954, Oct. 2012.
- [21] M. K. Khattak, S. Kahng, M. S. Khattak, A. Rehman, C. Lee and D. Han, "A low profile, wideband and high gain beam-steering antenna for 5G mobile communication," *2017 IEEE International Symposium on Antennas and Propagation & USNC/URSI National Radio Science Meeting*, San Diego, CA, 2017, pp. 2575-2576.
- [22] N. Tiwari and T. R. Rao, "A switched beam antenna array with butler matrix network using substrate integrated waveguide technology for 60 GHz



- communications," *2015 International Conference on Advances in Computing, Communications and Informatics (ICACCI)*, Kochi, 2015, pp. 2152-2157.
- [23] Z. Chen, X. Wu and F. Yang, "A compact SIW butler matrix with straight delay lines at 60 GHz," *2017 IEEE International Symposium on Antennas and Propagation & USNC/URSI National Radio Science Meeting*, San Diego, CA, 2017, pp. 2141-2142.
- [24] O. Kramer, T. Djerafi and K. Wu, "Dual-layered substrate-integrated waveguide six-port with wideband double-stub phase shifter," in *IET Microwaves, Antennas & Propagation*, vol. 6, no. 15, pp. 1704-1709, 11 December 2012.
- [25] J. Dittloff, F. Arndt and D. Grauerholz, "Optimum design of waveguide E-plane stub-loaded phase shifters," in *IEEE Transactions on Microwave Theory and Techniques*, vol. 36, no. 3, pp. 582-587, March 1988.
- [26] D. M. Pozar, *Microwave Engineering*, 4th Edition New York: Wiley, 2011.
- [27] Z. C. Hao, W. Hong, J. X. Chen, H. X. Zhou and K. Wu, "Single-layer substrate integrated waveguide directional couplers," in *IEE Proceedings - Microwaves, Antennas and Propagation*, vol. 153, no. 5, pp. 426-431, Oct. 2006.
- [28] Feng Xu and Ke Wu, "Guided-wave and leakage characteristics of substrate integrated waveguide," in *IEEE Transactions on Microwave Theory and Techniques*, vol. 53, no. 1, pp. 66-73, Jan. 2005.

- 
- [29] J. E. Rayas-Sanchez and V. Gutierrez-Ayala, "A general EM-based design procedure for single-layer substrate integrated waveguide interconnects with microstrip transitions," *2008 IEEE MTT-S International Microwave Symposium Digest*, Atlanta, GA, USA, 2008, pp. 983-986.
- [30] J. D. Kraus and R. J. Marhefka, *Antennas for All Applications*, 3rd Edition, McGraw Hill, New York, 2003.
- [31] Zhubenko, V., "Passive microwave components and antennas," In-Tech, India, 2010.
- [32] X. Huang and K. Wu, "A Broadband U-Slot Coupled Microstrip-to-Waveguide Transition," in *IEEE Transactions on Microwave Theory and Techniques*, vol. 60, no. 5, pp. 1210-1217, May 2012.
- [33] N. Marcuvitz, *Waveguide Handbook*, New York:McGraw-Hill, 1951.
- [34] P. Rizzi, *Microwave Engineering Passive Circuits*, NJ, Englewood Cliffs:Prentice-Hall, 1988.
- [35] T. A. Milligan, *Modern Antenna Design*, New York:McGraw-Hill, 1985.
- [36] X. Chen, S. Zhang and Q. Li, "A Review of Mutual Coupling in MIMO Systems," in *IEEE Access*, vol. 6, pp. 24706-24719, 2018.